Crystallization of Lennard-Jones nanodroplets: from near melting to deeply supercooled

by

©Shahrazad Malek

A thesis submitted to the School of Graduate Studies in partial fulfillment of the requirements for the degree of

M.Sc.

Department of Physics and Physical Oceanography
Memorial University of Newfoundland

Memorial University of Newfoundland

October 2014

ST. JOHN'S NEWFOUNDLAND

Abstract

We carry out molecular dynamics and Monte Carlo simulations to characterize nucleation in liquid clusters of 600 Lennard-Jones particles over a broad range of temperatures. We find that Classical Nucleation Theory (CNT) predicts the rate quite well, even when employing simple modelling of crystallite shape, chemical potential, surface tension and particle attachment rate, down to the temperature where the droplet loses metastability and crystallization proceeds through growth-limited nucleation. Below this crossover temperature, the nucleation rate is controlled by particle attachment rates and is still described by CNT, but with thermodynamic quantities that appear to be "frozen in" to values at the crossover temperature. We use the formalism of mean first-passage times to determine the rate and to reconstruct free energy profiles, which agree at higher temperatures with those obtained through umbrella sampling Monte Carlo. Discrepancy arises when twinned structures with five-fold symmetry provide a competing free energy pathway out of the region of critically-sized embryos. We find that crystallization begins with hcp-fcc stacked precritical nuclei and differentiation to various end structures occurs when these embryos are critical or post-critical in size. We comment on using the largest embryo in the system as a reaction coordinate, confirm that it is useful in determining the onset of growth-limited nucleation and show that it gives the same free energy barriers as the full cluster size distribution once the proper reference state is identified. We find that the bulk melting tempera-

ture controls the rate, even thought the solid-liquid coexistence temperature for the droplet is significantly lower. Additionally, we find that the anisotropy of critical embryos grows at low temperature, but largely follows the same size dependence of anisotropy for embryos taken from a single temperature near coexistence.

Acknowledgements

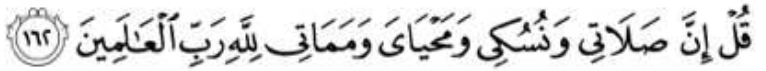

"Indeed, my prayer, my rites of sacrifice, my living and my dying are for Allah , Lord of the worlds."

All my appreciation to my Lord GOD, for his beautiful designing of my life.

In the first place, I would like to thank my supervisor Dr. Ivan Saika-Voivod for being a nice friend as much as he is a fantastic supervisor, for his trust in his students, for never giving me a feeling that I disappointed him during the learning process, for being patience and a good teacher in many of the life prospectives. I would thank him for all the absolutely amazing conversations I had with him.

I would thank my mother Ibtihaj, my father Mohammad, and my siblings for their wonderful support, especially my beloved sister Camellia.

I would like to thank Carmen Paul and Patsy-marie Campbell for their tremendously uplifting words when everything seems to be closed in my face.

I would thank Dr. Sam Bromley who taught me programming course and has a great benefit on my progress, and for his massive believing in his students. And I would like to thank also Dr. Anand Yethiraj who taught me *Soft Matter*. Finally, I would like to acknowledge ACEnet for carrying up our computational work.

Table of Contents

Abstract **ii**

Acknowledgments **iv**

Table of Contents **vii**

List of Tables **viii**

List of Figures **x**

1 Intoduction **1**

2 Theoretical Background **4**

2.1 Classical Nucleation Theory 4

2.1.1 Cluster Distribution 5

2.1.2 Modelling the Free Energy Barrier 7

2.1.3 The Nucleation Rate 10

2.2 $n_{\max}$ as the Order Parameter 14

2.3 The Mean First-Passage Time Formalism 17

2.4 Reconstructing the Free Energy Landscape from the Steady-State . . 20

3 Methodology **25**

3.1 Molecular Dynamics Simulations . . . 25
3.2 Monte Carlo . . . 28
3.3 Umbrella Sampling . . . 30
3.4 Reduced Units . . . 31
3.5 The Simulated System . . . 32
3.6 Determining Crystal Structure . . . 34

4 Results **36**
4.1 Nucleation rates from MFPT . . . 36
4.2 T dependence of the rate and CNT . . . 40
4.2.1 The melting temperature . . . 43
4.2.2 The enthalpy difference . . . 45
4.2.3 Embryo shape . . . 46
4.2.4 Attachment rate . . . 50
4.2.5 Surface tension . . . 57
4.3 Free energy barriers . . . 58
4.3.1 MFPT barrier reconstruction and MC calculations . . . 58
4.3.2 T-dependence of barrier heights and critical embryo sizes . . . 60
4.3.3 Escape from the critical state . . . 68

5 Discussion **73**

6 Conclusions **77**
Bibliography . . . 80

A The Fokker-Planck Equation **88**
A.1 Stochastic process . . . 88
A.2 Derive Fokker-Planck equation from thermodynamics . . . 89

A.3 Derive Fokker-Planck equation from Mathmatics 93

B The Simulation Results **96**

List of Tables

3.1 Natural LJ units.. 32

4.1 The fitting parameters obtained for J_{250}, and J_{MFPT} with Eq. 2.23. . 42

B.1 Simulation results data. 97

List of Figures

2.1 The bulk and surface contributions to the free energy. 9

2.2 Double-well potential. 18

3.1 The Lennard-Jones pair potential. 26

4.1 The series of potential energy U and largest embryo size $n_{\max}$ at T =0.485, 0.455, 0.430, 0.485, and 0.200. 37

4.2 Mean first-passage time $\tau(n)$ for the appearance of an embryo of size n for a range of T 39

4.3 Nucleation rate as a function of T. 41

4.4 Potential energy times series for the droplet at $T = 0.490$. 44

4.5 Determination of C_V from reweighting histograms obtained from the probability distribution for the potential energy at $T = 0.490$. 47

4.6 Determining the enthalpy $\Delta H/N_p$. 48

4.7 Estimating the shape factor $A = Sn^{-2/3}$ as a function of embryo size. 49

4.8 Quantifying embryo anisotropy. 52

4.9 Steady-state distributions $P^{st}_{\max}(n)$ obtained at $T = 0.485$ for different values of b 53

4.10 Determination of the attachment rate to the critical cluster. 55

4.11 Barrier reconstruction from the steady-state probability distribution and $\tau(n)$ at T =0.485, and 0.475 compared to MC results. 59
4.12 Barrier profiles from barrier reconstruction method and MC at T=0.450, and 0.370 61
4.13 Nucleation barrier heights and size of the critical cluster as a function of T 63
4.14 CNT relations $\Delta\mu = 2\Delta G^*/n^*$ and $\gamma = 3\Delta G^*/S^*$ as a function of T. 65
4.15 $\beta\Delta G(n)$ from $T = 0.485$ (circles) with fits to Eq. 2.9. 67
4.16 Probability distribution for Q_6 at $T = 0.475$ for $60 \leq n_{\max} \leq 100$. . . 68
4.17 Joint probability distributions for $n_{\max}$ and Q_6 at $T = 0.475$. 71
4.18 Droplet configurations containing critical embryos for low and high Q_6 at T =0.485, 0.475, 0.465, 0.424, and 0.200. 72

Chapter 1

Intoduction

Nanotechnology has garnered much interest in the last few decades because of the wide range of applications that come out of it. Nanoclusters, small clusters comprising tens to millions of atoms, are used in a variety of settings, such as tuning the optical [1–3] and electronic properties of materials [2,4], biolabeling and imaging [5], catalysis [6,7], and chemical sensing [8]. The various structures to which nanoclusters solidify, as well as their surface properties, bear a strong impact on their function [9].

Much attention has been paid to the size dependence of nanocluster structure. Experimental work on argon clusters showed that for fewer than 50 atoms, poly-icosahedral structure emerges [10], for larger particles up to 750 atoms multilayer icosahedra are formed, while beyond this size the structure becomes fcc [11]. Simulations with the Lennard-Jones (LJ) potential, a reasonable model for noble gases, as well as exhaustive searches of ground state structures confirmed this picture [12–14]. LJ simulations also revealed richer behaviour, especially at finite temperature T, including decahedral structures and surface transitions [15–18]. Our interest is how these structures form out of the liquid state on cooling.

Freezing of a liquid generally occurs through the process of nucleation. This is

accomplished when one of the embryonic crystallites that appear as structural fluctuations in the liquid reaches a sufficient size to overcome the crystal-liquid surface tension that tends to shrink and eliminate small crystalline embryos. Classical Nucleation Theory (CNT) forms the basis of understanding the process qualitatively and provides quantitative predictions for the rate of nucleation. Central to CNT is $\Delta G(n)$, the reversible work required to form an embryo of size n particles of the stable phase within the metastable bulk [19]. However, the predicted rate is highly sensitive to , and therefore to such considerations as the shape of the embryos, the nature of the interface and to the potentially T and curvature dependent surface tension.

The freezing of nanodroplets, i.e., nanoclusters in their liquid form, is complicated by the fact that such small systems can often freeze into more than one structure, for example icosahderal, decahedral or bulk-like fcc and hcp structures. And hence the nucleation process is potentially competitive in nanodroplets [20]. One wonders at what point during the freezing process does differentiation between structures occur and whether CNT provides a reasonable description of the rate at all. These are unresolved questions and their answers are likely system specific.

One study employing simulations of gold nanoparticles found that at sufficient supercooling, CNT predicted a constant or decreasing freezing rate with further supercooling while direct simulations saw the reverse, namely an increasing rate with further cooling [21]. This peculiar result is connected to broader questions regarding the choice of reaction coordinate in describing the nucleation process and the resulting free energy landscape, the description of nucleation when barriers are low and the approach to a possible spinodal-like end to liquid metastability [22]. Spinodal-like nucleation has been suggested to occur for bulk LJ [23], but this idea has been challenged [24, 25].

In this thesis, we use molecular dynamics (MD) simulations to determine the

freezing rate of a droplet consisting of 600 LJ particles. We press into service the mean first-passage time (MFPT) formalism of Reguera and co-workers [26–28] to determine the rate over a broad range of T and at the same time distinguish between free energy and dynamic contributions to the rate, namely the work of forming an n-size embryo and the attachment rate of particles onto embryos. While generally for nanodroplets the surface may play a large role in determining the rate, since a large fraction of particles is near or at the surface of the droplet, crystallization for the present system occurs within the interior. We thus expect CNT as formulated for bulk liquids to hold without the modifications often employed to describe nucleation occurring on the surface [29].

The previous study of this system [30] also revealed that several competing structures, some based on fcc tetrahedra of different sizes, exist within the free energy landscape of the system in the form of basins. However, as the free energy was calculated as a function of global measures of surface and bulk crystallinity, little light was shed on the question of how these different structures arise. The Monte Carlo simulations we carry out in the present work in order to check the ability of the MFPT formalism to determine the work of forming crystallites, also provide some information on the process of structural differentiation.

In terms of contributors to this thesis, I, Shahrazad Malek, carried out all the work under the direction of my supervisor, Dr. Ivan Saika-Voivod. The thesis builds on work done by Mr. Gregory Morrow during his honours research that showed the feasibility of using MFPT for the system.

This thesis is organized as follows. In Chapter 2, we describe Classical Nucleation Theory and the mean first-passage time formalism. In Chapter 3, we describe the simulation methods we use. We detail our results in Chapter 4 and descuss them in Chapter 5. Finally, we list our conclusions in Chapter 6.

Chapter 2

Theoretical Background

2.1 Classical Nucleation Theory

Classical Nucleation Theory (CNT) describes the initial process of phase change in a first-order transformation such as crystallization. Originally formulated for describing liquid condensation within a supersaturated vapour, the formalism is essentially unchanged when used to describe crystal nucleation within a supercooled liquid, i.e., a liquid cooled below the coexistence (melting) temperature. There are essentially three interrelated aspects of the theory. The first deals with the thermodynamics of having a distribution of crystal-like embryos (the stable phase) within the liquid (the metastable phase) and relating this distribution to the work required to form a crystalline *embryo*, within the liquid. The second aspect involves understanding the work of embryo formation in terms of bulk thermodynamic quantities of the liquid and crystal. The third aspect is the rate at which particles attach to or detach from embryos. For describtions of CNT, see Refs. [19, 31–33].

2.1.1 Cluster Distribution

CNT begins with a description of the formation of embryos of the stable phase within the metastable bulk. The thermal motion of particles leads to collisions between them, and this leads to two processes; decay and growth of embryos. The addition of a particle or a small embryo of particles to another embryo is *growth*, while detachment of a particle or a sub-embryo from an embryo is called *decay*. This formation process is essential for a first-order phase transition within a homogeneous system, where an energetically unfavourable interface between the embryo and the surrounding metastable liquid must be achieved first. At some instance in time, a fluctuation resulting from thermal motion will form a so-called *critical embryo* of size n^*. At this size, an embryo is equally likely to grow to very large (macroscopic) sizes or to shrink back into the liquid. Forming this critical embryo marks the beginning of the phase transition. Hence, it is of great interest to calculate the rate of nucleation, that is to say the number of crystalline embryos that cross the n^* threshold per unit time and start to grow.

We consider a system consisting of N_p particles, in which some form crystal-like embryos of different sizes. The total number of these embryos plus the number of leftover liquid particles is denoted N_t. Each embryo is characterized in terms of its size, i.e., the number of particles n that gathered to form the embryo. Denoted by $N(n)$ is the number of embryos in the system that are of size n. The number of liquid particles is given by $N(0)$. The immediate goal is to determine the minimum work required to create a system with a particular *distribution* of embryos, i.e., the free energy difference ΔG between the liquid containing a particular $N(n)$ and the equilibrium liquid.

There are two contributions to $\Delta G(n)$. The first arises from the work required to create a single embryo of size n, $\Delta G(n)$, while the second stems from the different

rearrangements of embryos in the system. If we assume, as is usually done, that embryos are few and far between, and thus generally interact negligibly with each other, this second contribution is given by the ideal entropy of mixing. The number of ways of arranging the N_t liquid-like particles and crystalline embryos distributed according to $N(n)$ is given by,

$$g = \frac{N_t!}{\prod_{n=0}^{h} N(n)!}, \tag{2.1}$$

where h is some upper embryo size limit, presumably not much larger than n^*, and $N_t = \sum_{n=0}^{h} N(n)$. Hence, the entropic contribution σ to ΔG arising from the rearranging of embryos, employing Stirling's Approximation $\log(N!) \cong N \ln N - N$, is,

$$\begin{aligned} \sigma/k_{\mathrm{B}} &= \ln g \\ &\cong N_t \ln N_t - N_t - \sum_{i=0}^{h} N_i \ln N_i + \sum_{i=0}^{h} N_i \\ &= -\sum_{i=0}^{h} N(i) \ln\left(\frac{N(i)}{N_t}\right), \end{aligned} \tag{2.2}$$

where k_{B} is Boltzmann's constant. Armed with this expression, we can write ΔG as,

$$\Delta G = \sum_{n=0}^{h} N(n)\Delta G(n) + k_{\mathrm{B}}T \sum_{n=0}^{h} N(n) \ln\left(\frac{N(n)}{N_t}\right), \tag{2.3}$$

where the first term accounts for the work required to create the embryos, while the second term is the (entropic) work associated with rearranging them. T is the temperature.

As the system tends to minimize its free energy, and the variables $N(j)$ are unconstrained, we can set the derivatives of Eq. 2.3 with respect to each $N(j)$ to zero,

$$\frac{\partial}{\partial N(j)} \Delta G = 0, \tag{2.4}$$

to determine a relationship between $\Delta G(n)$ and $N(n)$, via,

$$\begin{aligned} 0 &= \Delta G(j) - k_{\mathrm{B}}T\left[\frac{\partial N_t}{\partial N(j)}\ln N_t + N_t\left(\frac{1}{N_t}\frac{\partial N_t}{\partial N(j)}\right) - \ln N(j) - \frac{N(j)}{N(j)}\right] \\ &= \Delta G(j) - k_{\mathrm{B}}T\left[\ln N_t + 1 - \ln N(j) - 1\right] \\ &= \Delta G(j) + k_{\mathrm{B}}T\ln\frac{N(j)}{N_t} \\ \beta\Delta G(j) &= -\ln\frac{N(j)}{N_t}, \end{aligned} \tag{2.5}$$

where $\beta = (k_{\mathrm{B}}T)^{-1}$. Formally, this minimization needs to take into account conservation of the total number of particles through the condition $N_p = N(0) + \sum_{n=1}^{h} nN(n)$, but this correction should be negligible so long as the number of crystal-like particles is small compared to the number of liquid-like particles. Assuming that the system is dominated by liquid-like particles and small embryos, i.e., $N_t \approx N_p$, we finally obtain the equilibrium distribution of embryos of size n in terms of the work required to form them,

$$N(n) = N_p \exp\left[-\beta\Delta G(n)\right]. \tag{2.6}$$

2.1.2 Modelling the Free Energy Barrier

The minimum work required to form an embryo of size n, $\Delta G(n)$, is often referred to as the *free energy barrier*, or the *barrier profile*. It can be understood as consisting of two parts, one arising from the chemical potential difference between bulk liquid and bulk crystal, which favours the appearance of the crystal, and a surface tension, which tends to shrink small crystallites [see Fig. 2.1]. When these two thermodynamic driving forces balance at n^*, a maximum in $\Delta G(n)$ occurs. This maximum, $\Delta G(n^*)$, is referred to as the *barrier height* or simply as the *nucleation barrier*. We now proceed to describe $\Delta G(n)$ in the *capilarity approximation*, i.e., in the approximation that the interior of a crystallite and its interface with the liquid are well described by bulk

properties.

Consider an embryo with and spherical surface of radius r. This is an idealized, smooth surface with an effective surface tension with the liquid γ, obtained by averaging in some way over different surface structures. (We are effectively treating this crystallite as an isotropic fliuid.) On traversing the surface from the liquid into the interior, there is an increase in pressure given by the Young-Laplace equation,

$$\begin{aligned} \Delta p &= p_s - p \\ &= \frac{2\gamma}{r}, \end{aligned} \tag{2.7}$$

where p_s and p are the pressures inside the solid embryo and the surrounding liquid, repsectively. We assume that p and T are constant. Thus, the pressure within the crystallite is higher than that of the surrounding liquid.

If we consider a portion of liquid with and without an embryo of size n, the difference in the Gibbs free energy between these two state is precisely $\Delta G(n)$, and it can be shown that [19],

$$\Delta G(n) = \gamma S + (p - p_s)V + [\mu_s(p_s) - \mu_l(p)]n, \tag{2.8}$$

where μ_s and μ_l are the chemical potentials of the crystal and liquid phases, respectively, and V and S are the volume and surface area of the embryo, respectively. It appears that the pressure difference inside and outside the embryo complicates $\Delta G(n)$, but in fact, we can use the relation $d\mu_s = V/n\, dp_s$ (assuming constant per particle volume $v = V/n$ of the effectively incompressible crystal and constant T) to

write,

$$\begin{aligned} \Delta G(n) &= -\Delta\mu\, n + \gamma S \\ &= -\Delta\mu\, n + A\gamma\, n^{2/3}, \end{aligned} \tag{2.9}$$

where $A = \sqrt[3]{36\pi\, v^2}$ for a sphere, and $\Delta\mu = \mu_l - \mu_s > 0$.

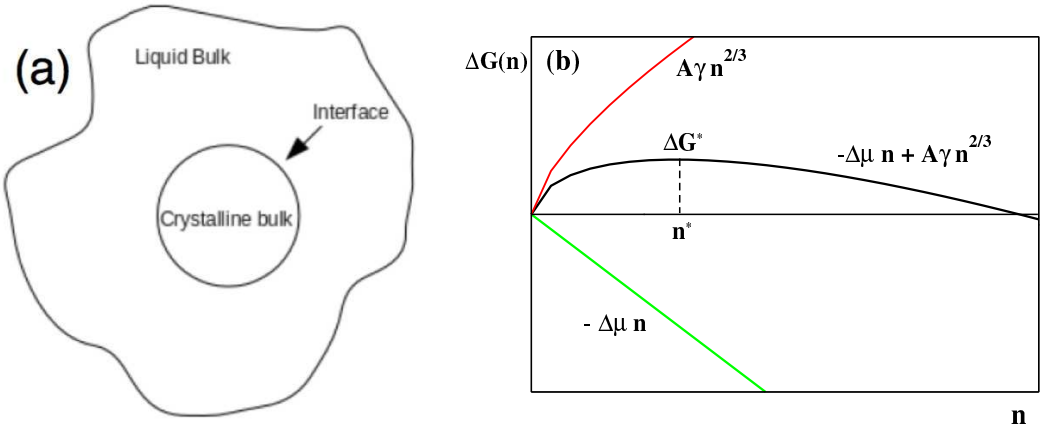

Figure 2.1: (a) A system composed of a crystalline embryo surrounded by a bulk liquid bulk, separated by an interface. (b) Schematic represents the competing contributions of the bulk and surface terms in Eq. 2.9 to $\Delta G(n)$.

In the sense that the system tends to minimize its free energy, we see in Fig. 2.1(b), that for small n, n will tend to decrease, while for large n, n tends to grow. The critical size n^* is found by setting $\Delta G'(n^*) = 0$, and obtaining,

$$n^* = \frac{8\pi}{27}\left(\frac{A\gamma_s}{\Delta\mu}\right)^3, \tag{2.10}$$

and by substituting this into Eq. 2.9, obtaining,

$$\beta\Delta G(n^*) = \frac{4(\beta A\gamma)^3}{27(\beta\Delta\mu)^2}. \tag{2.11}$$

This implies that at the maximum point of $\Delta G(n)$, the embryo is unstable and tends

to either shrink or grow.

2.1.3 The Nucleation Rate

We will follow the CNT formalism to derive the nucleation rate presented in [19]. CNT assumes that a distribution of embryos is established through a balance of single particle additions and detachments from embryos. For example, an n-sized embryo forms through the addition of a single particle to an embryo of size $n-1$, but an n sized embryo may also lose a particle and hence shrink to size $n-1$. An n-sized embryo may also form from an $(n+1)$-sized embryo losing a particle. We call $J(n)$ the difference between the rate of forming an embryo of size n through a particle addition and the rate of losing an n-sized embryo through a detachment,

$$J(n) \quad = \quad f(n-1)F(n-1)\Gamma - f(n)F(n)\alpha, \tag{2.12}$$

where $f(n)$ is the number of embryos of size n during nucleation (which differs from the equilibrium distribution), $F(n)$ is the surface area of an n-embryo, Γ is the flux of particles onto an embryo's surface (number of attachments per unit time, per unit area), and α is the detachment flux. As Γ and α are both per area quantities, they are assumed to be independent of n.

We can write the time rate of change of the distribution of embryos as,

$$\frac{\partial f(n,t)}{\partial t} \quad = \quad J(n) - J(n-1), \tag{2.13}$$

which follows from the definition of $J(n)$. But now we consider the so-called *steady-state* nucleation regime, where the rate of formation of critical embryos is constant in time, or equivalently, that the distribution $f(n)$ is constant in time (at least for small

n, i.e. not much bigger than n^*) and $J_{\rm CNT} \equiv J(n)$ is independent of n.

Determining Γ and α is generally difficult, so the assumption is made that these fluxes are the same whether they are occurring in equilibrium or during steady-state nucleation. At equilibrium, $J(n) = 0$, and hence we can write α in terms of the equilibrium distribution of embryos we considered above,

$$\begin{aligned} N(n-1)F(n-1)\Gamma &= N(n)F(n)\alpha \\ \alpha &= \frac{\Gamma N(n-1)F(n-1)}{N(n)F(n)}. \end{aligned} \tag{2.14}$$

Using this expression for α, we obtain,

$$J_{CNT} = \Gamma F(n-1)N(n-1)\left[\frac{f(n-1)}{N(n-1)} - \frac{f(n)}{N(n)}\right], \tag{2.15}$$

which is the nucleation rate, i.e., the number of embryos that surpass critical size per unit time.

While in principle $J_{\rm CNT}$ can be determined from Eq. 2.15 for any value of n, we can simplify the equation by summing over n from 2 to χ, where χ is some unspecified embryo size significantly larger than n^*, to obtain,

$$J_{CNT} = \frac{\frac{f(1)}{N(1)} - \frac{f(\chi+1)}{N(\chi+1)}}{\sum_{n=1}^{\chi} \frac{1}{\beta F(n)N(n)}}, \tag{2.16}$$

reducing our reliance on $f(n)$ in determining $J_{\rm CNT}$. Moreover, we expect that the equilibrium and steady-state distributions to be the same for very small embryos, and hence the ratio $\frac{f(1)}{N(1)} = 1$. We also assume that $f(\chi+1) \ll N(\chi+1)$ precisely because steady-state nucleation deals with the regime where the equilibrium distribution for large n is still far from being achieved, i.e., the new phase has not yet formed. With

these simplifications,

$$J_{CNT} = \frac{1}{\sum_{n=1}^{\chi} \frac{1}{\Gamma F(n) N(n)}}. \tag{2.17}$$

Approximating this sum with an integral and writing $N(n)$ in terms of Eq. 2.6, we write,

$$J_{CNT} = \Gamma N_p \left[\int_{n \ll n^*}^{n \gg n^*} \exp\left(\frac{\beta \Delta G(n)}{kT}\right) \frac{1}{F(n)}\, dn \right]^{-1}, \tag{2.18}$$

where the limits reflect the fact that, because of the exponential, the overwhelming contribution to the integral comes from the portion of $\beta\Delta G(n)$ near the maximum at n^*. In this case, we can expand $\beta\Delta G(n)$ to second order around n^*,

$$G(n) \approx G(n^*) + G'(n^*)(n - n^*) + \frac{1}{2} G''(n^*)(n - n^*)^2, \tag{2.19}$$

and approximate $F(n)$ with its value at n^*, to obtain,

$$\begin{aligned} J_{CNT} &\approx \Gamma N_t F(n^*) \exp\left[\frac{-\Delta G(n^*)}{k_{\mathrm{B}} T}\right] \\ &\quad \times \left[\int_{-\infty}^{\infty} \exp\left\{ -\frac{1}{2kT} \left[-G''(n^*)\right] (n - n^*)^2 \right\} dn \right]^{-1} \\ &= \left\{\Gamma F(n^*)\right\} \times \left[\sqrt{\frac{-\Delta G''(n^*)}{2\pi k_{\mathrm{B}} T}} \right] \times \left\{ N_p \exp\left[\frac{-\Delta G(n^*)}{k_{\mathrm{B}} T}\right] \right\} \\ &= N_p Z f_{crit}^{+} \exp\left[-\beta \Delta G^*\right] \end{aligned} \tag{2.20}$$

where f_{crit}^{+} is the product $\Gamma \times F(n^*)$, and represents the frequency of the attachment of a single particle to the critical embryo, $N(n^*) = N_p \exp\left[-\beta\Delta G^*\right]$ is the equilibrium number of critical embryos, and the Zeldovich factor, given Eq. 2.9 in evaluating

the second derivative, is $Z = \frac{3}{4\sqrt{\pi}} \frac{(\beta\Delta\mu)^2}{(\beta A\gamma)^{3/2}}$ and can be interpreted as the factor that corrects for the fact that the actual number of critical embryos $f(n^*)$ differs from the equilibrium number (as described first by Zeldovich in 1942 [19]).

The simplest model for the T-dependence of J_{CNT} is obtained by combining Eqs. 2.20 and 2.9, along with assuming γ and A constant. By further assuming a constant enthalpy difference ΔH between the liquid and crystal phases as T decreases at constant pressure p, one obtains,

$$\beta\Delta\mu = \frac{\Delta H}{N_p k_{\mathrm{B}}} \frac{T_m - T}{T T_m}, \tag{2.21}$$

where T_m is the T at which the chemical potentials of the liquid and crystal phases are equal and at which point J_{CNT} is zero. For bulk phases, T_m is the melting temperature. Additionally, one assumes a simple Arrhenius T dependence of the critical attachment rate,

$$f^{+}_{\mathrm{crit}} = f_0 \exp\left(-\frac{C}{T}\right), \tag{2.22}$$

where $k_{\mathrm{B}}C$ is an activation free energy and f_0 is a constant. Combining all these approximations results in [34],

$$J_{CNT}(T) = \lambda \frac{(T_m - T)^2}{\sqrt{T}} \exp\left[-\frac{C}{T} - \frac{B}{T(T_m - T)^2}\right], \tag{2.23}$$

which predicts a maximum rate to occur even in the absence of considerable slowing down of dynamics owing to a possibly large value of C. The simple modelling employed here implies that the barrier to nucleation is,

$$\beta\Delta G^* = \frac{B}{T(T_m - T)^2}, \tag{2.24}$$

and therefore has a minimum at $T_m/3$, which tends to maximize the rate, before

diverging as T approaches zero. In terms of the physical quantities ΔH, T_m, f_0, A and γ, the parameters λ and B in the model are given by,

$$\lambda = f_0 N_p \frac{3}{4\sqrt{\pi k_{\mathrm{B}}}} \frac{1}{(A\gamma)^{3/2}} \left(\frac{\Delta H}{N_p}\right)^2 \frac{1}{T_m^2}, \tag{2.25}$$

$$B = \frac{4}{27} \frac{(A\gamma)^3}{k} \left(\frac{N_p}{\Delta H}\right)^2 T_m^2. \tag{2.26}$$

In this thesis, we first obtain the rate as a function of T and treat λ, T_m, B and C in Eq. 2.23 as fitting parameters. We then compare against independent estimates of the underlying physical quantities.

2.2 $n_{\max}$ as the Order Parameter

As is now common in simulation studies of nucleation, we employ the size of the largest embryo in the system $n_{\max}$ as a reaction coordinate. Once an embryo definition is set, every system configuration can be uniquely assigned a value of $n_{\max}$, and hence the (configurational part) of the partition function can be written as a sum of restricted partition functions,

$$Q = \sum_{n=0}^{h} Q(n), \tag{2.27}$$

where as before, h is a constraint on the largest allowable embryo size used to formally define the metastable state, and,

$$Q(n) = \sum_{c \in n} \exp\left(-\beta U_c\right), \tag{2.28}$$

is the partition function, here written for the canonical ensemble, where U_c is the potential energy of configuration c, restricted to those configurations that have a largest embryo of size n. From this grouping of the partition function, we define the

free energy $\Delta\tilde{F}(n)$ as,

$$\beta\Delta\tilde{F}(n) = -\ln\left[\frac{Q(n)}{Q}\right] = -\ln\tilde{P}_{\max}(n), \tag{2.29}$$

where $\tilde{P}_{\max}(n)$ is the probability that the largest embryo in the system is of size n. $\Delta\tilde{F}(n)$ is interpreted as the reversible work required to force the metastable state defined by h in Eq. 2.27 into a state in which the largest embryo is of size n. One subtlety remains, in that a transition state theory (TST) prediction for the rate requires the equilibrium probability of being at the transition state (critical embryo size), *given that the system starts in the metastable liquid*. This implies the choice of $h = n_F^*$, the point at which $\Delta\tilde{F}(n)$ has it local maximum, resulting in

$$Q_{\text{liq}} = \sum_{n=0}^{n_F^*} Q(n), \tag{2.30}$$

and a renormalization of probabilities that were calculated for $h > n_F^*$,

$$P_{\max}(n) = \frac{\tilde{P}_{\max}(n)}{\sum_{i=0}^{n_F^*}\tilde{P}_{\max}(i)}. \tag{2.31}$$

This is useful since the value of n_F^* is unknown prior to running simulations. With this normalization,

$$\sum_{n=0}^{n_F^*} P_{\max}(n) = 1. \tag{2.32}$$

Thus, we define

$$\beta\Delta F(n) = -\ln\left[\frac{Q(n)}{Q_{\text{liq}}}\right] = -\ln P_{\max}(n). \tag{2.33}$$

For relatively large barrier heights, large embryos are rare, i.e., there is only one large embryo in the system if there is one at all. In this case, the probability of there being an embryo of size n in the system, the probability that the largest embryo is

of size n and the average number of embryos of size n are all equal. This becomes immediately obvious when constructing related histograms during the simulations. In this regime, $P_{\max}(n) = N(n)$ (and both are small). The TST rate expression when there is a free energy barrier present is,

$$J_{\mathrm{TST}} = f^{+}(n_F^*) Z_F \exp\left[-\beta \Delta F^*\right], \tag{2.34}$$

where n_F^*, the Zeldovich factor $Z_F = \left[\beta \Delta F''(n_F^*)/(2\pi)\right]^{1/2}$ and $f^{+}(n_F^*)$, the generalized diffusion coefficient at the critical state, become equal to n^*, Z and f_{crit}^{+} at sufficiently high barriers, respectively, and $\beta \Delta F^* = \beta \Delta F(n_F^*)$. f_{crit}^{+} in Eq. 2.20 is the attachment rate of particles to an embryo of critical size, while $f^{+}(n_F^*)$ tracks changes in the size of the largest embryo at critical size in the system. The two are the same so long as the largest embryo in the system is the only embryo near the critical size. Again, when barriers are high, the equalities $n^* = n_F^*$ and $P_{\max}(n) = N(n)$ near n^* imply that $\beta \Delta G^* = \beta \Delta F^* + \ln N_p$, and this is consistent when comparing Eqs. 2.20 and 2.34. However, there is no reason why this should hold when barriers become low.

It is generally the case that $\Delta F(n)$ possesses a minimum at $n_{\min}$, the most likely largest embryo size in the system. It is tempting to formulate Eq. 2.34 in terms of the free energy difference,

$$\beta \Delta F_{\min}^* = -\ln \left[\frac{\tilde{P}_{\max}(n_F^*)}{\tilde{P}_{\max}(n_{\min})} \right] = \beta \Delta F^* - \beta \Delta F(n_{\min}). \tag{2.35}$$

This is incorrect in terms of rate prediction, but becomes approximately correct in the high barrier regime when $P_{\max}(n_{\min}) \approx 1$, or when $\tilde{P}_{\max}(n_{\min})$ dominates with sum in the denominator of Eq. 2.31.

The identification of $\Delta F_{\min}^* \to 0$ as a spinodal has been shown to be incorrect [24], but it nonetheless marks the point at which the system ceases to possess a basin in the

free energy and has therefore lost formal metastability. For bulk systems of finite-size, this marks the point at which phase change proceeds through the monotonic increase in size of the largest embryo in the system with time, i.e., because the system is large enough, it becomes probable that it possesses an embryo of critical size within the time for $\sim n_F^*$ particle attachments to occur. Phase transformation of the sample thus proceeds through growth-limited nucleation. However, the metastable phase has not lost inherent metastability as work is still required to form an embryo. For systems such a our nanodroplets, it is perhaps not meaningful to distinguish between phase and system, but we nonetheless expect that the loss of metastability occurring at $\Delta F^*_{\min} = 0$ be actualized through a growth-limited nucleation mechanism with a transformation rate given, at least approximately, by Eq. 2.20. A true kinetic spinodal, i.e., a loss of stability on the particle level, should occur when ΔG^* vanishes.

2.3 The Mean First-Passage Time Formalism

In 2007, Reguera and his co-workers derived a new method to analyze simulations of activated processes [26–28]. The new method originates from the concept of mean first-passage time (MFPT) within transition state theory [35], and provides a direct path to calculate the reaction rate, the transition state, and Zeldovich factor from the kinetics rather than thermodynamics. Here we provide an overview of the derivation of some of the results.

The MFPT $\tau(b)$ for any quantity x following a stochastic process that begins at time $t = 0$ with a value of x_0, is the mean time required for the quantity to first reach an absorbing boundary at $x = b$, given some reflecting domain boundary at $x = a$. For example, for the nucleation process, the quantity in question is the size of largest embryo in the system, $n_{\max}$; if $n_{\max}$ reaches zero, it can simply grow to positive

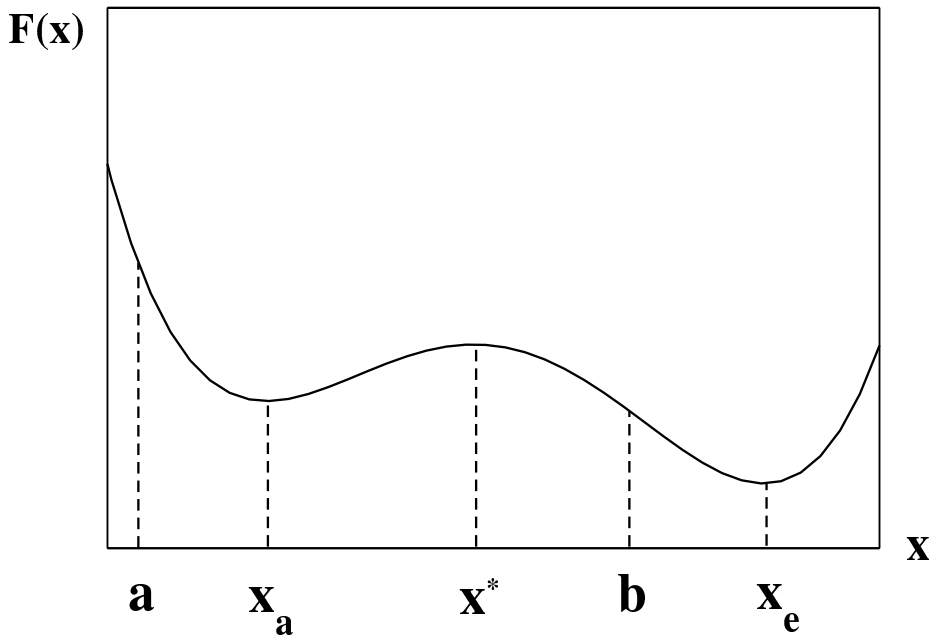

Figure 2.2: Double well potential. x_e is represents the equilibrium state, b is the absorbing parameter, x^* is the critical state, x_a is metastable state, and a is the reflecting point.

values later (so $a = 0$), and once it reaches a value significantly larger than n^*, it will typically grow rapidly to macroscopic sizes and so $n_{\max}$ can be considered "absorbed" if it reaches a value $b \gg n^*$. This scenario is depicted schematically in Fig. 2.2. The mean first-passage time for a one dimensional transition state is [26, 35]

$$\tau(b) = \int_{x_0}^{b} \frac{1}{D_0} dy \exp[\beta \Delta F(y)] \int_{a}^{y} dz \exp[-\beta \Delta F(z)], \tag{2.36}$$

where D_0 is the generalized diffusion coefficient, assumed to be constant here, and $x(t)$ is the stochastic process bounded between a to b.

Taking a derivative of Eq. 2.36 with respect to b, we get

$$\frac{\partial \tau(b)}{\partial b} = \frac{1}{D_0} \exp[\beta \Delta F(b)] \int_{a}^{b} dz \exp[-\beta \Delta F(z)], \tag{2.37}$$

and the second derivative gives,

$$\frac{\partial^2 \tau(b)}{\partial b^2} = \frac{1}{D_0} + \beta \Delta F'(b) \frac{\partial \tau(b)}{\partial b}. \tag{2.38}$$

At the saddle point of the free energy curve, i.e., at the transition state $b = x^*$, $\Delta F'(b) = 0$, and hence,

$$\frac{\partial^2 \tau(b)}{\partial b^2}\Big|_{b=x^*} = \frac{1}{D_0}, \tag{2.39}$$

which simply yields the kinetic prefactor D_0.

Now, starting from Eq. 2.36, the free energy $\Delta F(y)$ is peaked around the maximum point x^*, Fig. 2.2. This suggest expanding $\Delta F(y)$ around x^*,

$$\begin{aligned} \tau(b) &= \frac{1}{D_0(x^*)} \int_a^{x^*} dz \exp\left[-\beta \Delta F(z)\right] \\ &\quad \times \int_{x_0}^{b} dy \exp[\beta \Delta F(x^*) - \frac{1}{2} \left|\Delta F''(x^*)\right| (y - x^*)^2 \,, \end{aligned} \tag{2.40}$$

which allows us to integrate y,

$$\begin{aligned} \tau(b) &= \frac{1}{D_0(x^*)} \exp[\beta \Delta F(x^*)] \\ &\quad \times \int_a^{x^*} dz \exp[-\beta \Delta F(z)] \frac{1}{2 \times \sqrt{\left|\Delta F''(x^*)\right|/2\pi KT}} \\ &\quad \times \left(1 + erf\left(\sqrt{\frac{|\Delta F''(x^*)|}{2KT}}(b - x^*)\right)\right). \end{aligned} \tag{2.41}$$

At the transition state x^* the MFPT is simplified to,

$$\begin{aligned} \tau(x^*) &= \frac{1}{D_0(x^*)} \exp[\beta \Delta F(x^*)] \\ &\quad \times \int_a^{x^*} dz \exp[-\beta \Delta F(z)] \frac{1}{2 \times \sqrt{\left|\Delta F''(x^*)\right|/2\pi KT}} \equiv \frac{1}{2J}, \end{aligned} \tag{2.42}$$

where J is the nucleation rate, and it is given by the inverse of twice average time to reach the transition state, $J = [2\tau(x^*)]^{-1}$. This is so since at x^*, there is a 50% chance of falling to either side.

With the result from Eq. 2.42, and identifying x^* with n_F^*, b with n (size of the largest embryo) and $\beta\Delta F$ with Eq. 2.33, we can simplify Eq. 2.41 to,

$$\tau(n) \quad = \tfrac{\tau_J}{2}(1 + erf(Z\sqrt{\pi}(n - n_F^*))) \tag{2.43}$$

where $\tau_J = 1/J$ and $c = \sqrt{|\Delta F''(n_F^*)|/2k_{\mathrm{B}}T}$ is the local curvature at the top of the barrier. Under relatively high barriers, we can fit the MFPT data with eq. 2.43, and in a rather simple way, obtain the three of the most important parameters of the activated processes: the nucleation rate J, the location of the transition state n_F^*, and Zeldovich factor $Z = c/\sqrt{\pi}$.

2.4 Reconstructing the Free Energy Landscape from the Steady-State

The MFPT method allows one to calculate the equilibrium free energy $\Delta F(n)$ between $n = 0$ and $n = b$, an absorbing boundary, from steady-state nucleation data. The value of $b > n_F^*$ should be large enough so that growth of the embryo is inevitable, i.e., that once $n_{\max}$ reaches b, it would be highly unlikely to return to n_F^*.

Starting from Fokker-Plank equation (derived in Appendix A),

$$\begin{aligned} \frac{\partial P_{\max}(n,t)}{\partial t} &= \frac{\partial}{\partial n}\left[D(n)e^{-\beta\Delta F(n)}\frac{\partial}{\partial n}(P(n,t)_{\max}e^{\beta\Delta F(n)}\right] \\ &= -\frac{\partial J(n,t)}{\partial n}, \end{aligned} \tag{2.44}$$

where n is the size of the largest embryo in the system, $P_{\max}(n)$ is the non-equilibrium probability distribution for n and is normalized to unity over the interval $0 \leq n \leq b$, $J(n,t)$ is the so-called flux, and $\Delta F(n)$ is the free energy landscape. When the system reach steady-state nucleation, $\partial P(n,t)^{\rm st}_{\max}/\partial t = 0$, i.e., $P_{\max}(n,t) = P^{\rm st}_{\max}(n)$, and $\partial J(n,t)/\partial n = 0$, i.e., J is constant and is now the nucleation rate, or the flux of embryos growing past n^*_F. Eq. 2.44 becomes

$$J = -D(n)e^{-\beta\Delta F(n)}\frac{\partial}{\partial n}(P^{\rm st}_{\max}(n)e^{\beta\Delta F(n)}) \tag{2.45}$$

Taking the drivative in Eq. 2.45, we get,

$$J \;=\; -D(n)\left[\frac{\partial}{\partial n}P^{\rm st}_{\max}(n) - P^{\rm st}_{\max}(n)\frac{\partial}{\partial n}\left(\beta\Delta F(n)\right)\right]. \tag{2.46}$$

At this point, we can integrate Eq. 2.46 and rearrange terms to obtain,

$$\beta\Delta F(n) \;=\; -\ln P^{\rm st}_{\max}(n) - J\int_0^n \frac{dx'}{D(x')P^{\rm st}_{\max}(x')} + C \tag{2.47}$$

where C is the intergration constant and can be determined from a suitable reference state.

However, Eq. 2.47 needs pre-knowledge of the steady-state rate J and $D(n)$ to reconstruct the free energy from the steady-state probability, and so is not immediately useful. We note that Eq. 2.47 reduces to the standard Boltzmann formula at equilibrium, $P_{eq}(n) = e^{-\beta\Delta F(n)}$.

To evaluate ΔF and $D(n)$ at the same time, we start from Eq. 2.37 with $D(n)$ now explicitly a function of n,

$$D(n)\frac{\partial\tau(n)}{\partial n} \;=\; e^{\beta\Delta F(n)}\int_0^b dz e^{-\beta\Delta F(z)}. \tag{2.48}$$

Taking the natural logarithm of Eq. 2.48 and taking the second derivative, we get,

$$\frac{\partial}{\partial n}\left(\ln\left[D(n)\frac{\partial\tau(n)}{\partial n}\right]\right) = \frac{\partial}{\partial n}\left(\beta\Delta F(n)\right) + \frac{e^{-\beta\Delta F(n)}}{\int_0^b dz e^{-\beta\Delta F(z)}}. \tag{2.49}$$

The argument in the LHS is exactly Eq. 2.48, and by denoting $B_F(n) = D(n)\frac{\partial\tau(n)}{\partial n}$, Eq. 2.49 becomes,

$$\beta\Delta F(n) = \ln(B_F(n)) - \int_0^b \frac{dx'}{B(x')} + C'. \tag{2.50}$$

Now, taking the derivative of Eq. 2.47 with respect to n and combining it with Eq. 2.49, we get

$$\frac{\partial(B_F(n)P^{\rm st}_{\rm max}(n))}{\partial n} = P^{\rm st}_{\rm max}(n) - J\frac{\partial\tau(n)}{\partial n}. \tag{2.51}$$

This equation can be integrated to yield,

$$B_F(n) = \frac{1}{P^{\rm st}_{\rm max}(n)}\left[\int_0^n P^{\rm st}_{\rm max}(x')dx' - \frac{\tau(n)}{\tau(b)}\right], \tag{2.52}$$

noting that if post-critical embryo growth is fast, then $\tau(b) = \tau_J$, and $J = 1/\tau(b)$ [26, 27].

We note that $B_F(n)$ near b is noisy, as the quantity in square brackets in Eq. 2.52 approaches zero as n approaches b and $P^{\rm st}_{\rm max}(b)$ is small and tends to suffer from poor statistics. We determine $P^{\rm st}_{\rm max}(n)$ using all data from the simulation time series up to the point at which $n_{\rm max}$ first crosses b. The parameter C' is set by normalizing according to Eq. 2.32. In the event that $\beta\Delta F(n)$ ceases having a maximum, and therefore n^*_F is not defined, C' is determined by setting $\beta\Delta F(2) = -\ln\left[P^{\rm st}_{\rm max}(2)\right]$ [28], which

assumes that for small embryo sizes, the equilibrium and steady-state distributions are the same. In our use of Eqs. 2.50 and 2.52, we replace integrations with sums since the order parameter is a whole number.

We would like to point out a handy (new) result that, assuming $\tau(n)$ follows Eq. 2.43, allows a way of reconstructing the equilibrium free energy that is simpler than Eq. 2.50. We begin by relating the equilibrium and steady-state distributions via an unknown function $X(n)$,

$$P^{\rm st}_{\rm max}(n) = X(n) P_{\rm max}(n), \tag{2.53}$$

where we expect that $X(n) \approx 1$ for small n and $X(n) \approx 0$ for $n \gg n^*_F$. Combining this ansatz with the expression for the steady-state nucleation rate from the Fokker-Planck equation that forms the basis of the MFPT method, one obtains a differential equation for $X(n)$,

$$J = -f^+(n) e^{-\beta \Delta F(n)} \frac{\partial}{\partial n} \left[P^{\rm st}_{\rm max}(n) e^{\beta \Delta F(n)} \right] \tag{2.54}$$

$$-\frac{J}{f^+(n) e^{-\beta \Delta F(n)}} = \frac{\partial}{\partial n} \left[\frac{P^{\rm st}_{\rm max}(n)}{P_{\rm max}(n)} \right] = \frac{\partial}{\partial n} X(n). \tag{2.55}$$

Solving this equation near n^*_F, after expanding $\Delta F(n)$ to second order as is usually done for high barriers, assuming $f^+(n) = f^+_{\rm crit}$ and using Eq. 2.34 for J, we obtain,

$$X(n) = const - \frac{1}{2} \, {\rm erf} \left[Z_F \sqrt{\pi} \, (n - n^*_F) \right] \tag{2.56}$$

$$\approx \frac{1}{2} \left(1 - {\rm erf} \left[Z_F \sqrt{\pi} \, (n - n^*_F) \right] \right) \tag{2.57}$$

$$\approx 1 - \frac{\tau(n)}{\tau_J}, \tag{2.58}$$

where we have used Eq. 2.43 and the expectation that $X(n) \approx 1$ for small n after

assuming that $n^* \gg 1$. Similar and identical equations relating steady-state and equilibrium distributions in terms of Z_F have been derived before, but the MFPT formalism provides a convenient route and expresses $X(n)$ in terms of $\tau(n)$. From Eq. 2.58, we can write down,

$$\beta\Delta F(n) = -\ln\left[P^{\rm st}_{\rm max}(n)\right] + \ln\left[1 - \frac{\tau(n)}{\tau_J}\right], \tag{2.59}$$

which should be applicable to simulation results whenever Eq. 2.43 holds.

Approximating $\beta\Delta F(n) \approx \beta\Delta F^* - Z_F^2\pi(n - n_F^*)^2$ near the top of the barrier and expanding Eq. 2.59 to second order results in,

$$\begin{aligned} -\ln\left[P^{\rm st}_{\rm max}(n)\right] &\approx \beta\Delta F^* + \ln 2 + 2Z_F(n - n_F^*) \\ &- (\pi - 2)\, Z_F^2\, (n - n_F^*)^2\,, \end{aligned} \tag{2.60}$$

which, in principal, provides a way of obtaining Z_F, n_F^* and $\beta\Delta F^*$ from the steady-state probability by fitting the nearly linear portion of $-\ln\left[P^{\rm st}_{\rm max}(n)\right]$.

Chapter 3

Methodology

We employ molecular dynamics (MD) and Monte Carlo (MC) simulations to study our Lennard-Jones droplet. A thorough description of these techniques can be found in Refs. [36] and [37]. Here we provide a brief overview of these methods and how we use them to obtain our results. We also describe the system we are simulating, as well as how we determine the crystallinity within the liquid.

3.1 Molecular Dynamics Simulations

We consider a system of N_p particles whose pairwise interaction with each other is governed by the Lennard-Jones (LJ) pair potential energy,

$$u(r) = 4\epsilon \left[\left(\frac{\sigma}{r} \right)^{12} - \left(\frac{\sigma}{r} \right)^{6} \right]. \tag{3.1}$$

The parameters ϵ and σ set the energy and length scales of the interaction. As shown in Fig. 3.1, the potential has a minimum of depth ϵ at a distance of $2^{1/6}\sigma \approx 1.12\sigma$, a very steep slope at distances near $r = \sigma$ that models the strong repulsion felt as the electron clouds begin to overlap, and an weak attraction due to the dipole moments

that two neutral atoms induce in each other. Although the LJ interaction models noble gas atoms reasonably well, its popularity stems from its simplicity and the generic features it possesses. It serves as a model potential for understanding general physical properties of condensed matter.

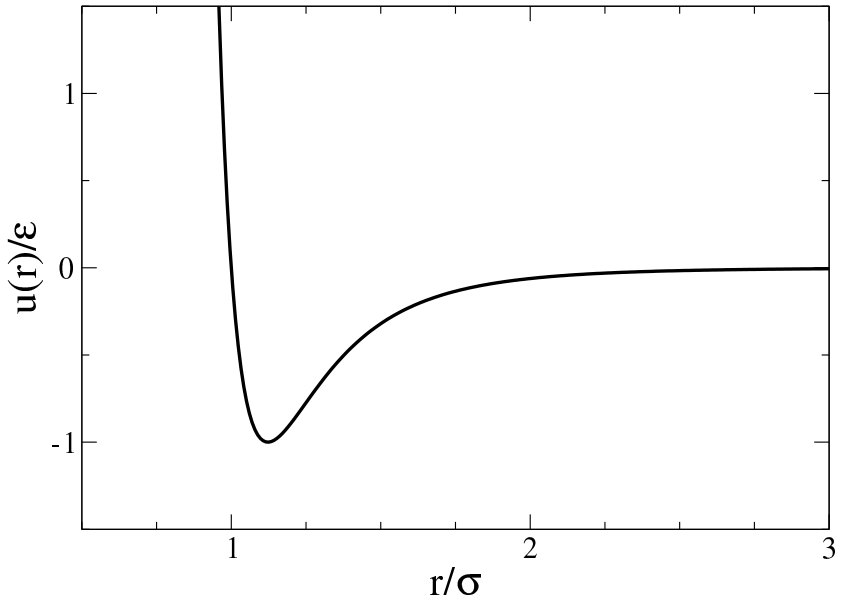

Figure 3.1: The Lennard-Jones pair potential shows generic features of atomic interactions: short range repulsion, long range attraction with a preferred separation defining a bond length. The axes are normalized by Lennard-Jones parameters in Eq. 3.1.

The force on particle i due to particle j is given by,

$$\mathbf{f}_{ij} = -u'(r_{ij})\frac{\mathbf{r}_{ij}}{r_{ij}}, \tag{3.2}$$

where $\mathbf{r}_{ij}$ is the displacement vector pointing from j to i and r_{ij} is the distance between the particles. The net force on particle i is then given as a sum over all such pair forces,

$$\mathbf{f}_i = \sum_{j \neq i}^{N_p} \mathbf{f}_{ij}. \tag{3.3}$$

Solving Newton's Second Law for each particle of the N_p particles,

$$m_i \ddot{\mathbf{r}}_i = \mathbf{f}_i, \tag{3.4}$$

where m_i is the mass of particle i, amounts to solving a system of $3N_p$ (in three dimensions) coupled, non-linear, second order ordinary differential equations. To accomplish this integration, fast, time-reversible, energy-conserving algorithms are preferred, such as the leap-frog algorithm we present next.

As its name suggests, the leap-frog finite-difference algorithm solves for the positions $\mathbf{r}$ and velocities $\mathbf{v}$ in a way that always leaves one of the quantities half a time step ahead of the other. The algorithm reads,

$$\mathbf{r}(t+\delta t) = \mathbf{r}(t) + \delta t\, \mathbf{v}(t+\frac{\delta t}{2}) \tag{3.5}$$

$$\mathbf{v}(t+\frac{\delta t}{2}) = \mathbf{v}(t-\frac{\delta t}{2}) + \delta t\, \mathbf{f}(t)/m. \tag{3.6}$$

To begin, $\mathbf{f}(t)$ is calculated, as it only depends on $\mathbf{r}(t)$. Subsequently, Eq. 3.6 is solved to provide $\mathbf{v}(t+\frac{\delta t}{2})$ as input into Eq. 3.5. Obtaining $\mathbf{r}(t+\delta t)$ allows one then to obtain $\mathbf{f}(t+\delta t)$ and the cycle repeats.

The velocity at time t is calculated by,

$$\mathbf{v}(t) = \frac{1}{2}\left(\mathbf{v}(t+\frac{\delta t}{2}) + \mathbf{v}(t-\frac{\delta t}{2})\right), \tag{3.7}$$

which is required to estimate the total energy,

$$\mathbf{E}(t) = \mathbf{U}(t) + \mathbf{K}(t), \tag{3.8}$$

where the system potential energy is,

$$U = \sum_{i=1}^{N_p-1} \sum_{j>i}^{N_p} u(r_{ij}), \tag{3.9}$$

and the system kinetic energy is

$$K = \frac{1}{2} \sum_{i=1}^{N_p} m_i v_i^2. \tag{3.10}$$

Eqs. 3.5 and 3.6 as they are will conserve mechanical energy. However, they can be modified to simulate conditions of constant T instead. The conceptually simplest method to implement this is to periodically rescale velocities so as to satisfy the Equipartition Theorem for the kinetic energy,

$$\frac{3}{2} N_p k_\mathrm{B} T = K. \tag{3.11}$$

However, although this will achieve the desired average T, the fluctuations in, say, the potential energy, will not follow the canonical ensemble. More sophisticated methods, for example based on extending the Lagrangian with additional degrees of freedom that couple to a heat bath, such as the Nosé-Hoover thermostat algorithm, are required to generate canonical fluctuations.

3.2 Monte Carlo

In contrast to MD simulations, Monte Carlo (MC) methods do not mimic the microscopic motion of particles based on forces. Rather, they employ random trial displacements together with carefully crafted acceptance criteria in order to recover rigorously the statistical ensemble in which the simulation takes place. Here we present the

Metropolis algorithm, which is the original and still most commonly used algorithm for simulating condensed matter systems.

To generate a new microstate of the system, a randomly chosen particle in the system is given a random trial displacement, with each spatial component of the displacement chosen uniformly between $-dr_{\max}$ and $dr_{\max}$. The parameter $dr_{\max}$ is adjusted by the programmer, as we discuss below. The new trial position of the particle is accepted with a probability that depends on the change in the potential energy of the system, and is given by,

$$P_{\text{accept}}(r_i^{\text{trial}}) = \begin{cases} 1 & \text{if } U_{\text{current}} \geq U_{\text{trial}} \\ \exp\left[-\beta(U_{\text{trial}} - U_{\text{current}})\right] & \text{if } U_{\text{current}} < U_{\text{trial}}. \end{cases}$$

That is, trail moves that lower the potential energy are always accepted, while trial moves that increase the potential energy are accepted with a finite probability that is larger at higher T. This simple acceptance rule exemplifies the battle between entropy and energy, in that although energetically poor moves have a low acceptance probability, there are typically many more possible ways of choosing such a move compared to choosing an energetically downhill move at random. On a practical note, determining $U_{\text{trial}} - U_{\text{current}}$, i.e., the change in system energy as a result of the single particle trial displacment, only the change in the interaction energy of the one particle needs to be calculated, as all other interactions are left unchanged.

If the trial move is rejected, then the current configuration is kept (i.e., its properties are counted again in any average being calculated), and is used as the starting point for the next trial move. If the trial move is accepted, the new configuration replaces the current one and its properties are used in determining any ensemble average.

Since $dr_{\max}$ controls the size of particle displacement, it is necessary to chose an

optimal value for it. Otherwise, the simulation becomes costly and inefficient. If $dr_{\max}$ is too small, most trial moves will be accepted since energy changes will be small, but the exploration of configurational space will be slow. If $dr_{\max}$ is too big, then trial moves are likely to result in unfavourable interactions, leading to near certainty of rejection. Often, $dr_{\max}$ is adjusted during run to maintain an acceptance frequency near 0.5.

3.3 Umbrella Sampling

The Metropolis algorithm is fine for determining average system properties at given thermodynamic conditions. However, in studying nucleation, the formation of a critical embryo is typically a highly unfavourable event, energetically speaking, and umbrella sampling MC provides a way of forcing the system to sample configurations that would otherwise be observed only rarely.

In our case, we carry out umbrella sampling MC simulations to determine the works defined in Eqs. 2.5 and 2.33 more directly that what MFPT affords. When barriers are reasonably high, we make use of a biasing potential, or constraint,

$$\phi(n_{\max}) = \frac{1}{2}\kappa(n_{\max} - n_0)^2,$$

where $\kappa = 0.00625\epsilon$ determines the strength of the constraint and n_0 is the target largest crystalline embryo size. The MC procedure consists of first noting at iteration step i the value of the constraint for a configuration o, ϕ_o, and then generating an unbiased MC trajectory in the canonical ensemble with the Metropolis algorithm for 10 displacement attempts per particle to arrive at a new configuration w with a value of the constraint potential ϕ_w. The new configuration is accepted (w becomes the configuration at iteration $i+1$) with probability $\max\left[1, \exp\left(\beta\phi_o - \beta\phi_w\right)\right]$. Otherwise,

o remains the configuration at iteration $i+1$.

Carrying out biased simulations for several values of n_0 allows us to determine embryo distributions in the biased ensemble. Following Ref. [38], we determine $P_{\max}(n) = \text{const} \times \exp\left[\beta\phi(n)\right] P_{\max}^{\text{bias}}(n)$ and $N(n) = \text{const} \times \left\langle \exp\left[\beta\phi(n_{\max})\right] N^{\text{bias}}(n; n_{\max}) \right\rangle$ and hence determine portions of $\beta\Delta F(n)$ and $\beta\Delta G(n)$, up to constant shifts, near each n_0, where $P_{\max}^{\text{bias}}(n)$ is the probability in the biased ensemble of observing a largest embryo in the system of size n and $N^{\text{bias}}(n; n_{\max})$ is the distribution in the biased ensemble of embryo sizes given that the largest embryo is of size $n_{\max}$. As in Ref. [50] we discard histogram bins with poor statistics and simply shift the different portions of $\beta\Delta F(n)$ and $\beta\Delta G(n)$ to minimize the difference in the range of n for which the pieces overlap. We check our procedure with MBAR [39] and our results agree to within error. $\beta\Delta F(n)$ is normalized according to Eq. 2.32 and for $\beta\Delta G(n)$, we determine N_t so that $\exp\left[-\beta\Delta G(0)\right] + \sum_{i=1}^{n^*} \exp\left[-\beta\Delta G(i)\right] = N_p$. This latter condition is usually indistinguishable to within $0.1 k_{\text{B}}T$ from imposing the condition $\beta\Delta G(0) = 0$ in terms of determining $\beta\Delta G^*$. When the barrier is sufficiently low, we impose a simple "hard wall" constraint, namely, that any MC trajectory that results in $n_{\max} > n_0$ is rejected. In both biasing schemes, we generally use twenty independent starting configurations in order to obtain good averages.

3.4 Reduced Units

In this thesis, we report all quantities in reduced dimensionless units, e.g., length is rescaled by σ, energy by ϵ and time by $\sqrt{\epsilon/(m\sigma^2)}$ (where m is the mass of a particle). Scaling quantities by their natural units formed from the basic parameters of the system, k_{B}, σ, ϵ and m, shown in Table 3.1, has a few technical advantages. For one, the LJ potential is of the form $u(r) = \epsilon f(r/\sigma)$, and so using reduced units will

Property	Natural unit
number density	σ^{-3}
temperature	ϵ/k_{B}
energy	ϵ
pressure	ϵ/σ^3
time	$(m\sigma^2/\epsilon)^{1/2}$
force	ϵ/σ
surface tension	ϵ/σ^2

Table 3.1: Natural LJ units. The reduced (dimensionless) quantities are obtained by dividing by the natural unit.

remove the unnecessary multiplications with ϵ and σ. Another is that with reduced units, most quantities calculated are much closer to unity than, say, the bond energy of argon, $\epsilon = 2.73 \times 10^{-21}$ J, and so they avoid possible overflow or underflow errors within the code. However, the main reason for using reduced units is that they offer a more intuitive feel for what is going on. E.g., a per particle energy of -6 arises roughly from each particle having $6 \times 2 = 12$ energetically bonded neighbours, or a temperature of 0.5, means that the thermal energy is roughly half of the LJ bond strength.

Reduced units also enable ready comparison between systems. For example, given parameters for different noble gases $\epsilon_{\mathrm{Ar}}/k_{\mathrm{B}} = 119.8$ K and $\epsilon_{\mathrm{Kr}}/k_{\mathrm{B}} = 164.0$ K, a simulation at $T = 0.4$ translates to 47.9 K for Ar and 65.6 K for Kr.

3.5 The Simulated System

Our system consists of $N_p = 600$ particles interacting through the LJ pair potential, simulated in the canonical ensemble (constant T, volume and N_p). We use a cubic simulation box of side length $L = 30$ and employ a potential cutoff of $R_c = 14.99999$. For the range of T we consider, the system consists of a single condensed droplet

with a few particles at most detaching themselves from the droplet. The finite size and periodic boundaries ensure that these particles return to the droplet and that the droplet does not evaporate. The box size is sufficiently large to ensure that particles within the droplet do not interact unphysically with periodic images of the droplet.

We use Gromacs v4.5.5 [40] to carry out MD simulations. Temperature is maintained with the Nosé-Hoover thermostat with a time constant of 1. We use a time step of $\Delta t = 0.001$ and integrate equations of motion with the leap-frog algorithm. We equilibrate the system at $T = 0.53$, for which the droplet is well formed but clearly a liquid, and subsequently harvest 501 independent configurations by sampling every 100000 time steps. Each of these configurations serves as a starting point for a "crystallization run", for which the thermostat is set to the desired lower T. We determine $\tau(n)$ from the MFPT formalism, as in Refs. [26, 41] from these 501 crystallization trajectories for each of several T from 0.490 down to 0.370 in steps of 0.005, and from 0.350 to 0.05 in steps of 0.05. To determine $\tau(n)$, we calculate the size of the largest crystalline embryo, as described below, every 1000 time steps (integer LJ time units). As an example of calculating the first-passage time in a given run, say run number 157 of 501, suppose that at $t = 12$ an embryo of size 5 appears for the first time. Then $\tau_{157}(5) = 12$. Suppose further that the embryo shrinks but then an embryo of size 8 is recorded at time 20 (and no embryo of size 6 or 7 was recorded in the intervening times). Then we not only assign $\tau_{157}(8) = 20$, but $\tau_{157}(6) = 20$ and $\tau_{157}(7) = 20$ as well, as a way of dealing with the discrete nature of sampling. Then we average to obtain $\tau(n) = 501^{-1} \sum_{i=1}^{501} \tau_i(n)$, considering n up to the largest value sampled by all the runs.

3.6 Determining Crystal Structure

We use a procedure developed by Frenkel and co-workers [38, 42] to define crystal-like embryos within the droplet. The procedure begins with quantifying the local bond ordering for a single particle [43] via,

$$q_{6m}(i) = \frac{1}{n_b(i)} \sum_{j=1}^{n_b(i)} Y_{6m}(\hat{r}_{ij}) \tag{3.12}$$

where the sum is over the nearest neighbors $n_b(i)$ of particle i and $Y_{6m}(\hat{r}_{ij})$ is the sixth order spherical harmonic as a function of the polar and azimuthal angles specified by $\hat{r}_{ij}$, the unit pointing from particle i to neighbouring particle j. Neighbors are considered to be those within the first minimum of the radial distribution function, which is taken to be located at a distance $r = 1.363$ in this study. The *correlation* between i and a neighboring particle j is given by,

$$c_{ij} = \sum_{m=-6}^{6} \tilde{q}_{6m}(i)\tilde{q}_{6m}(j)^*, \tag{3.13}$$

where,

$$\tilde{q}_{6m}(i) = \frac{q_{6m}(i)}{\sqrt{\sum_{m=-6}^{6} \mid q_{6m} \mid^2 (i)}}, \tag{3.14}$$

and $\tilde{q}_{6m}(j)^*$ is the complex conjugate. Particles are considered to be *connected* by a crystal-like bond if $c_{ij} > 0.5$. The value of 0.5 is chosen since it is the intersection point for the probability distributions of c_{ij} obtained from 100 liquid and 100 solidified configurations at $T = 0.475$. A particle is considered to be crystal-like if it is *connected* to 80% of its neighbors (keeping in mind that particles on the surface have fewer neighbors), and two connected, crystal-like particles are considered to be part of the

same crystalline embryo.

In order to differentiate between embryos of the same size but different overall structure, we calculate a measure of the overall crystallinity of the cluster [44],

$$Q_6 = \sqrt{\frac{4\pi}{13} \sum_{m=-6}^{6} \left| \frac{\sum_{i=1}^{N_p} n_b(i)\, q_{6m}(i)}{\sum_{i=1}^{N_p} n_b(i)} \right|^2}. \tag{3.15}$$

Chapter 4

Results

4.1 Nucleation rates from MFPT

We first consider the potential energy per particle U/N_p as a function of time after the quench from $T = 0.530$ to the various target temperatures. At low to moderate supercooling, e.g., from $T = 0.485$ to $T = 0.430$ in Fig. 4.1(a), the initial rapid change in U shows the system reaching a metastable equilibrium, where the droplet is liquid. The sharp drop in U for these T after metastable equilibrium is achieved marks rapid growth of a postcritical crystalline embryo, as evidenced by the commensurate sharp increase in $n_{\max}$ in Fig. 4.1(b). At $T = 0.385$, the metastable state is less clearly seen, if at all, near $t = 60$ and the decrease in U beyond $t \approx 90$ is accompanied by an increase in $n_{\max}$. By $T = 0.200$, the system proceeds monotonically from the $T = 0.530$ state, with both U and $n_{\max}$ sliding towards the frozen state. The sharp change in U and $n_{\max}$ near $t = 400$ occurs after most of the droplet is already crystalline. While this is interesting, we do not consider it in this study.

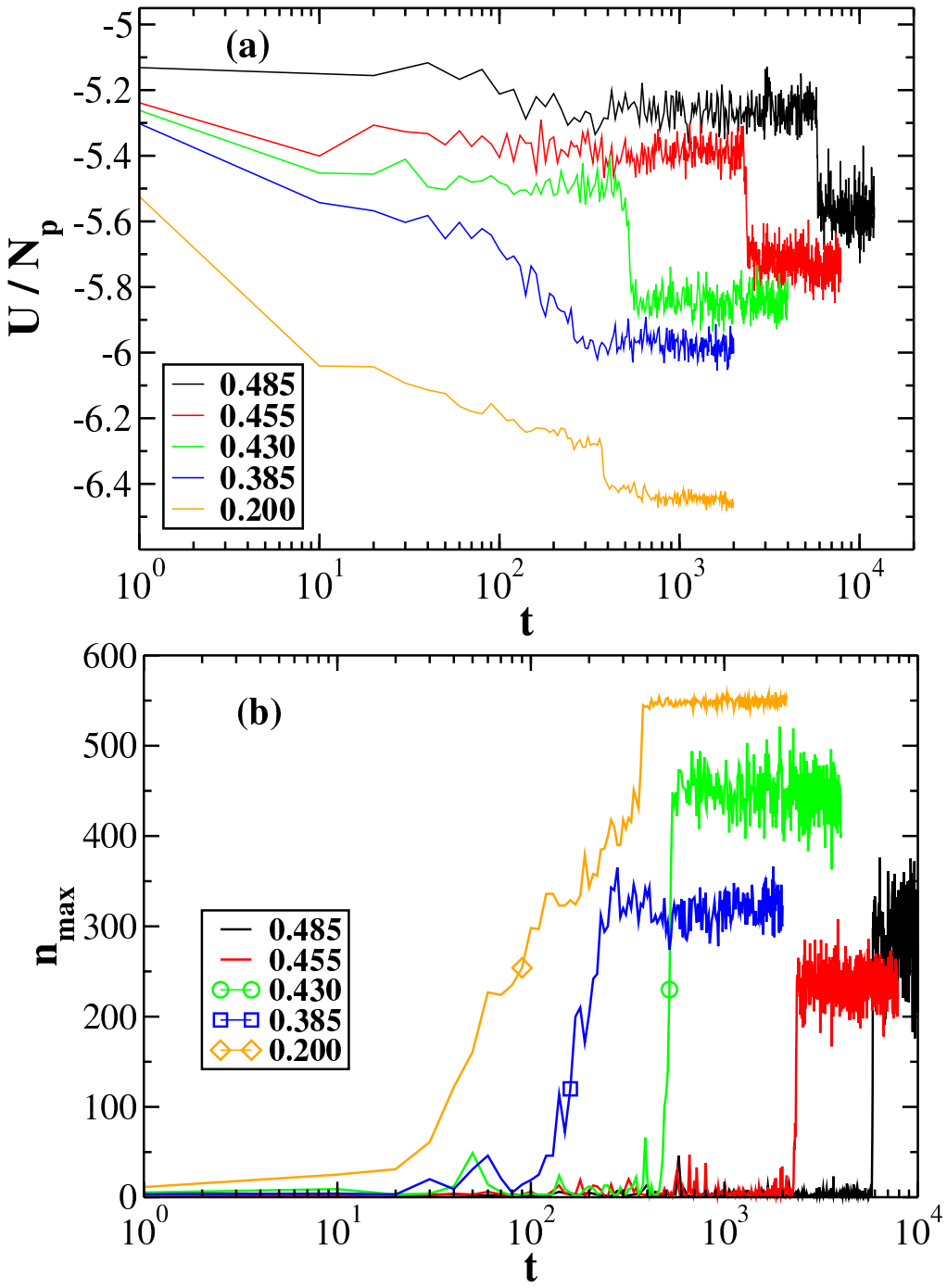

Figure 4.1: Time series of (a) potential energy U and (b) largest embryo size $n_{\max}$ showing crystallization events. At higher T, the nearly vertical behaviour of the graphs indicate very fast growth compared to the lifetime of the metastable liquid state. Legend indicates different T. At $T = 0.385$ shown, the metastable state becomes difficult to discern. At $T = 0.200$, the system progresses essentially monotonically to the frozen state.

Next we wish to quantify the rate of nucleation from $\tau(n)$. A sampling of curves from our range of T is shown in Fig. 4.2, where we have normalized the curves by $\tau(n = 250)$ since nucleation times vary widely. To actually determine the rate from fitting $\tau(n)$ with Eq. 2.43 is well defined only at fairly shallow superercooling, where $\tau(n)$ exhibits the sigmoidal shape characteristic of relatively high nucleation barriers. At these shallow supercoolings, e.g., $T = 0.485$, the initial horizontal plateau of $\tau(n)$ corresponds to the relative ease with which the small crystalline embryos appear in the droplet. The inflection corresponds to the low probability with which embryos of near-critical size appear, and also to the lack of a thermodynamic driving force for critical embryos to change size. The plateau at large times corresponds to fast growth of embryos once they have "gone over the barrier".

At deeper supercooling, the initial horizontal plateau in $\tau(n)$ shortens as n^* decreases, but there is still a relatively fast change in slope in $\tau(n)$ at larger n as the embryo leaves the critical region and experiences more rapid growth. When barriers become very small, the crystallization time is dominated by growth, which is now relatively slow compared to the rate at which critical nuclei are formed, and $\tau(n)$ becomes linear.

We see that from $\tau(n)$ alone, it is not straightforward to determine the rate unambiguously except at shallow supercooling. Once we define $J_{250} \equiv 1/\tau(250)$ and $J_{\mathrm{MFPT}} \equiv 1/\tau_J$, where τ_J is determined from fitting to Eq. 2.43 at $T = 0.415$ and above [where $\tau(n)$ is still fairly well approximated by the sigmoidal shape of Eq. 2.43], we see from Fig. 4.3(a) that these two estimates for the rate agree very well. The two rates agree since in this range of T, growth is quite fast and the upper plateau in $\tau(n)$ is quite flat. Choosing a fixed value such as $n = 250$ to determine the rate necessarily includes a portion of the growth phase of crystallization, and therefore J_{250} provides a lower bound on the rate. To provide a less biased estimate of the rate

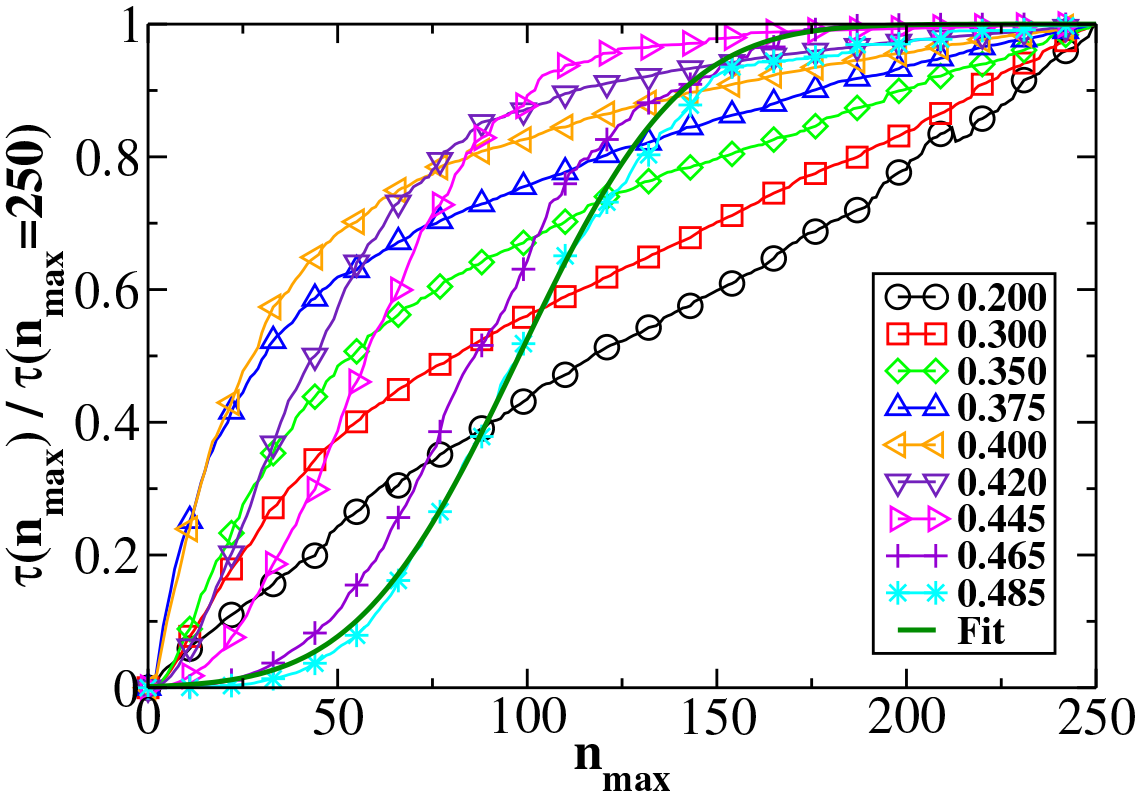

Figure 4.2: Mean first-passage time $\tau(n)$ for the appearance of an embryo of size n for a range of T indicated by the legend. For ease of comparison, curves are normalized by $\tau(250)$, which we take to be a measure of the rate across T. For $T = 0.485$, we show a fit according to Eq. 2.43. This characteristic sigmoidal shape is progressively lost with increased supercooling as the early time plateau shortens. Beyond $T = 0.420$, the curve begins to flatten as growth begins to dominate the crystallization process until the curve is roughly linear by $T = 0.200$.

from MD simulations, we define $J_b \equiv 1/\tau(b)$, where b is the upper value of $n_{\max}$ used to normalize the steady-state probability $P^{\rm st}_{\rm max}(n)$ in Eq. 2.52. We discuss how we choose b below, but roughly speaking $b \approx 2n^*$. Another estimate of the rate we use is $J_{2n^*} \equiv [2\tau(n^*)]^{-1}$, which stems from the definition that at the critical state, the system will either continue to grow or shrink with probability 1/2, but the drawback is that MFPT barrier reconstruction allows us to determine n^* only to $T = 0.390$. We plot J_b and J_{2n^*} alongside J_{250} and $J_{\rm MFPT}$. They all agree at higher T (shallow undercooling) but begin to diverge when growth starts being important around $T = 0.400$. J_{250} and

J_b both exhibit a maximum.

In the next section, we determine the extent to which simple CNT can quantitatively account for the T dependence of the rate, or conversely, to what extent we can reliably extract relevant physical quantities from the rate.

4.2 T dependence of the rate and CNT

As discussed in Section 2.1, the simplest model for $J(T)$ assumes an Arrhenius dependence of the attachment rate on T, a constant surface tension and a constant difference in enthalpy between the solid and liquid phases. The resulting model is given in Eq. 2.23, which we use to fit J_{250} and J_{MFPT}. We use data from all $T \geq 0.200$ to determine the fit parameters, except for T=0.490, which, as it turns out, is above melting. Although we measure a rate of nucleation at $T = 0.490$, since this small system escapes form the stable liquid into the metastable solid, the rate is higher than for $T = 0.485$, and so we neglect it. We note that J_{MFPT} is determined for $T \geq 0.415$, and so fitting it to Eq. 2.23 is essentially fitting the nucleation rate close to melting, the regime for which Eq. 2.23 is formulated.

Fitting J directly using Eq. 2.23, to which we refer as *linear fit*, because of the orders-of-magnitude difference in the rates at different T highly biases the fit to the points where J is largest. To check this bias, we also fit by first taking logarithms of both sides of Eq. 2.23, which we call *log fit*. The resulting fit parameters are listed in Table 4.1, and the resulting curves for the linear fits of J_{250} and J_{MFPT} are plotted in Fig. 4.3(a). We see a rather drastic change in the fit parameters when comparing shallow supercooling and the broader T range. Using linear or log fits also produces different parameters even though the resulting curves are similar (not plotted).

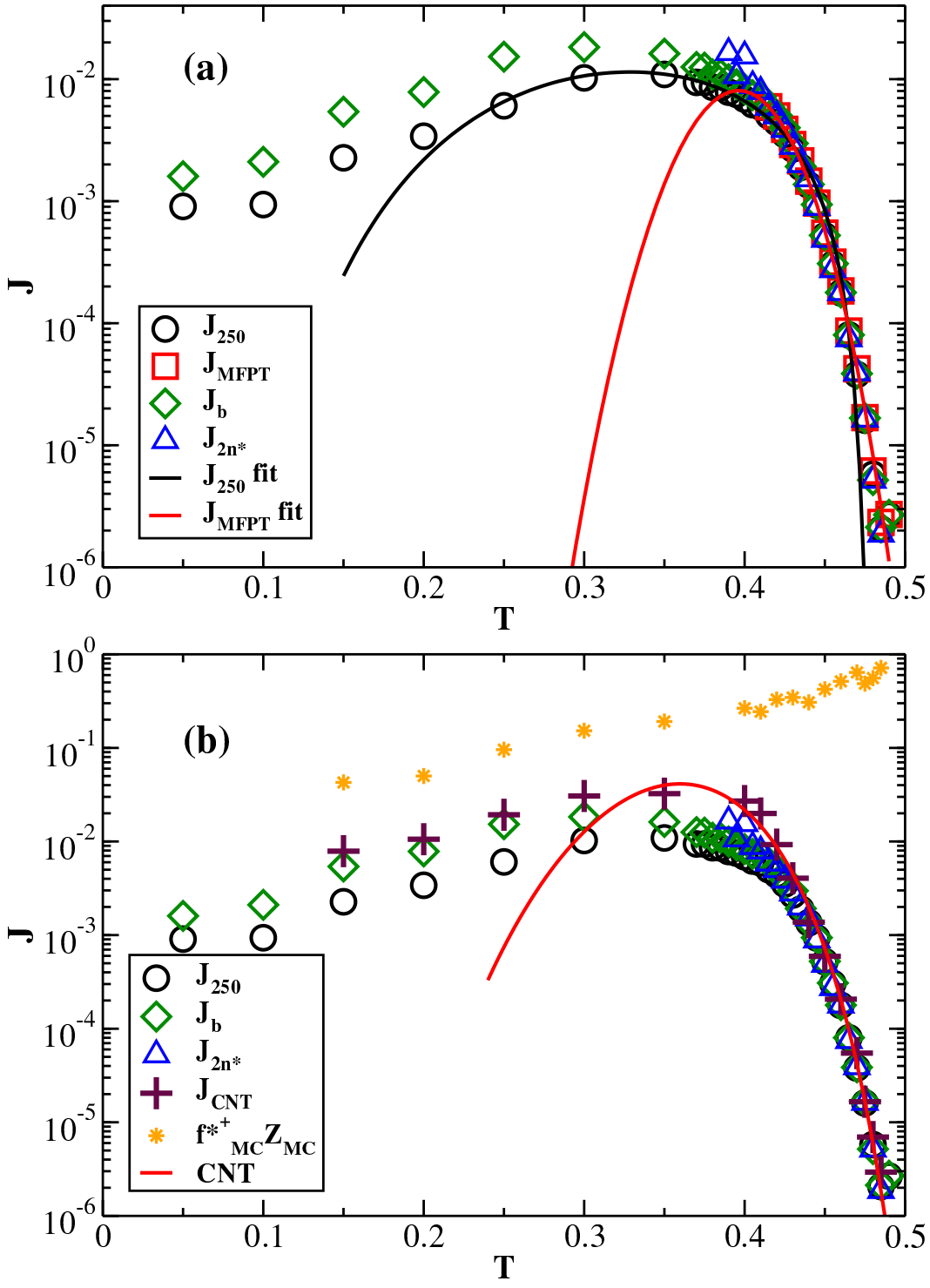

Figure 4.3: Nucleation rate as a function of T. Panel (a) shows four estimates as described in the text of J based on $\tau(n)$, which all agree at higher T. Curves are fits according to Eq. 2.23. Panel (b) shows a comparison with rate predicted by Eq. 2.20 (brown plus signs) and the result of using Eq. 2.23 (curve) with independently determined parameters except for $\gamma = 0.131$, which is chosen to give a good fit.

	J_{250} linear fit	J_{250} log fit	J_{MFPT} linear fit	J_{MFPT} log fit
λ	35	87	7.1×10^{34}	2.8×10^{21}
T_m	0.49	0.54	0.77	0.67
B	8.8×10^{-4}	1.5×10^{-2}	2.1	0.54
C	1.6	1.7	18	14

Table 4.1: The fitting parameters obtained for J_{250}, and J_{MFPT} with Eq. 2.23. The terms *linear fit* and *log fit* refer to whether the fitting is done directly using Eq. 2.23 or done after taking logarithms of both sides. The fits for J_{250} span T from 0.200 to 0.485, while the fits for J_{MFPT} span T from 0.415 to 0.485.

Choosing data from J_{250} in the same temperature range over which J_{MFPT} is calculated produces similar fit parameters to those listed for J_{MFPT}. Using fewer points from the lower T range does not significantly affect the fits for J_{MFPT}. Attempts to use an equation similar to Eq. 2.23, but developed for growth-controlled crystallization [34], does not reproduce the weakly exponential decay of J_{250} at the lowest T, even if the higher T data are omitted from fitting, and produces curves similar to those obtained with Eq. 2.23. While Eq. 2.23 is able, for our system, to describe the T dependence of the rate only for shallow supercooling, it does seem to provide an estimate of the maximum rate based on relatively high T data where rates are low.

We see that the rate predicted by Eq. 2.23, while being very sensitive to parameters such as γ, ΔH and the order of magnitude of f_0, is not particularly suited to determining these quantities, as significant changes in one parameter can be compensated by a significant change in another in order to produce similar curves. Nonetheless, we now proceed to determine reasonable values of the parameters in Eq. 2.23 by independent means by examining T_m, ΔH, A, f_0 and γ.

4.2.1 The melting temperature

There are two melting temperatures to speak of. According to Eqs. 2.11 and 2.20, the barrier to nucleation, $\Delta G(n^*)$, becomes infinite and the rate is zero when $\Delta\mu = 0$, which simultaneously defines the melting temperature in the thermodynamic limit. This T_m, then, represents the T at which the rate is zero and below which the chemical potential of the crystal is lower than that of the liquid. For our finite-sized cluster, the presence of a surface complicates matters, and the melting temperature should be defined as the temperature at which the droplet has equal probability of being either solid or liquid.

The values of T_m obtained from fits of $J_{\mathrm{MFPT}}(T)$ are in the range of 0.67 to 0.77. The pressure of our system, evaluated from the virial as for a bulk system, is less than 10^{-4}, effectively zero. Even if the interior of the droplet is subject to a Laplace pressure of $2\gamma/R \sim 2(1)/6 < 0.5$, then the range of T_m from bulk values is, for $p = 0$, 0.68 [45] or 0.618 [46] to 0.74 ($p = 0.5$) [45]. Thus, using Eq. 2.23 to fit $J(T)$ provides a reasonable estimate of the fcc-liquid melting temperature in bulk.

As for the coexistence temperature between solid and liquid cluster, we note that the system at $T = 0.490$ is predominantly in the liquid state but makes short excursions to being largely solid (a surface melted state). This flipping between states is apparent in any of the 501 potential energy time series we have collected for this state point, one of which is plotted in Fig. 4.4. From the equilibrated time series we construct a probability distribution for the potential energy $P(U)$, which in turn allows us to calculate the heat capacity, via,

$$C_V = \frac{\langle U^2\rangle - \langle U\rangle^2}{k_{\mathrm{B}}T^2} + \frac{3}{2}N_p k_{\mathrm{B}}T, \tag{4.1}$$

where $\langle . \rangle$ denote an average. Since $P(U) \propto \Omega(U)\exp\left[-\beta U\right]$, and the density of states

$\Omega(U)$ is independent of T, one can in a straightforward manner estimate $P(U)$ at other T, and hence $C_V(T)$.

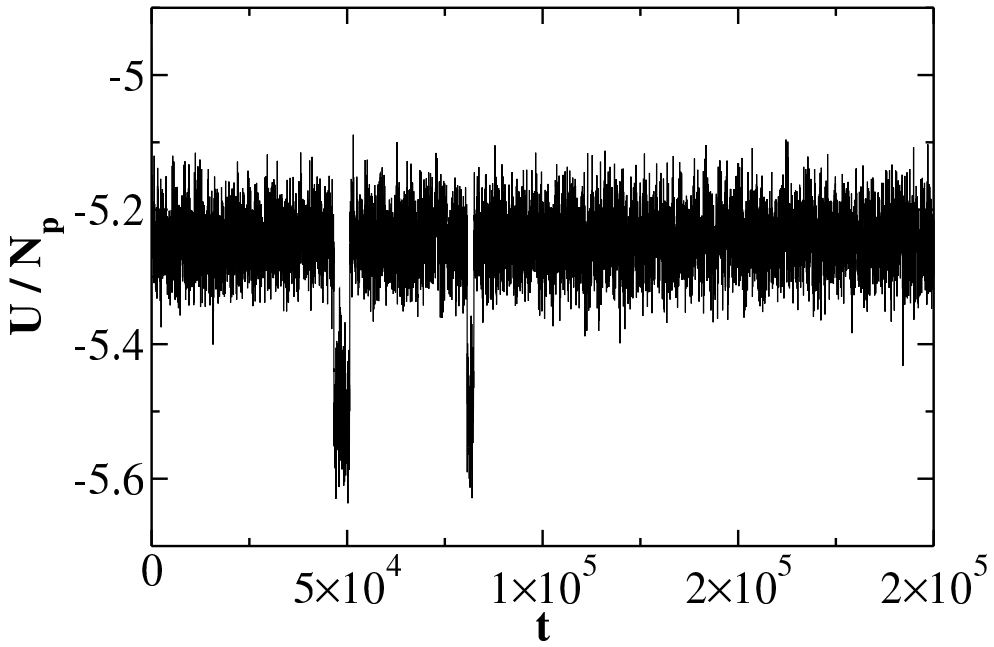

Figure 4.4: Potential energy times series for the droplet at $T = 0.490$. The system makes infrequent, short-lived flips into the solid state. This spontaneous sampling of both energy states allows us to use reweighting techniques to determine the heat capacity for lower T.

The histogram for $T = 0.490$ is shown in Fig. 4.5(a), showing a distinctly bimodal character, while the resulting $C_V(T)$ is given in panel (b). Along with the extrapolated $C_V(T)$ curve, we plot with a red circle $C_V(T = 0.470)$, determined solely from energy fluctuations in the crystallized state at that T. There are several possible reasons for the discrepancy, such as not taking care to correct for the bias in the $T = 0.490$ histogram arising from always starting in the liquid state and from not sampling sufficiently at $T = 0.490$ the crystalline states present at $T = 0.470$. However, our aim is to merely estimate the solid-liquid coexistence temperature for our cluster $T_m^c = 0.4815$ as the location of the C_V peak, which occurs when $P(U)$ is widest, i.e., sampling liquid and solid equally. Clearly, T_m^c is not the intended melting temperature

in Eq. 2.23.

4.2.2 The enthalpy difference

Another quantity entering into the calculation of the coefficients λ and B of Eq. 2.23 is $\Delta H = U_L - U_S + P(V_L - V_S)$, the enthalpy difference between liquid and solid. Given that our system is at a very small pressure, that the densities of liquid and crystal are comparable and that there is a sizeable potential energy difference between liquid and crystal, we approximate $\Delta H \approx U_L - U_S \equiv N_p \Delta u$, where Δu is the per particle potential energy difference between the liquid and crystal. The scenario is complicated here once again by the fact that when our droplet solidifies, it does so incompletely and remains partially liquid. Calling ΔU the difference in potential energy between the liquid and (partially) solidified droplet, and α the fraction of particles in the solidified droplet identified as solid-like, then we can estimate the enthalpy difference as,

$$\frac{\Delta H}{N_p} = \Delta u = \frac{1}{\alpha}\frac{\Delta U}{N_p}. \tag{4.2}$$

In Fig. 4.6(a) we plot α as a function of T, and see that the fraction of solid-like particles in the frozen state, at least according to our order parameters, increases roughly linearly with decreasing T. In panel (b) of the same figure, we plot both $\Delta U/N_p$ and the resulting Δu. Somewhat surprisingly, we see that the assumption of constant enthalpy difference between liquid and crystal used in deriving Eq. 2.23 is vindicated, and its value is approximately $\Delta H/N_p = \Delta u = 0.58$.

4.2.3 Embryo shape

As noted above, we assume that the surface area of a crystalline embryo within the droplet has surface area $S = An^{2/3}$. If we assume spherical embryos and a volume per particle to be that of an fcc particle, $v_{\rm fcc} = 1.04$ [45], we obtain $A = 4.96$. To obtain a better estimate of the shape factor, we model the embryo as an ellipsoid [23]. To do this, we first compute the moment of inertia tensor for all particles in the largest embryo in the system,

$$I_{mn} = \sum_{i=1}^{n_{\rm max}} \left[r_i^2 \delta_{mn} - r_{i,m} r_{i,n} \right], \tag{4.3}$$

where r_i is the position of particle i with respect to the centre of mass of the embryo, $r_{i,m}$ is the m^{th} component (x, y or z) and δ_{mn} is the Kronecker delta function. The principal moments (eigenvalues) I_{xx}, I_{yy} and I_{zz} of I_{mn}, give us the principal axes lengths a, b and c (radii) of the ellipse from relations $5I_{zz} = n_{\rm max}(a^2 + b^2)$, $5I_{xx} = n_{\rm max}(b^2 + c^2)$ and $5I_{yy} = n_{\rm max}(a^2 + c^2)$. The area is then given by,

$$S = 2\pi c^2 + \frac{2\pi ab}{\sin\phi} \left(E(\phi, k) \sin^2\phi + F(\phi, k) \cos^2\phi \right), \tag{4.4}$$

where $E(\phi, k)$ and $F(\phi, k)$ are elliptic functions of the first and second kind, respectively, $\cos\phi = c/a$, $k^2 = \frac{a^2\left(b^2 - c^2\right)}{b^2(a^2 - c^2)}$ and where $a \geq b \geq c$. We plot $A = Sn^{-2/3}$ as a function of n in Fig. 4.7 for both critical embryos from all T, and all largest embryos from MD trajectories for $T = 0.485$. We see that, roughly speaking, the critical embryos from different T follow the same behaviour as embryos (pre-critical, critical and post-critical) at $T = 0.485$. For large embryos (shown in the lower inset) A tends to the spherical value of ~ 5, as is expected. For our range of T of interest (0.415 to 0.485), we see that the embryos become less spherical with decreasing size, and that the values of A range from about 6.7 to 8.5 (corresponding to $50 < n < 100$). The upper inset shows that the dependence of S on $n^{2/3}$ possesses only a slowly varying

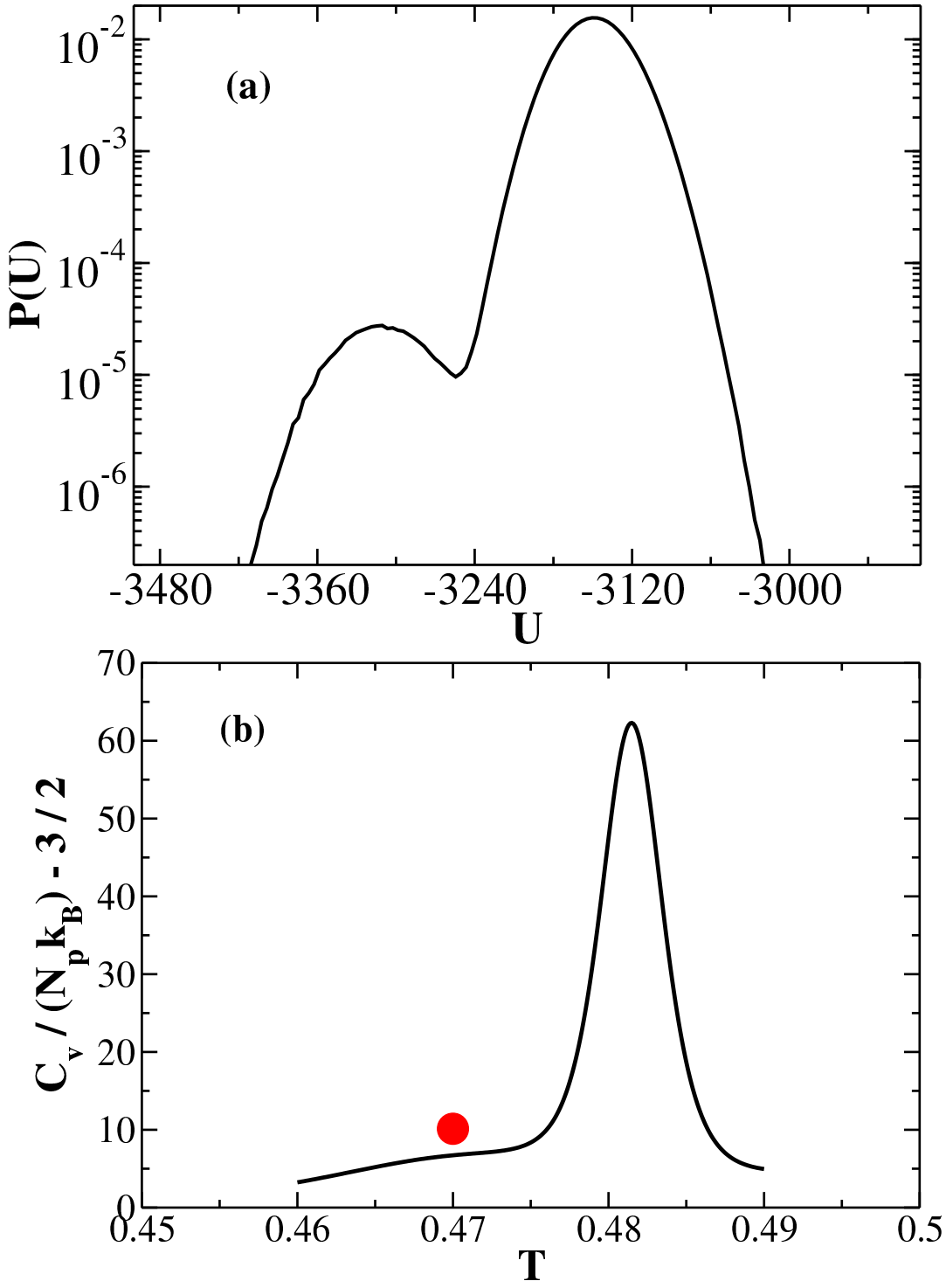

Figure 4.5: Determination of C_V. Panel (a) shows the probability distribution for the potential energy at $T = 0.490$. The distribution shows two peaks, one for the stable liquid (high U) and one for the metastable solid (low U). Panel (b) shows $C_V(T)$ as determined from histogram reweighting (curve), with a peak at $T = 0.4815$. The red circle is the value of C_V at $T = 0.470$ determined from solidified cluster states.

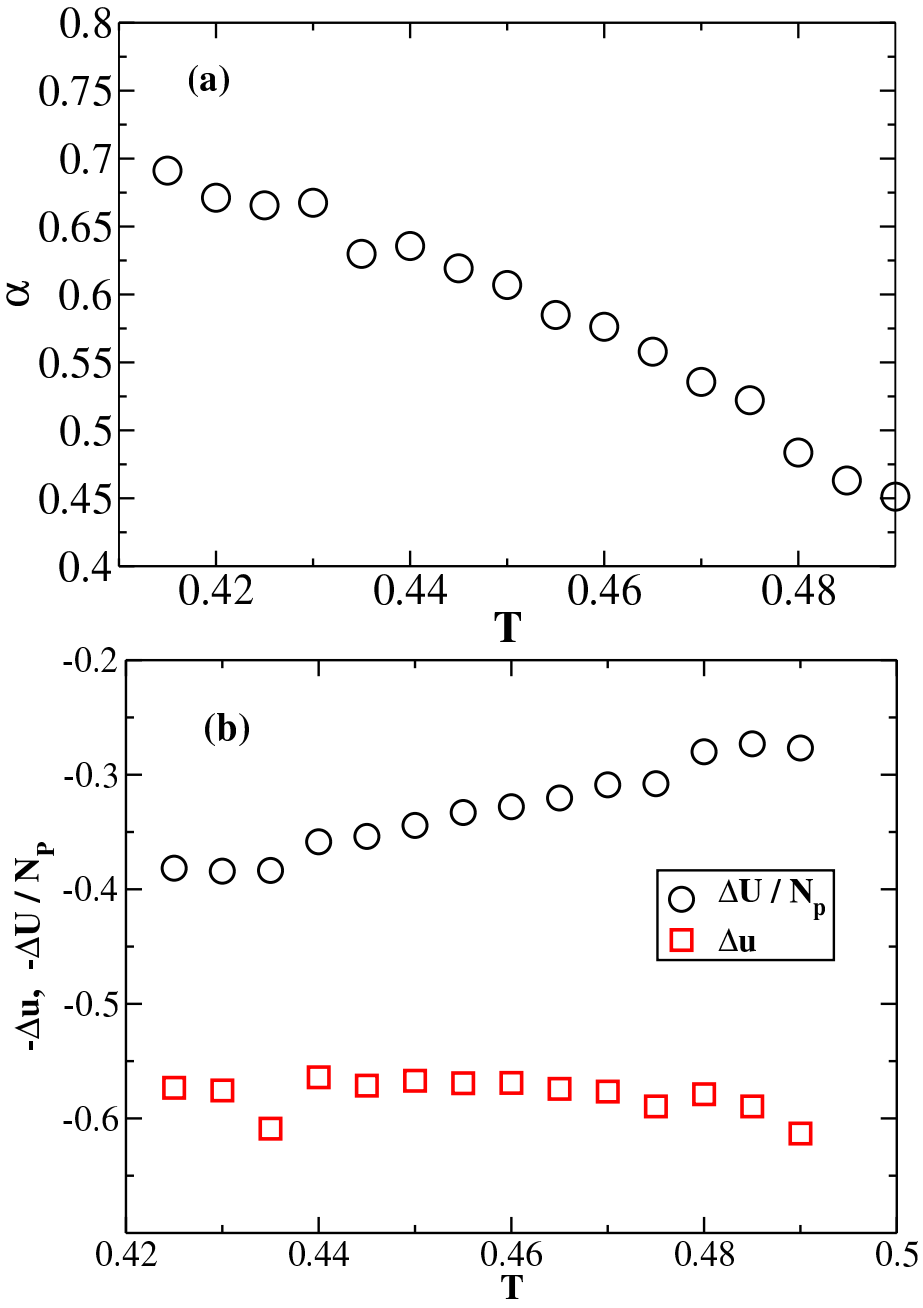

Figure 4.6: Determining $\Delta H/N_p$. Panel (a) shows the fraction α of solid-like particles in a solidified cluster as a function of T. Panel (b) shows the raw estimate $\Delta H = \Delta U$, the system potential energy difference before and after crystallization occurs, as well as a more refined estimate $N_p \Delta u = \Delta H$ that takes into account α in determining energy differences between solid and liquid particles. Δu is approximately constant with T.

departure from linearity.

In mean-field theories of nucleation that predict a spinodal, as the spinodal is reached, the critical embryo becomes ramified, large and anisotropic. To quantify the degree to which critical embryos are anisotropic, we plot the ratio to the largest semi-axis to the smallest semi-axis in Fig. 4.8(a), and see that indeed this ratio attains a value near 4, indicating rather high anisotropy.

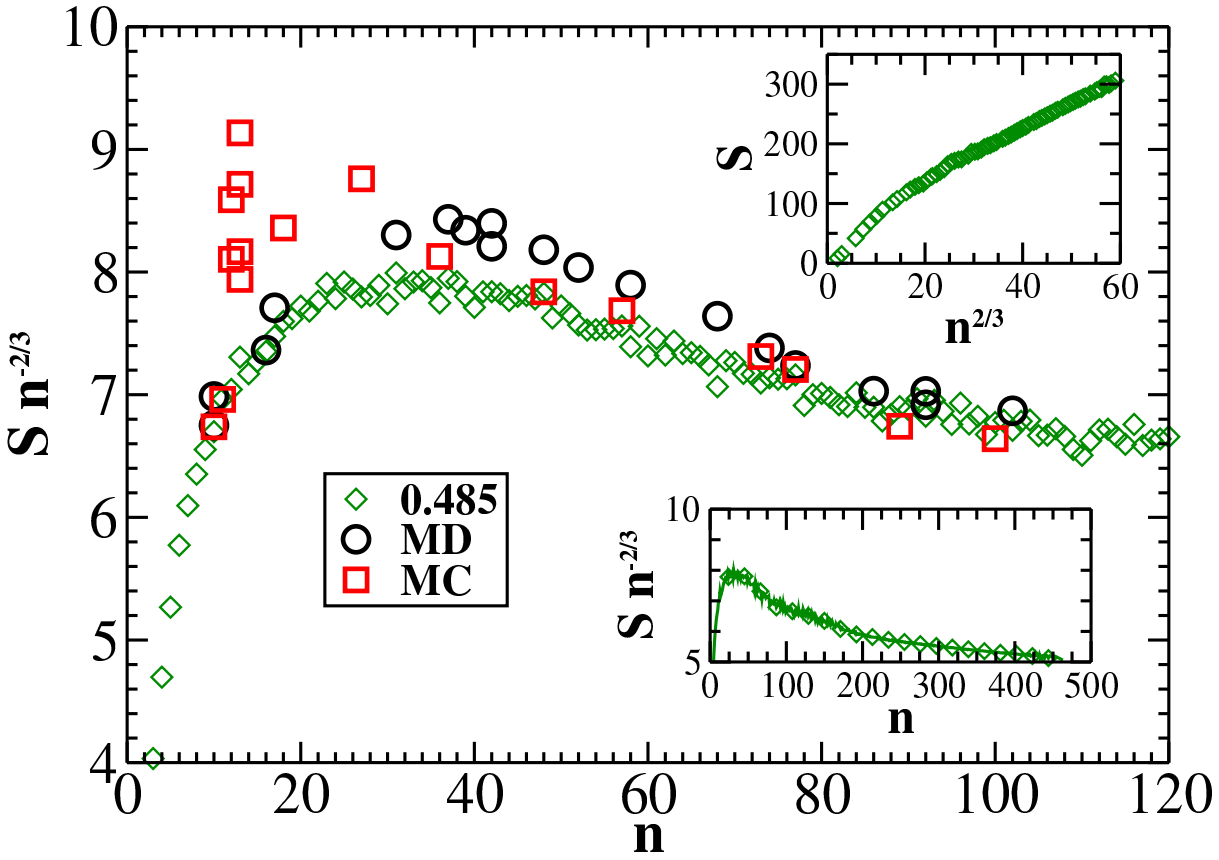

Figure 4.7: Estimating the shape factor $A = Sn^{-2/3}$ as a function of embryo size, where embryo area S is that of an ellipse with equivalent moments of inertia as an embryo. Shown are data for critical clusters from MD (circles) and MC (squares), as well as from all clusters from MD simulations at $T = 0.485$. In the T range where we expect Eq. 2.23 to be valid, corresponding to $50 < n < 100$, A ranges from about 6.7 to 8.5. Insets show S as a function of $n^{2/3}$ (upper) and that A approaches a spherical value of 5 for large n (lower).

To test this further, we calculate the relative shape anisotropy κ^2,

$$\kappa^2 = \frac{3}{2}\frac{\lambda_x^4+\lambda_y^4+\lambda_z^4}{\left(\lambda_x^2+\lambda_y^2+\lambda_z^2\right)^2} - \frac{1}{2}, \tag{4.5}$$

where λ_m^2 is an eigenvalue of the gyration tensor,

$$S_{mn} = \frac{1}{2n_{\max}^2}\sum_{i=1}^{n_{\max}}\sum_{j=1}^{n_{\max}}\left(r_{i,m}-r_{j,m}\right)\left(r_{i,n}-r_{j,n}\right). \tag{4.6}$$

We plot κ^2 in Fig. 4.8(b) as a function of embryo size for critical embryos across our T range from both MD and MC simulations, as well as for largest embryos taken from MD configurations at $T = 0.485$. For a spherical object, $\kappa^2 = 0$, while for linear objects, $\kappa^2 = 1$. The plot confirms that smaller critical embryos are more anisotropic, but what is interesting is that the size dependence of the anisotropy is the same as that for embryos taken from $T = 0.485$.

The similarity between critical embryos of different sizes (taken from different T) and embryos taken from near coexistence ($T = 0.485$), in terms of area and anisotropy, allows for a T independent modelling of A. This also provides some indication against the notion of a mean-field spinodal, that would give rise to structural changes to embryos with deep supercooling, i.e., we see small critical embryos at low T with similar structural properties to similarly-sized embryos from high T.

4.2.4 Attachment rate

To estimate f_0, which is an essential prefactor in λ in Eqs. 2.23 and 2.25 via Eq. 2.22, we take two independent approaches. The first uses the MFPT approach, for which

the attachment rate for embryos of all sizes is obtained through the relation [27],

$$f^+(n) = B_F(n)/\frac{\partial \tau(n)}{\partial n}, \tag{4.7}$$

where $B_F(n)$ is defined in Eq. 2.52 and relies on $\tau(n)$ and $P^{\rm st}_{\rm max}(n)$ for its calculation. The derivative in the above equation unavoidably introduces noise when determining $f^+(n)$.

The first step in finding $f^+(n)$ is to obtain $P^{\rm st}_{\rm max}(n)$, and we do so by accumulating a histogram during the MD simulations that we use to obtain $\tau(n)$, using only data up to the time in each run that $n_{\rm max}$ first surpasses the upper limit b, i.e., we stop collecting data when $n_{\rm max}$ leaves the region $[0, b]$. Thus, $P^{\rm st}_{\rm max}(n)$ is a function of b, but generally, once b is large enough, the system should only grow after $n_{\rm max}$ reaches b and hence $P^{\rm st}_{\rm max}(n)$ should not change shape with increasing b. A complication in our system is that kinetically trapped intermediate or thermodynamically stable crystalline structures are present whose size is not significantly larger than n^*, resulting in a local maximum in $P^{\rm st}_{\rm max}(n)$ for $n > n^*$. This means that there will be a strong dependence of $P^{\rm st}_{\rm max}(n)$ on b, as we show in Fig. 4.9. In principle, if the MD simulations are run long enough and the system can flip back and forth between solid and liquid, the steady-state distribution becomes the equilibrium distribution. However, we only achieve this equilibration at $T = 0.490$.

Our approach to deal with this challenge is to choose a value of b where the nearly linear regime predicted by Eq. 2.60 is largest in extent. For the cases plotted in Fig. 4.9, this corresponds to a value of $b = 190$. We validate this choice below by comparing the free energy barrier reconstructed from the MFPT formalism, which is also sensitive to b, with MC simulations.

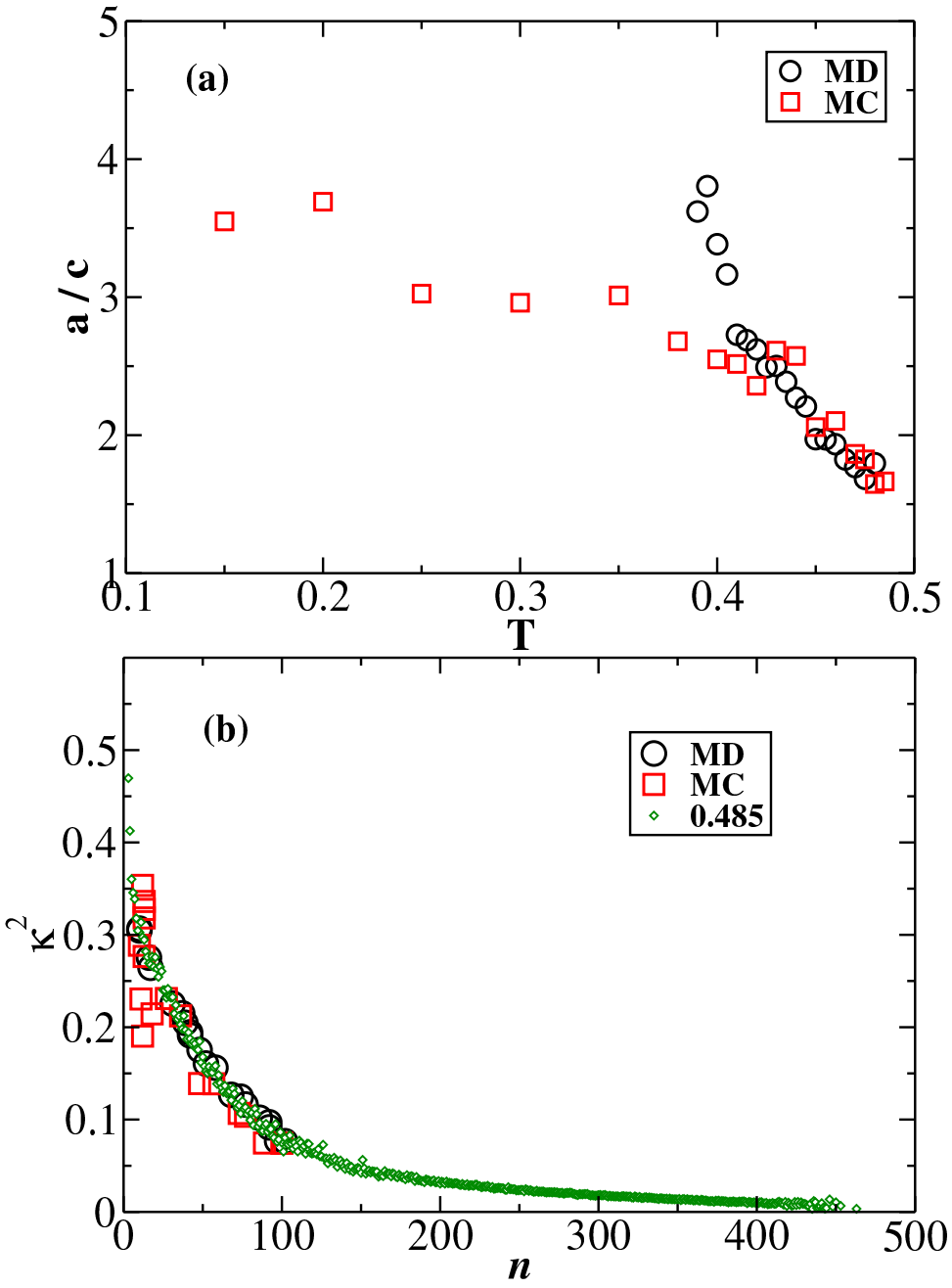

Figure 4.8: Quantifying embryo anisotropy. (a) The ratio between the maximum and the minimum semi-minor axes for critical embryos as a function of T. Ratios for both MD (circles) and MC (squares) are above 1, indicating that the embryos are not perfect spheres, and increase as T decreases. (b) Relative shape anisotropy, for which $\kappa^2 = 0$ for spheres 1 for linear objects. Here, we see that although small critical embryos become quite anisotropic, the anisotropy follows the same behavior as for embryos taken from at MD data $T = 0.485$ (small green diamonds).

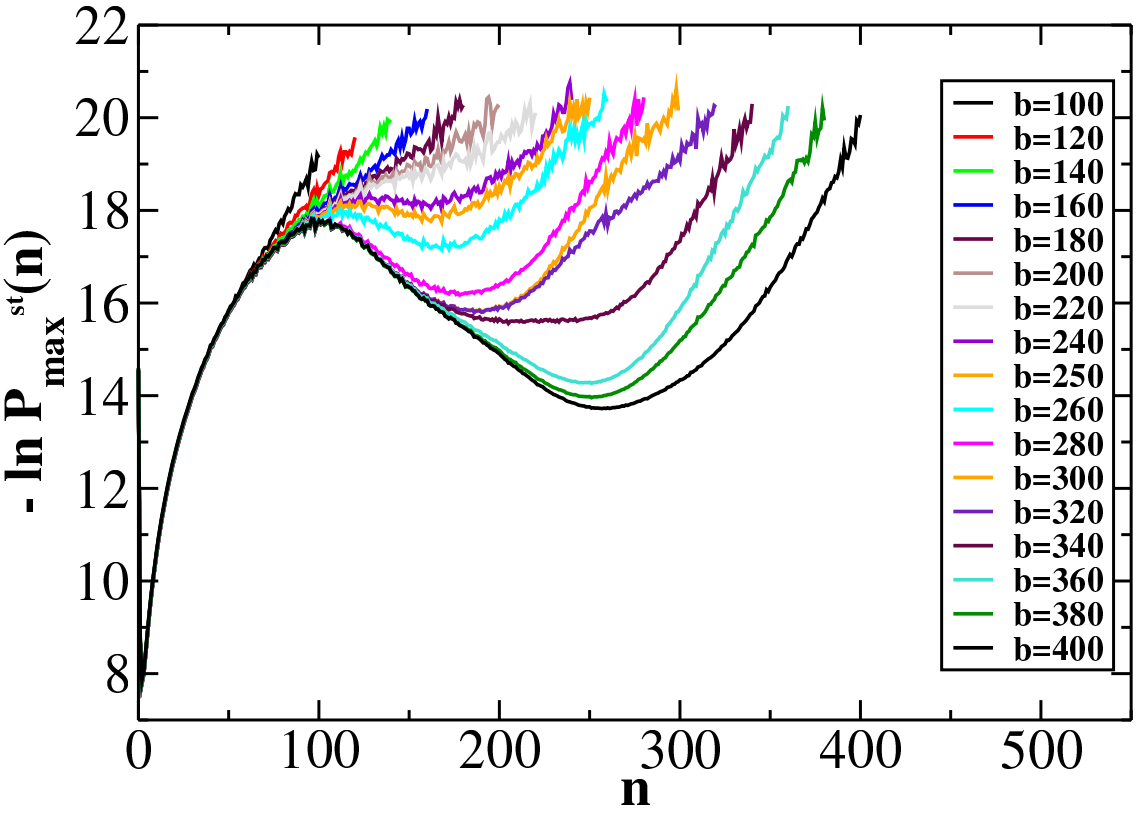

Figure 4.9: Steady-state distributions $P^{st}_{\max}(n)$ obtained during MD simulations at $T = 0.485$ for different values of absorbing parameter b, showing a strong dependence on b. The appearance of a second minimum in the curves indicates a high tendency for the embryos shrink at sizes significantly larger than n^*.

Having chosen a way to pick b, we calculate $f^+(n)$ through Eq. 4.7 and show the result in Fig. 4.10(a). In these calculations, since n is discrete, we replace the integrals with sums and use the centred difference scheme to calculate the derivative of $\tau(n)$. The noise in $f^+(n)$ is readily apparent and so to calculate $f^+(n^*)$, we average $f^+(n)$ over 21 points, i.e., including 10 points on either side of n^*. We find $n^* = 97$ for $T = 0.485$ as determined from either Eq. 2.43 or from barrier reconstruction, which we present below. Also shown is the result based on MC simulations, which we describe next. The good agreement between methods is encouraging, but only occurs at $T = 0.485$ and $T = 0.480$ when both MC and MD predict the same critical embryo size (we also discuss this below).

Another method we use for determining the attachment rate, and now describe, follows Refs. [38, 42]. This method makes use of the fact that the change in size of a critical embryo follows a simple diffusive process since the free energy landscape is locally flat at the top of the free energy barrier. One defines the mean of the squared deviation from the critical size as a function of time,

$$\left\langle \Delta n^2(t) \right\rangle = \left\langle [n_{\max}(t) - n_{\max}(0)]^2 \right\rangle , \tag{4.8}$$

where $n_{\max}(0) = n^*$. After a very short time, $\langle \Delta n^2(t) \rangle$ enters a diffusive regime [47], i.e., it becomes linear in time, and one obtains in this regime,

$$f^+_{\text{crit}} = \frac{1}{2} \text{slope of } \left\langle \Delta n^2(t) \right\rangle . \tag{4.9}$$

The usual process is to select a few system configurations containing an embryo of size n^* from MC simulations and to use those as starting points for MD simulations. One then selects trajectories that diffuse near n^* and averages over these trajectories, i.e., one rejects runs for which the embryo slips off the top of the barrier and shows rapid growth or decay. For low barriers, attachment of clusters of particles to the critical embryo (or break-up of a tenously-linked embryo), rather than single particle events, may contribute to rapid growth or decay. We follow the same procedure, employing from 50 (at low T) to 300 (at high T) MC configurations. The criteria for choosing what constitutes diffusive motion is unclear, for even an embryo that appears to grow first undergoes a diffusive process, and this diffusive behaviour should be included in the averaging.

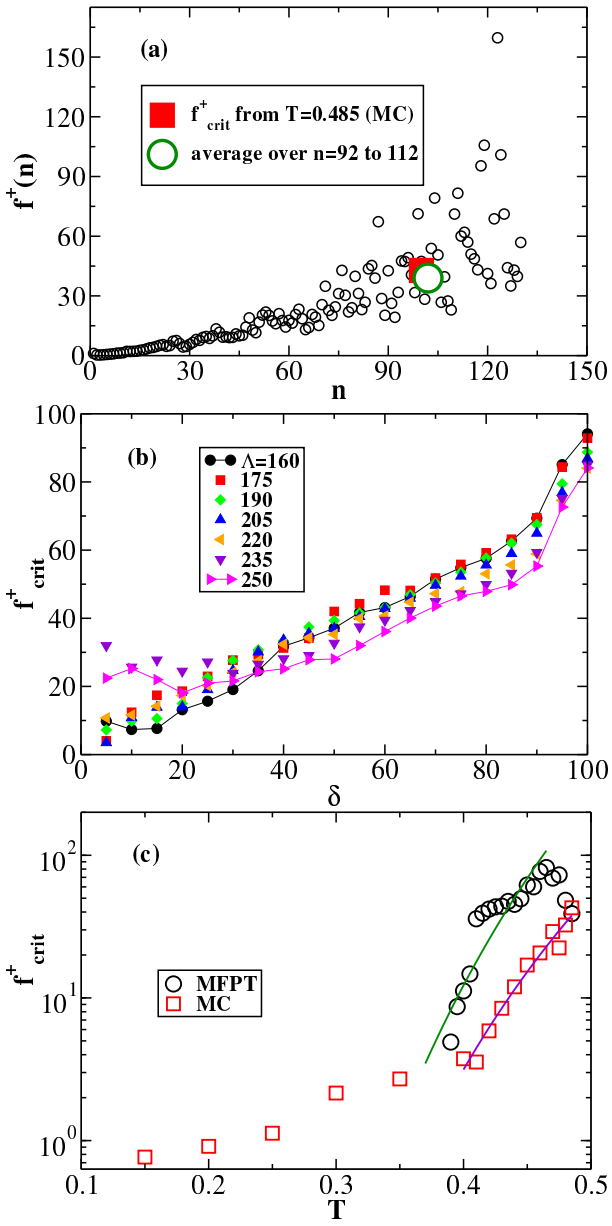

Figure 4.10: Determination of the attachment rate to the critical cluster. (a) MFPT result for $f^+(n)$ from Eq. 4.7 for $T = 0.485$. To determine $f^+(n_F^*)$, an average is taken over $n = n_F^* \pm 10$ (large circle), while the MC result (square) is plotted for comparison. (b) The effect of Λ and δ on $f^+_{\rm crit}$ for $T = 0.485$. Short MD trajectories used to determine $f^+_{\rm crit}$ contribute to the average in Eq. 4.8 if $|n_{max}(\Lambda) - n_{max}(0)| < \delta$. Values of Λ for the different curves are given in the legend. To obtain $f^+_{\rm crit}$, we average over all Λ and $30 \leq \delta \leq 90$. (c) $f^+_{\rm crit}$ (MC - square) and $f^+(n_F^*)$ (MFPT - circles) as functions of T. Curves are Arrhenius fits $\ln f^+(n_F^*) = 16.94 - 5.73\frac{1}{T}$ for MFPT, and $\ln f^+_{crit} = 15.35 - 5.68\frac{1}{T}$ over $0.400 \leq T \leq 0.485$ for MC.

To systematically explore this, we define two parameters, δ and Λ, and perform averaging in Eq. 4.8 for trajectories that satisfy $|n_{max}(\Lambda) - n_{max}(0)| < \delta$. In principle, δ should be of the size over which the free energy barrier is flat. Λ governs the length of time over which a trajectory ends up back within δ of n^*. A small Λ eliminates embryos that exhibit large changes in short times, while a large Λ allows embryos that grow or shrink to return to the critical region. Ideally, there should be a range of δ and Λ over which $f^+_{\rm crit}$ is invariant. We note that we employ averaging over time origins, i.e., if an embryo returns to n^* after a time of 4, we treat that time as the beginning of an independent trajectory.

The results for $f^+_{\rm crit}$ as a function of δ for different Λ values are shown in Fig. 4.10(b). We see that for $\delta < 30$, there is a large spread in $f^+_{\rm crit}$ over different Λ. For $\delta > 90$, there is a rapid increase in $f^+_{\rm crit}$. For δ in between, we see no obvious way to choose an optimal $f^+_{\rm crit}$, and so we average over the range $30 \leq \delta \leq 90$ over all Λ to obtain $f^+_{\rm crit} = 43$ with a standard deviation of 13.

We note that in both methods, we always track the size of the largest embryo, and therefore do not differentiate between cases where the largest embryo at one time is the same embryo at the next, i.e., we assume $f^+_{\rm crit} = f^+(n^*)$. Neither do we analyze for multiple particle attachments.

Repeating both the MFPT-based and MC-based methods, we obtain $f^+_{\rm crit}$ across our T range, which we plot in Fig. 4.10(c). The figure also shows fits of $f^+_{\rm crit}$ to the Arrhenius behaviour in Eq. 2.22 over $0.390 \leq T \leq 0.465$ for MFPT (squares) and $0.400 \leq T \leq 0.485$ for MC (triangles). The fit parameters from MD are $C = 5.7 \pm 0.5$ and $f_0 = \exp(16.9 \pm 1.6) = 2.3 \times 10^7$ (4.6×10^6 to 1.1×10^8), and from MC are $C = 5.7 \pm 0.3$ and $f_0 = \exp(15.4 \pm 0.7) = 4.7 \times 10^6$ (2.3×10^6 to 9.4×10^6). Both methods agree on the value of C. The discrepancy in f_0 likely stems from the larger critical cluster size seen in MD. This value of C is significantly smaller than 14-18, the

values obtained from fitting $J(T)$ with Eq. 2.23. The value of f_0 is also significantly smaller than fitted values of $\lambda \sim 10^{21-34}$. As noted before, similar fits to $J(T)$ can be obtained from Eq. 2.23 with very different parameters. Perhaps the calculated value of B, which depends sensitively on the surface tension, will compensate for our values of C and f_0.

4.2.5 Surface tension

Having obtained estimates of ΔH, A, f_0, C and seeing that the fits of $J(T)$ to Eq. 2.23 yield values of T_m close to the bulk value, we can obtain estimates of the fit parameters B and λ from estimates of γ from the literature. Studies of crystal nucleation in bulk LJ liquid report values of $\gamma = 0.28$ to 0.30 for $T = 0.43$ and 0.45, respectively [46], and these compare favourably with the surface tension of a flat interface at the same T [48].

Using average value of our estimates for the various parameters, namely, $\Delta H = 0.58N_p$, $A = 7.6$, $f_0 = 1 \times 10^7$ (geometric average), $C = 5.7$, and values of $T_m = 0.618$ (most recent for $p = 0$) [46] and $\gamma = 0.3$ [46] from the literature, we obtain $B = 2.0$ and $\lambda = 6.5 \times 10^8$. The resulting curve, according to Eq. 2.23 is not plotted anywhere because it fails to recover the rates in Fig. 4.3(b) by tens of orders of magnitude.

Conversely, we can use the fitted values of B to find the implied value of γ, keeping the other parameters as above. For $B = 0.54$, we obtain $\gamma = 0.194$ and for $B = 2.1$ we find $\gamma = 0.305$, which in principle look rather reasonable.

In the next section, we determine the effective surface tension felt by crystallites within the droplet through the calculation of $\beta\Delta G(n)$, and try to account for the disparity between our directly calculated rate and the one modelled through Eq. 2.23.

4.3 Free energy barriers

4.3.1 MFPT barrier reconstruction and MC calculations

In Fig. 4.11(a) we present the results at $T = 0.485$ from the MFPT barrier reconstruction and compare against MC results, where we give subscripts MC or MFPT to indicate the simulation method used. Formally speaking, this T is above the liquid-solid coexistence temperature, but we still can measure a rate and barrier out of the liquid to the crystal. The $\beta\Delta F(n)$ curves for both MC and MFPT have been shifted up by $\ln N_p$ as discussed in Section 2.2. The agreement between both methods is remarkably good until a point well past n^*. We obtain a similarly good comparison at $T = 0.480$. The inset shows $-\ln P^{\rm st}_{\rm max}(n)$ and a "quick" reconstruction of the barrier using Eq. 2.59, also showing satisfactory results. Parabolic fits within $\sim k_{\rm B}T$ of the maximum, allow us to determine Z, Z_F, $\beta\Delta G^*$, $\beta\Delta F^*$, n^* and n^*_F.

The results for $T = 0.475$ in Fig. 4.11(b) show a significant difference in the location of the maxima between MC and MFPT, i.e., n^*_F from MFPT is significantly larger than for n^*_F or n^* from MC. The MFPT curve is also significantly less curved at the top. As we discuss below, this discrepancy arises because the MC simulations are able to sample types of structures not as easily accessible to MD because of free energy or kinetic barriers. What is interesting, is that despite the significant difference in critical sizes and Zeldovich factors, the barrier heights are approximately the same from MC and MFPT.

In Fig. 4.12(a) we see that the discrepancy continues at $T = 0.450$, while by $T = 0.370$, shown in panel (b), a qualitative change has occurred. The $\beta\Delta F(n)$ curves for both MFPT and MC are monotonically decreasing. The interpretation of these results is laid out in Ref. [28], although in the context of the vapour to liquid transition but still above spinodal conditions. The monotonic decrease means that

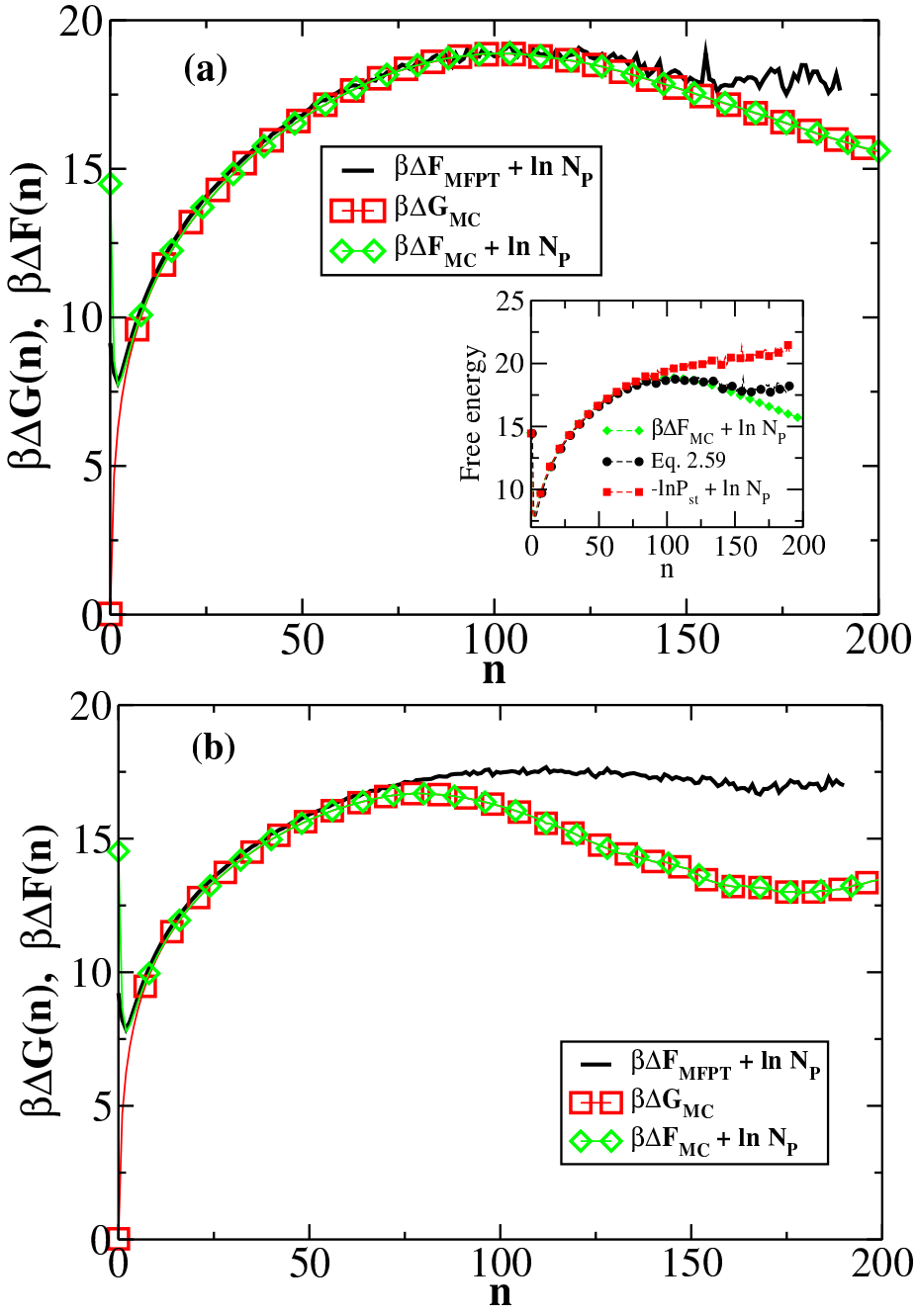

Figure 4.11: Barrier reconstruction from the steady-state probability distribution and $\tau(n)$ is successful at (a) $T = 0.485$, but by (b) $T = 0.475$, comparison with umbrella sampling MC results reveals a small difference in the barrier height, and a large discrepancy in the shape and location of the maximum. The inset in panel (a) shows results for using Eq. 2.59 to reconstruct the barrier.

for any value of $n_{\max}$, it is more probable for $n_{\max}$ to increase in size than to decrease. Thus the system has lost metastability and unavoidably transforms to the solid. However, the work of forming a critical embryo is still positive [$\beta\Delta G(n^*) \approx 8.5$]. So while the liquid phase is locally stable against fluctuations towards the liquid state, the system as a whole is not, since it is large enough to make it probable for a critical embryo to appear somewhere in the system on the time scale required for the diffusive attachment of particles. A crude analogy may be made with coin flipping. While it is improbable for a person flipping a coin to land 7 heads in a row, at which point the flipper is deemed to have reached a critical state, the time required for someone in a room with 100 people flipping coins to reach the critical state is the time required to flip a coin 7 times. At this T, therefore, transformation occurs through growth-limited nucleation.

4.3.2 T-dependence of barrier heights and critical embryo sizes

Between $T = 0.450$ and 0.370, as the difference between the minimum and maximum in $\beta\Delta F(n)$ becomes small, $n_{\min}$ increases while n_F^* decreases until the two meet, forming an inflection. For a small range of T above where this inflection forms, n_F^* decreases with lowering T faster than does n^*. Nonetheless, at the point where $\beta\Delta F_{\min}^*$ disappears, n_F^* is finite. A very similar scenario was encountered in Ref. [49] in the context of heterogeneous nucleation on a microscopic impurity, where it was shown that a finite barrier to nucleation remains at the limit of metastability (owing to the the finite size of n_F^*) and that it is incorrect to use $\beta\Delta F_{\min}^*$ in predicting the rate in an equation like Eq. 2.34.

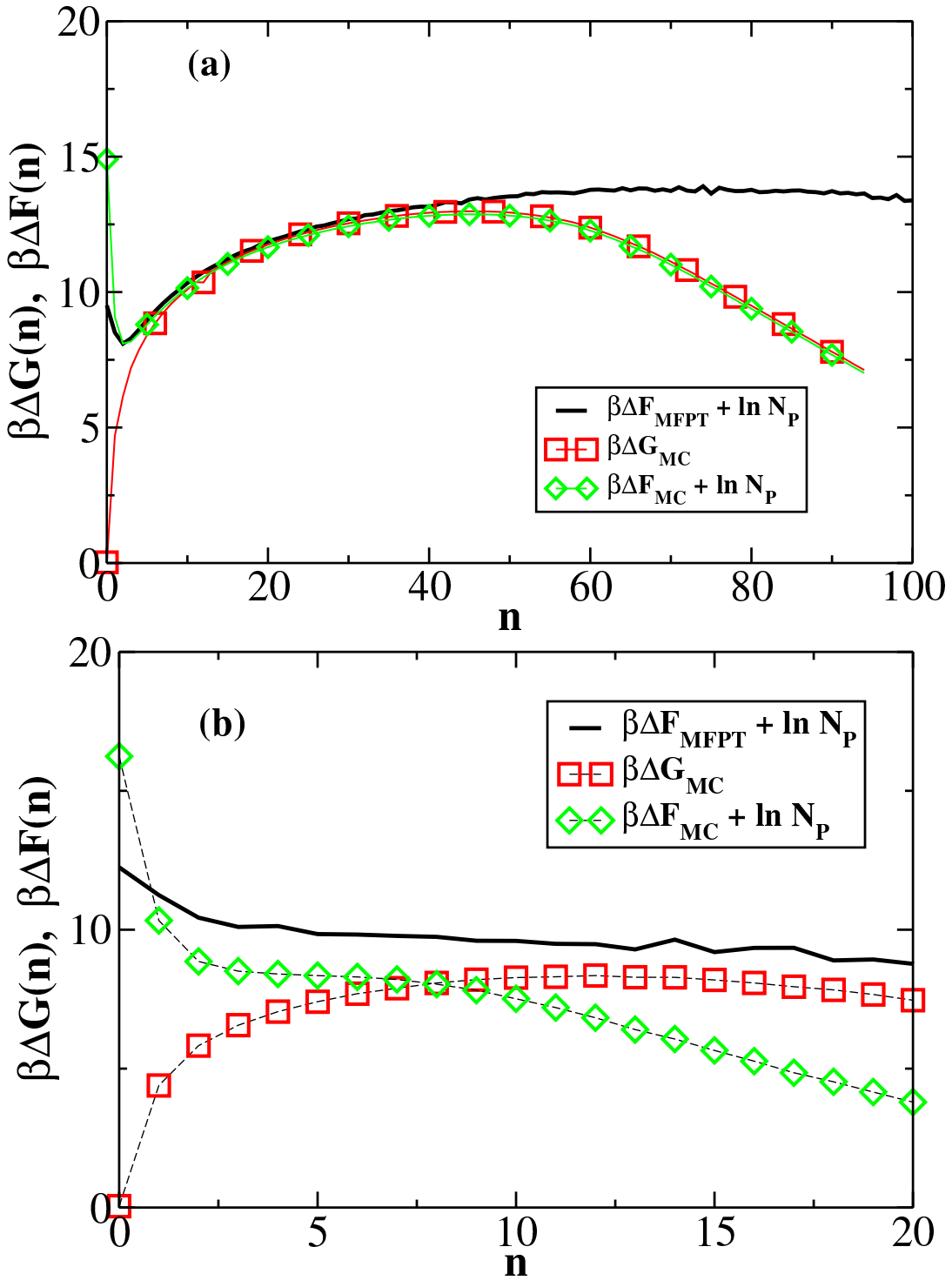

Figure 4.12: Barrier profiles. Panel (a) shows for $T = 0.450$ a similar discrepancy between MFPT and MC results obtained at $T = 0.475$. By $T = 0.370$, $\beta\Delta F(n)$ is monotonically decreasing, meaning liquid drop metastability is lost as the droplet enters a regime of unavoidable growth-limited nucleation.

The full T dependence of barrier heights is shown in Fig. 4.13(a), while that of critical embryo size in Fig. 4.13(b). For the barriers, all agree to within $1k_{\mathrm{B}}T$, despite more significant differences in n^*. The crystallization process becomes formally driven by growth-limited nucleation when $\beta\Delta F^*_{\mathrm{min}} = 0$ at $T = 0.395$, at which point $\beta\Delta G^* = 8.53$. In Ref. [28], the authors gave a simple criterion for the onset of growth-limit nucleation, namely that $P_{\mathrm{max}}(n^*) \approx 1$, or $\beta\Delta F(n^*) = 0$, which implies $\beta\Delta G^* \approx \ln N_p = 6.40$, which is roughly $2k_{\mathrm{B}}T$ lower than what we obtain. But as this is a rule of thumb, the prediction is quite good.

Below this cross-over temperature of $T_x = 0.395$, both $\beta\Delta G^*$ and n^* become constant. It is somewhat of a paradox that $\beta\Delta G^*$, an intensive property, should change its behaviour, or rather, its behaviour should become frozen in, when a system-size dependent condition is met, i.e., $\beta\Delta G^* \approx \ln N_p$. We discuss our thoughts on resolving this paradox below.

Having calculated the $\beta\Delta G(n)$, and hence obtained Z and n^* as well, we are now in a position to predict $J_{\mathrm{CNT}}(T)$ according to Eq. 2.20, and we show the result in Fig. 4.3(b). The agreement with J_b is rather good, showing the greatest discrepancy near $T = 0.4$, i.e., near the maximum rate and where growth-limited nucleation begins. In this region, a finer estimate of the rate, $J_{2\mathrm{n}^*}$ shows better agreement with J_{CNT}. Also shown in Fig. 4.3(b) is the kinetic prefactor Zf^+_{crit}. Similarly to what was observed in Ref. [28] for the vapour to liquid transition, once the growth-limited nucleation regime is entered, the kinetic prefactor dictates the T dependence of the rate. Here, however, the finite free energy barrier that remains in the growth-limited regime, gives rise to a rate that is about an order of magnitude slower than the kinetic prefactor alone.

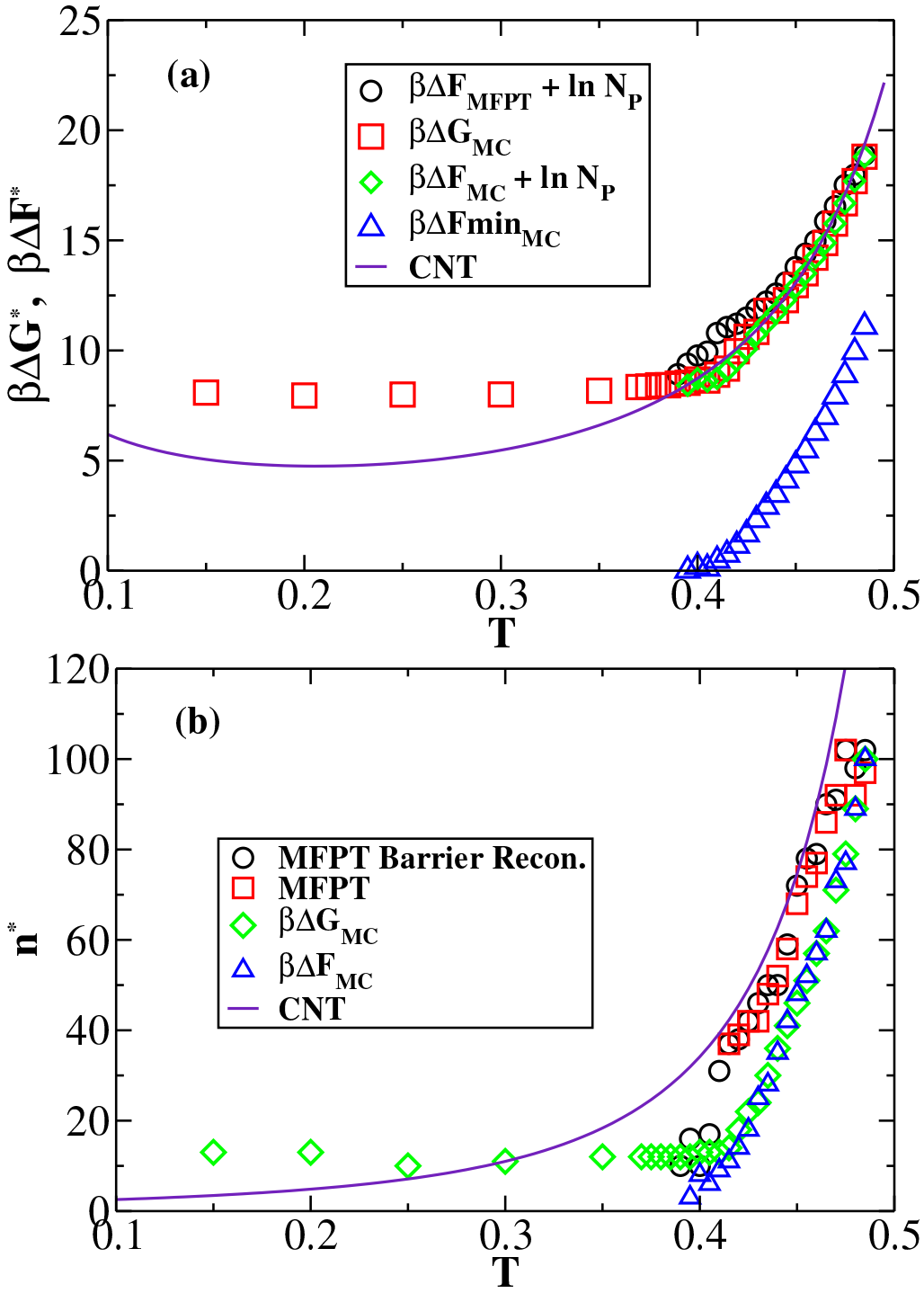

Figure 4.13: (a) Nucleation barrier heights as a function of T. Solid curve shows the prediction based on CNT after obtaining only $\gamma = 0.131$ from a fit to $J(T)$ via Eq. 2.23. $\beta\Delta F^*_{\rm min} = 0$ signals the onset of growth-limited nucleation. (b) Size of the critical cluster as a function of T from various estimates. Solid curve is the CNT prediction using the same parameters as for panel (a).

Eq. 2.20 is the CNT prediction of the rate that lacks any thermodynamic modelling of the work of forming a critical embryo. We have already seen that modelling $\beta\Delta G(n)$ through Eq. 2.9 and estimating the thermodynamic quantities that enter it and Eq. 2.23 give rise to vastly inaccurate rate predictions. However, given the simplicity of the modelling and the extreme sensitivity of the rate to the various parameters, e.g., the logarithm of the rate depends on γ^3 and ΔH^2, we can at least see whether the data and model support a self-consistent set of effective thermodynamic parameters and rationalize why they are different from the ones determined independently.

To this end, we plot in Fig. 4.14(a) for $T \geq 0.4$, where we expect Eq. 2.23 to work, the quantity $2\Delta G^*/n^*$, which according to Eq. 2.9 should equal $\Delta\mu(T)$, which in turn should be $\Delta\mu(T) = \Delta H(1-T/T_m)/N_p \approx \Delta u - \Delta u\, T/T_m$. For the MFPT data plotted, we use $\Delta G^* = \Delta F^*_{\mathrm{MFPT}} + \ln N_p$. The MFPT and MC data have different slopes on account of having different n^* below $T = 0.480$. Although linear fits to both MFPT and MC data sets look convincing, they yield values of $\Delta u = 0.83$ and 1.27, respectively, that are significantly higher than the calculated value of 0.58, by factors of 1.4 and 2.2, respectively. Similar discrepancies have been noted for MC studies of nucleation in Ref. [50], where across many state points the value of $\beta\Delta\mu$ obtained from fits to Eq. 2.9 were a factor of 2.5 higher than those calculated from thermodynamic integration, i.e., the true value.

In Fig. 4.14(b), we plot $\gamma = 3\Delta G^*/S^*$, which again follows from Eq. 2.9, where S^* is the area of the critical embryo. For a good range of both MC and MFPT data, γ is indeed constant, as assumed for Eq. 2.23. However, the value, as obtained from a fit to a constant of the MFPT data for $T \geq 0.41$, is 0.16, roughly half the value of the expected value of 0.3. In Fig. 4.3(b), we plot the result of using $\gamma = 0.167$ and $\Delta u = 0.83$ (giving $B = 0.168$ and $\lambda = 3.2 \times 10^9$) in Eq. 2.23, with rather satisfactory

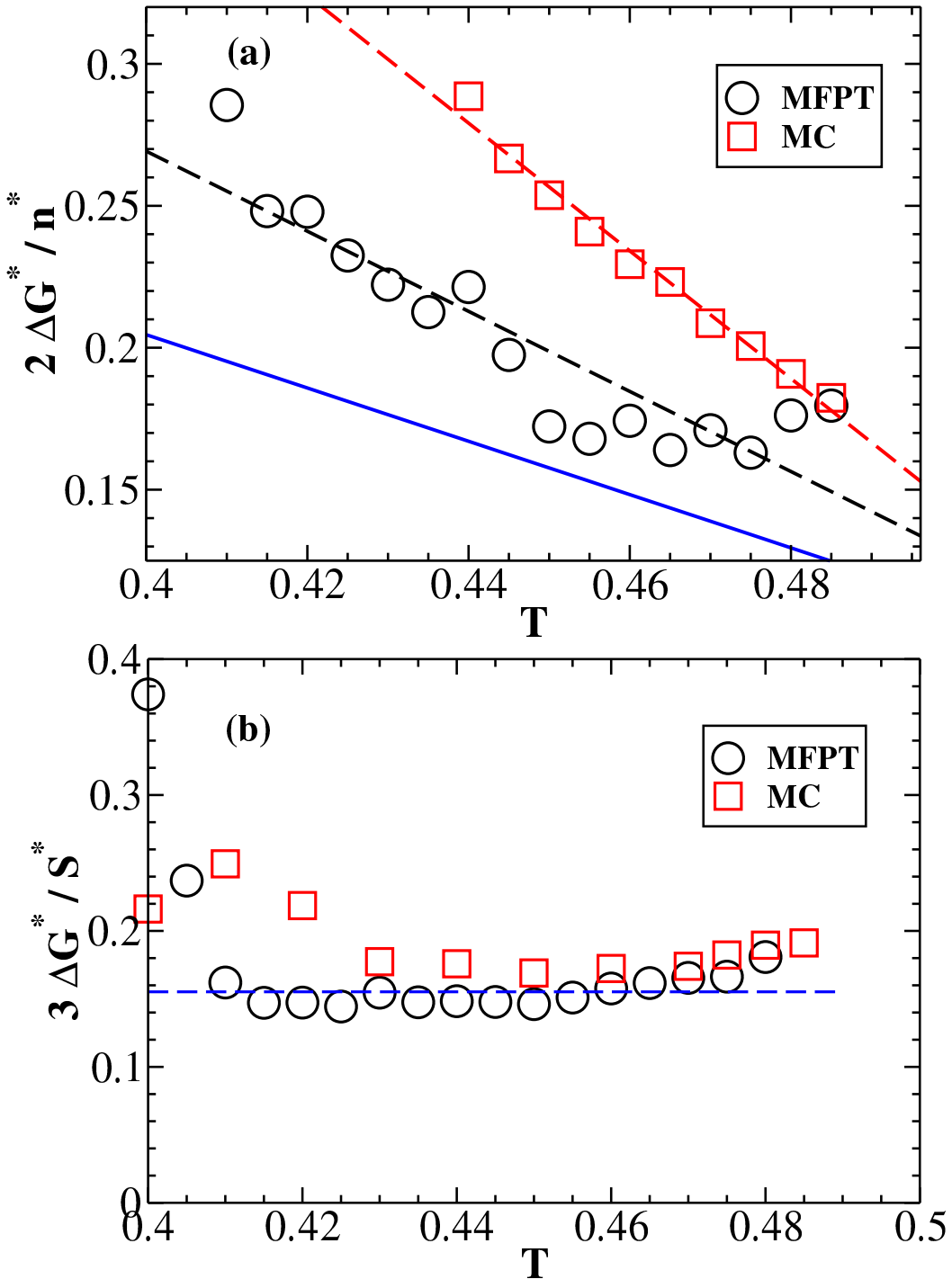

Figure 4.14: Panel (a) shows the CNT relation $\Delta\mu = 2\Delta G^*/n^*$ as a function of T. Blue solid line is $\Delta u - \Delta u T/T_m$, setting $T_m = 0.618$ and $\Delta u = 0.58$. Dashed lines are fits to data, with MFPT yielding $T_m = 0.591$ and $\Delta u = 0.83$, and MC yielding $T_m = 0.564$ and $\Delta u = 1.27$. Panel (b), $\gamma = 3\Delta G^*/S^*$ versus T. Dashed line is a fit to the MFPT data (from $T = 0.41$ and up) with a constant, yielding $\gamma = 0.155$, about half of the expected value of 0.3.

results.

Thus, while it is possible to arrive at effective values of γ and $\Delta\mu$ or Δu that give a very reasonable T dependence of the rate and that are consistent with the relationship between ΔG^* and n^* implied through Eq. 2.9, predicting these values from thermodynamics is difficult. The effective values of γ arising from CNT modelling tend to be significantly lower, while values of Δu (or equivalently, $\Delta\mu$) tend to be higher than thermodynamic values.

In fact, there is a family of curves for pairs of not unreasonable values of γ and Δu that produce similarly appealing curves, so long as $\gamma^3/\Delta u^2 = \text{const}$. Acknowledging that the value of n^* is more sensitive to the definition of an embryo than is $\beta\Delta G^*$, we set $\Delta u = 0.58$, our independently determined value, and find that a value of $\gamma = 0.131$ (yielding $B = 0.166$ and $\lambda = 2.3 \times 10^9$ with f_0, C, A and T_m also at their independently determined values) produces $J_{\mathrm{CNT}}(T)$ according to Eq. 2.23 that fits the MD rates rather well. With these parameters, the CNT prediction for $\beta\Delta G^*$ from Eq. 2.24 in Fig. 4.13(a) is rather good down to $T = 0.395$. The CNT prediction $n^* = 2Bk_{\mathrm{B}}T_m/[\Delta u(T_m - T)^3]$ produces somewhat larger values than those directly obtained, as shown in Fig. 4.13(b). This means that a one-parameter fit of the rate for γ reproduces the rate well, $\beta\Delta G^*$ well, but yields a value of γ that is significantly lower than expected.

Expanding on this last point, we plot again in Fig. 4.15 $\beta\Delta G_{\mathrm{MC}}(n)$ from $T = 0.485$, along with three fits to Eq. 2.9 using 20 points on either side of the maximum: setting $A = 7.6$ and $\beta\Delta\mu = 0.257$ as calculated from Eq. 2.21 with $\Delta u = 0.58$ and $T_m = 0.618$, yielding $\gamma = 0.132$ and a significantly larger n^*; setting $A = 7.6$, yielding $\beta\Delta\mu = 0.370$ and $\gamma = 0.165$; and setting $An^{2/3}$ to a fit to the data for $S(n)$ at $T = 0.485$ shown in Fig. 4.7 upper inset, yielding $\beta\Delta\mu = 0.168$ and $\gamma = 0.118$. All three curves yield similar values of $\beta\Delta G^*$ with significantly different values of $\beta\Delta\mu$

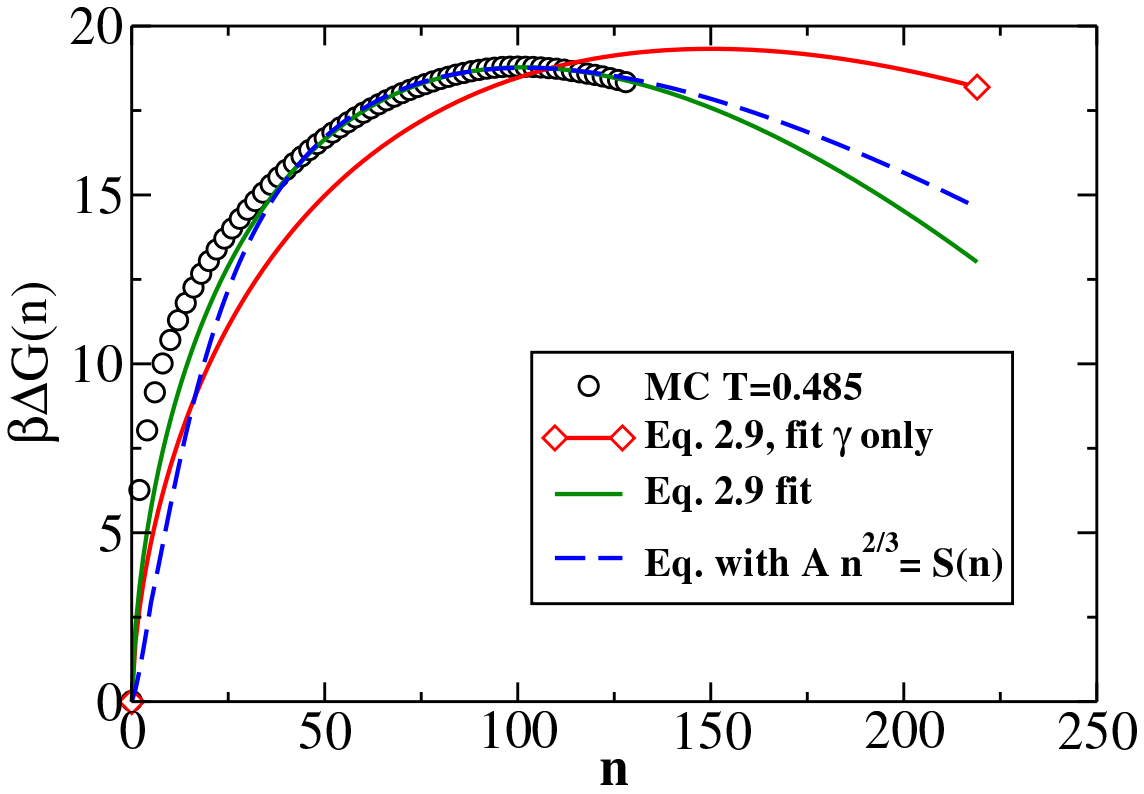

Figure 4.15: $\beta\Delta G(n)$ from $T = 0.485$ (circles) with fits to Eq. 2.9. The red curve (with diamond) uses our calculated value of $\beta\Delta\mu = 0.257$ to obtain $\gamma = 0.132$ in a one-parameter fit. The green curve obtains $\beta\Delta\mu = 0.370$ and $\gamma = 0.165$ from fitting. The dashed blue curve replaces $An^{2/3}$ in Eq. 2.9 with $S(n)$ obtained from $T = 0.485$, yielding $\beta\Delta\mu = 0.168$ and $\gamma = 0.118$.

and γ, with γ in all case significantly smaller than the expected value of 0.3. This is consistent with reports that different criteria for defining a crystalline particle yield curves with the same $\beta\Delta G^*$ but different n^* [51]. The curve where we included an n dependence of the area of the embryo is an unsuccessful attempt to correct the deviation of the first fit from $\beta\Delta G(n)$ at small n.

4.3.3 Escape from the critical state

We now explore the differences in n^* between MC and MFPT results that begin to be felt at $T = 0.475$. According to MFTP, $n^* \approx 100$. In Fig. 4.16 we plot the probability

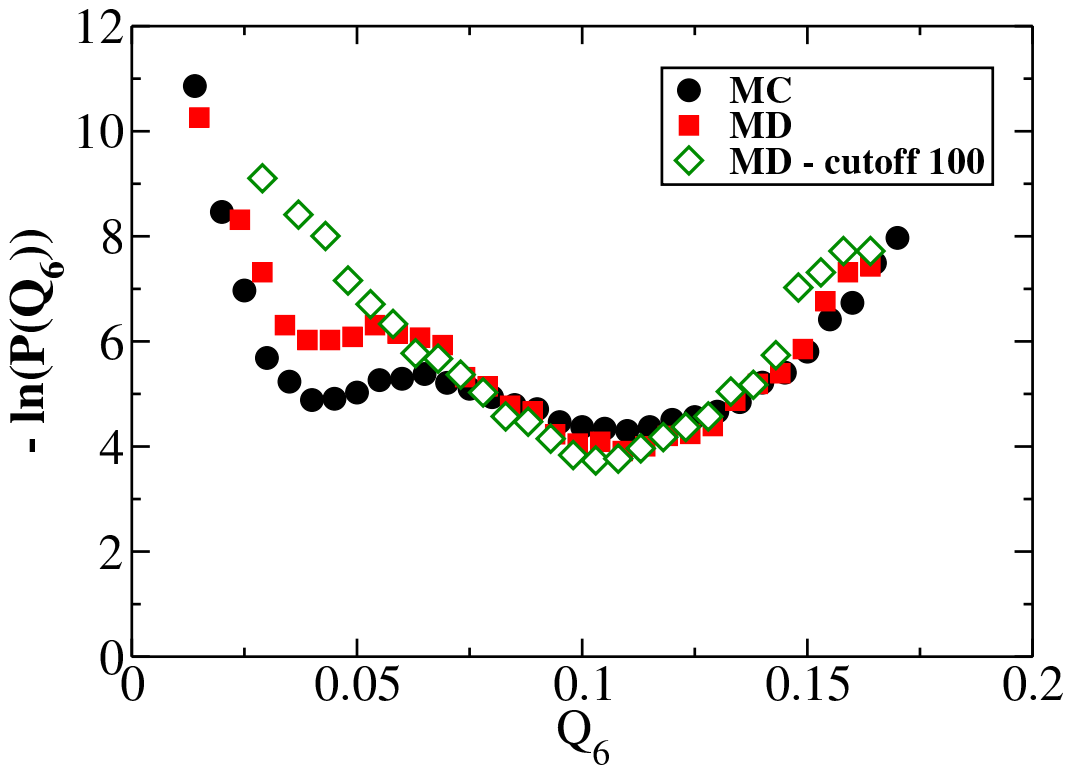

Figure 4.16: Probability distribution for Q_6 at $T = 0.475$ for $60 \leq n_{\max} \leq 100$.

density $P(Q_6)$ for Q_6, a global measure of the crystallinity of the system as a whole. We plot the negative of the logarithm of the distribution in order to view it as a free energy. Generally speaking, two factors contribute to the value of Q_6, the number of crystal-like particles and the relative orientation of crystallites. For example, Q_6 will grow as the size of an fcc crystallite increases, but a large icosahedral embryo of similar size consisting of 20 fcc tetrahedra sharing a vertex, will have a lower value of Q_6.

In the first instance we calculate $P(Q_6)$ from MD crystallization trajectories, using data up to the first time that $n_{\max}$ reaches 100, utilizing all configurations with $60 \leq n_{\max} \leq 100$. In this way, we consider embryos in the critical region but do not allow embryos to sample states beyond the critical size. The result is a unimodal $P(Q_6)$ with a preferred value of $Q_6 = 0.1$. We refer to this value of Q_6 as *high*. If

we consider embryos from all times along the trajectory, i.e., we allow the system to sample post-critical states and subsequently shrink back into the pre-critical region, the distribution changes by exhibiting a localized preference for $Q_6 = 0.04$ [a shallow minimum in $-\ln P(Q_6)$]. We refer to this value of Q_6 as *low*. Finally, we carry out MC simulations with hard wall constraints to enforce $60 \leq n_{\max} \leq 100$. The resulting fee energy, also shown in Fig. 4.16, shows that the relative preferences for high and low Q_6 structures are similar, but that there is a free energy barrier separating the two. Thus, although there exist qualitatively different equilibrium structures in the critical region (same $n_{\max}$, different Q_6), MD trajectories do not easily sample the low Q_6 states until after embryos have crossed into the post-critical region. The kinetics of crossing the small barrier for $n_{\max} \leq 100$ are apparently significantly slower than structural changes occurring for $n_{\max} > 100$.

To develop a better picture of the process, we use the data from Fig. 4.16 to construct two-dimensional probability distributions in both Q_6 and $n_{\max}$. The results are plotted in Fig. 4.17 as contour plots of $-\ln P(n_{\max}, Q_6)$. For the equilibrium MC data in panel (a), we see a single trough coming into the critical region from $n_{\max} = 60$ and $Q_6 = 0.1$ that becomes fairly flat at larger $n_{\max}$. An exiting trough at low Q_6 develops near $n_{\max} = 70$ that becomes comparable in free energy to the incoming trough near $n_{\max} = 80$. While the apparent barrier in the MC data for the one-dimensional case is largely due to the existence of the high Q_6 trough entering the region and the low Q_6 trough exiting the region, there still exists a very faint barrier separating the two Q_6 states at $n_{\max} = 100$ and somewhat larger barriers separating the two for smaller $n_{\max}$. By $n_{\max} = 100$, the low Q_6 exiting trough has a lower free energy than the high Q_6 flattened out trough.

Panel (b) of Fig. 4.17 shows MD data where post-critical embryos that retrace back below $n_{\max} = 100$ are counted. We see the noisy appearance of the low Q_6

exiting trough and a steepening of the of the incoming trough. For the MD data case that does not consider embryos with $n_{\max} > 100$, shown in panel (c), there is only the incoming high Q_6 trough with a maximum forming at $n_{\max} = 100$. The low Q_6 states are not visited.

Thus, while it is possible for $n_{\max} < 100$ embryos to transform from high to low Q_6, and both states have similar free energies, the kinetics of exploring across Q_6 are much slower than exploring along $n_{\max}$, at least in the range of $n_{\max}$ considered. What we do not see, are two competing pathways entering the critical region. The exiting trough only forms near the critical region.

While we leave a more detailed study of these transformations near the critical region for the future, we show in Fig. 4.18 a series of snapshots of critical configurations from $T = 0.485$ down to $T = 0.200$. For $T = 0.465$ and above, we select both high and low Q_6 specimens. We assign particle types (fcc, hcp, icosahedral) through common neighbour analysis [52,53], which distinguishes between local structure by considering the number of common neighbours two nearest neighbours share, as well as how those common neighbours are bonded. Before carrying out the CNA analysis, we identify the particles in the largest embryo, and then carry out a conjugate gradient quench of the system to remove vibrational displacements. It is these quenched structures that are presented in Fig. 4.18, with particles originally in the largest embryo colour-coded, and the rest of the particles appearing in a faint shade.

While we present here only a handful of structures, the picture that emerge seems rather robust. The high Q_6 structures, Fig. 4.18(a, c, e), appear to be stackings of fcc and hcp layers, while the low Q_6 structures appear to be multiply twinned structures, rich in hcp, and possessing 5-fold symmetry. For the lower T shown, the critical embryos are small and do not show secondary organization, but appear to be high in fcc. Thus the embryos belonging to the incoming free energy trough in Fig. 4.17

appear to be randomly close-packed structures, while differentiation to structures suggestive of icosahedra or decahedra, occurs as these embryos approach critical size.

For reference, we list various calculated quantities in Table B.1 in Appendix B.

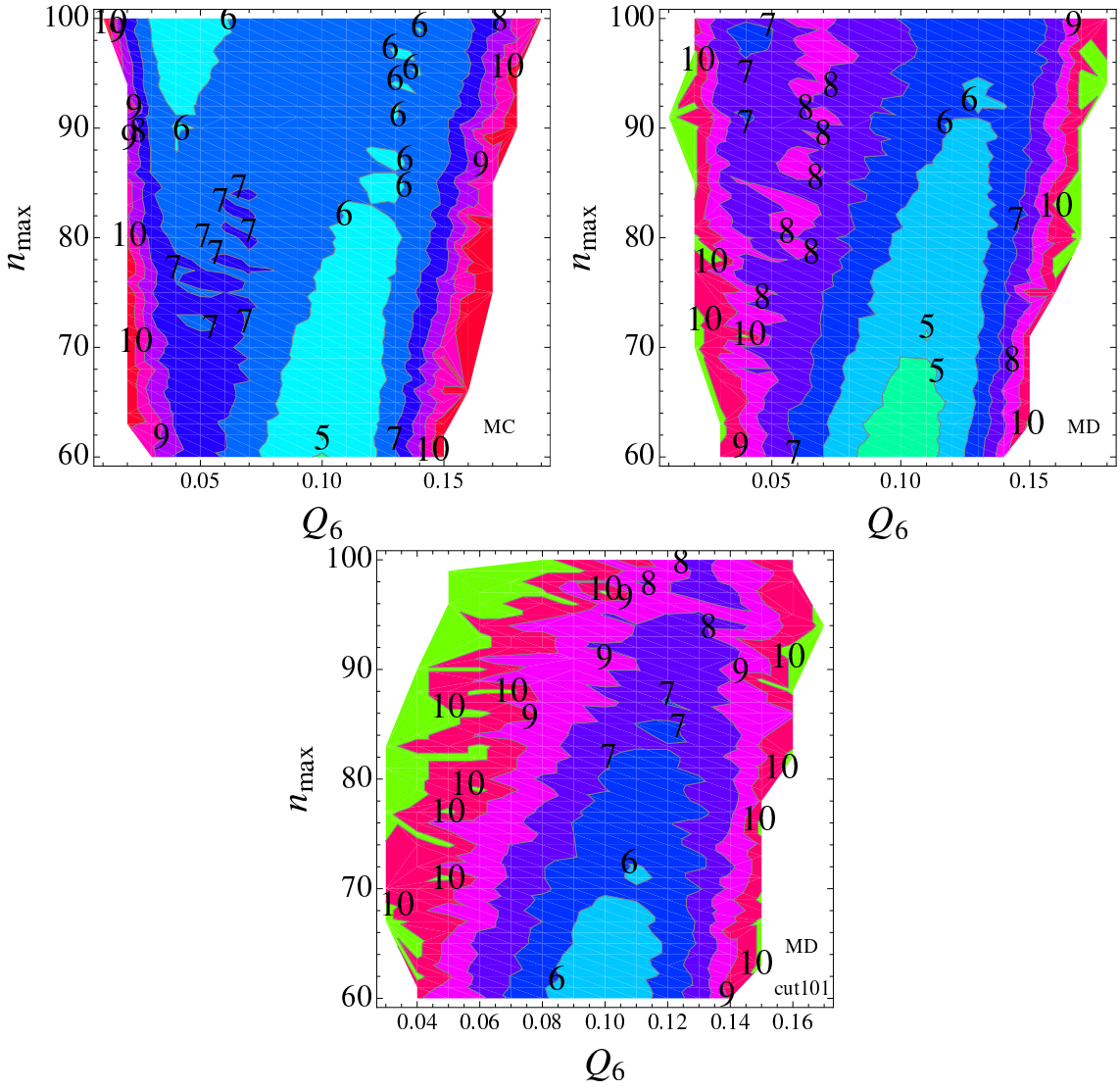

Figure 4.17: Joint probability distributions for $n_{\max}$ and Q_6 at $T = 0.475$. Plotted is $-\ln P(n_{\max}, Q_6)$ for (a) MC, (b) MD, (c) MD without allowing retracing to $n_{\max} \leq 100$. The contour lines are in increments of 1.

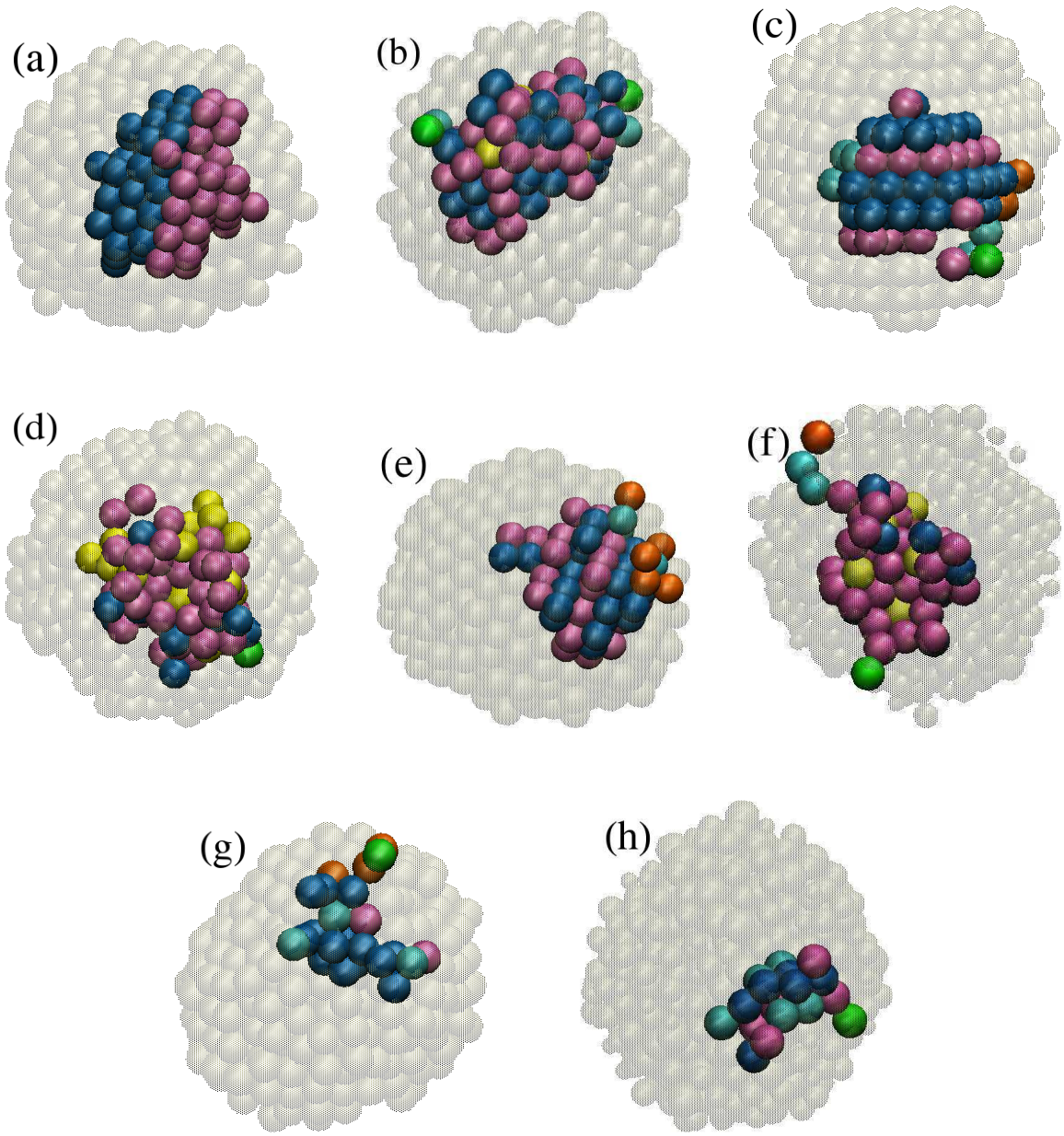

Figure 4.18: Droplet configurations containing critical embryos for (a) $T = 0.485$, $Q_6 = 0.176$, $n_{\max} = 98$, (b) $T = 0.485$, $Q_6 = 0.086$, $n_{\max} = 100$, (c) $T = 0.475$, $Q_6 = 0.129$, $n_{\max} = 79$, (d) $T = 0.475$, $Q_6 = 0.040$, $n_{\max} = 76$, (e) $T = 0.465$, $Q_6 = 0.111$, $n_{\max} = 63$, (f) $T = 0.465$, $Q_6 = 0.038$, $n_{\max} = 65$, (g) $T = 0.425$, $Q_6 = 0.078$, $n_{\max} = 24$, (h) $T = 0.200$, $Q_6 = 0.078$, $n_{\max} = 18$, The colouring scheme: blue, bulk fcc; mauve, bulk hcp; yellow, bulk icosahedral; cyan, unidentified (amorphous); green, 111 surface; orange, 100 surface; particles not part of the critical embryo, transparent tan.

Chapter 5

Discussion

Part of the motivation for the work done for this thesis comes from previous studies on the interpretation of $\beta\Delta F^*_{\rm min}$ approaching zero, its relation to nucleation rates and liquid metastability and the appropriateness of using the largest embryo in the system as an order parameter. While previous work misidentified this barrier disappearance as a condition for a spinodal (and the refutation of this pointed out its size dependence) [54], it clearly signalled some sort of limit to metastability. The recent scenario laid out in Ref. [28], namely that it signals unavoidable crystallization achieved through growth-limited nucleation, is supported by our work. By growth-limited nucleation we mean that with near certainty, somewhere in the system a critical nucleus will form through $\sim n^*$ consecutive particle additions, and so crystallization is controlled by the rate at which liquid-like particles attach themselves to crystal-like ones. This is what we see when we predict the rate through Eq. 2.20, which matches MD rate determination for the entire range of T, as seen in Fig. 4.3(b).

The case of gold particles studied in Ref. [21] remains a bit of a mystery, in that below $\beta\Delta F^*_{\rm min} = 0$, $\beta\Delta G^*(T)$ remains flat, while the rate increased. In order for Eq. 2.20 to work in this case, the attachment rate would need to increase with

decreasing T. Perhaps some surface effect is responsible for such behaviour.

For our LJ clusters, where nucleation originates within the bulk, CNT as formulated for homogeneous nucleation for bulk liquids works quite well. We see that a controlling factor, despite the presence of the surface, is the temperature at which $\Delta\mu = 0$ in bulk systems. This T_m from the bulk governs nucleation even in our finite-sized system where the melting temperature T_m^c is significantly lower than T_m.

We find that the simple modelling often used in CNT, such as constant γ, ΔH and A, and Arrhenius temperature dependence of $f_{\rm crit}^+$ is supported by our results in independently determining these quantities. Using these quantities as calculated, except for changing the surface tension value to $\gamma = 0.131$, results in very good consistency between thermodynamics and rates, at least for $T > 0.40$. There is some ambiguity regarding the values of ΔH, or rather $\Delta\mu$, and γ when using the CNT model in Eq. 2.9 to compare independently calculated $\beta\Delta G(n)$. The shape of the curves is quite different, particularly at small n, and changing the model slightly or fitting different portions of the curve results in quite different values of $\Delta\mu$ and γ. While this is less of a problem for large embryos, it would be satisfying to achieve better comparison for smaller embryos as well. A more detailed examination of the crystal-liquid interface, as well as of the very initial stages of nucleation would be helpful in this regard.

The temperature $T_x = 0.395$ at which system metastability is lost and growth-limited nucleation sets in is well approximated by the condition $\beta\Delta G^* = -\ln N_p$ [28]. As mentioned above, it is strange that the behaviour of $\beta\Delta G(n)$, an intensive property, should alter its behaviour and stop evolving with T, as in Fig. 4.13(a), once this system size dependent condition is met. The sudden flattening of $\beta\Delta G^*(T)$ at T_x either implies that there is a sudden change in one or more of the parameters appearing in B, or that the system is not in equilibrium below T_x, even within our constrained

MC simulations. Plotted for comparison in Fig. 4.13(a) is the behaviour of $\beta\Delta G^*$ expected from CNT given in Eq. 2.24. Falling out of equilibrium at and below T_x is understandable in that as the liquid equilibrates from $T = 0.53$ to the $T \leq T_x$ set by the thermostat, it must pass through a point at which its configurational properties are characteristic of T_x, where crystallization proceeds in a down-hill fashion. Thus, for $T < T_x$, the metastable liquid does not progress beyond T_x in terms of a configurational temperature. That the system as a liquid does not reach metastable equilibrium is an idea supported by the potential energy time series at low T. The ability for the liquid to undergo significant diffusive motion (enough to form critical embryos) while not equilibrating itself may be due to a decoupling of diffusive and collective relation time scales characteristic of glassy dynamics [55].

As for the MC simulations, the constraint should allow for equilibration to occur since the size of the largest embryo is constrained. It is perhaps likely that relaxation of the metastable liquid requires significantly longer times than our MC of 500000 iterations (5×10^6 displacement attempts per particle). And yet, the MC data produce rate predictions matching MD rate results (J_b) quite well even below T_x, so this "early time" barrier may be the required quantity to measure. Questions about the relaxation of the liquid surrounding embryos are perhaps more easily addressed in bulk systems, where determining the dynamics of the system is somewhat more straightforward in the absence of a surface. Perhaps carefully equilibrated MC simulations will be able to probe lower T to see if in fact ΔG^* disappears at a spinodal, where the liquid phase itself becomes unstable. However, it is unclear what dynamical signatures would be present, for example, in the $\tau(n)$ curves.

Commenting on early work [30], where the free energy was calculated as a function of Q_6-based determinations of the bulk and surface crystallinity, at $T = 0.475$ the barrier separating the liquid from a low Q_6 5-fold structure was $0.5k_{\mathrm{B}}T$ or less (as

calculated by subtracting from the free energy of the saddle point the minimum value in the liquid basin), implying that the system as a liquid had (practically) lost stability at this T. However, here we see that at $T = 0.475$, $\beta\Delta F^* = 10$, which is considerably higher. Thus, care must be taken when gauging phase stability from free energies based on Q_6, as there are crystal-like states with values of Q_6 that overlap with those of the liquid.

In reconstructing barriers from MD data through the MFPT formalism, choosing an appropriate value of the absorbing boundary is not as straightforward as for the bulk system because of the presence of partially crystallized states of the cluster. However, we do achieve consistent results between MC and MFPT, up until the appearance of structures with 5-fold symmetry with free energies that compete with those of hcp-fcc stacked structures as they approach critical size. For $T \leq 0.475$ the MFPT reconstructions continue to yield very similar barrier heights to MC, but somewhat larger value of n^*.

The picture that emerges, based on limited calculations, is that pre-critical nuclei or of one type, layered hcp-fcc planes, but (at least) two type of structures, with different Q_6 values, leave the critical region. A small barrier in Q_6 appears to separate the two, thus preventing MD simulations from sampling the low Q_6 states until the embryo exceeds the critical size. It seems that small icosahedral nuclei are unfavourable. As nucleation studied here occurs within the bulk of the cluster, perhaps a similar scenario occurs in bulk LJ. We look forward to exploring these issues in more detail in the near future.

Chapter 6

Conclusions

We have calculated the rate of nucleation in a cluster of 600 LJ particles by calculating mean first-passage times of the largest embryo in the system through MD simulations. For several orders of magnitude, the rate follows expectations from CNT under the simplest of assumptions, namely a constant (ellipsoidal) shape of crystallites, a constant enthalpy difference, Arrhenius dependence of the attachment rate, a melting temperature following from the bulk and a constant surface tension. Treating the surface tension as a fitting parameter while independently calculating the other quantities results in excellent agreement with the temperature dependence of the rate and the work of forming critical nuclei, albeit with a rather small effective surface tension of $\gamma = 0.131$ and larger than expected critical embryo sizes, from $T = 0.485$ down to $T \approx 0.40$.

The apparent values of γ and $\Delta\mu$ can be increased in a way consistent with CNT as to largely preserve agreement on $\beta\Delta G^*$ and $J(T)$, but with a resulting change in n^*. This is consistent with observations that different criteria for defining embryo sizes in simulations result in different n^* but similar $\beta\Delta G^*$ [51]. A more careful approach to modelling the crystal-liquid interface as well as the initial stages of nucleation may

reduce this ambiguity.

Near $T_x = 0.4$, the rate starts approaching a maximum as the system loses its ability to maintain metastability, as evidenced by a monotonically decreasing free energy as a function of the largest cluster size. At and below this temperature, crystallization proceeds through growth-limited nucleation. The liquid phase is not inherently unstable itself, as there is a finite work required to form critical nuclei, but rather the barrier has become sufficiently small, as determined approximately by $\beta\Delta G^* = \ln N_p$. This picture follows what was observed for the vapour-liquid transition [28].

Below T_x, $\beta\Delta G^*$ and n^* become constant with T, departing from CNT expectations. We speculate that this perhaps indicates that nucleation for $T < T_x$ proceeds in the still-equilibrating liquid as its configurational properties reach those that are characteristic of the liquid at T_x. If this is true, reaching a predicted mean-field spinodal would be difficult to achieve in this system.

Regarding the spinodal scenario and the large predicted anisotropy of critical embryos at small T, we note that the anisotropy of critical embryos from different temperatures follows the same size dependence of the anisotropy of embryos taken at a single high T. Therefore, for the rather anisotropic critical embryos we observe at lower T, there is no anomalous increase in anisotropy as T decreases. If the spinodal exists, we do not detect its effects.

Surprisingly robust are the excellent predictions of the rate from MC-based calculations of $\beta\Delta G^*$, Z and $f^+_{\rm crit}$. The predictions match the rate over the entire T range studied.

Using the MFPT approach to reconstruct the free energy barrier gives the same results as MC calculations at high T. Related to this agreement is the proper normalization, or proper identification of the reference state, when using the free energy

with largest cluster size as an order parameter to predict the nucleation rate. Simply taking the difference between the minimum and the maximum of $\beta\Delta F(n)$ is incorrect, especially when barriers become low.

For our system, the free energy curves obtained from MFPT and MC show discrepancies in shape and n^* (but not so much in height) because of the appearance of embryos with twinned structures exhibiting 5-fold symmetry. The differentiation between these and hcp-fcc stacked structures happens only in the critical region; pre-critical nuclei do not seem to possess the 5-fold symmetry of the icosahedral structures to which LJ clusters often freeze. In the critical region, there appears to be a small free energy barrier with Q_6 as an order parameter between the hcp-fcc and 5-fold structures, inhibiting MD trajectories from sampling the same structures accessible to constrained MC simulations. Small barriers obtained using Q_6, or indeed global order parameters in general, are not necessarily good indicators of phase stability or ease of transition kinetics.

Bibliography

[1] A. Puzder, A. J. Williamson, J. C. Grossman, and G. Galli, *Surface control of optical properties in silicon nanoclusters.* J. Chem. Phys. **117**, 6721 (2002).

[2] F. Iori, S. Ossicini *Effects of simultaneous doping with boron and phosphorous on the structural, electronic and optical properties of silicon nanostructures.* PHYSICA E **41**, 939 (2009).

[3] T. Shimizu-Iwayama, N. Kurumado, D. E. Hole, and P. D. Townsend, *Optical properties of silicon nanoclusters fabricated by ion implantation.* J. Appl. Phys. **83**, 6018 (1998).

[4] W. Kruppa, M. G. Ancona, R. W. Rendell, A. W. Snow, E. E. Foos and R. Bass *Electrical noise in gold nanocluster sensors.* Appl. Phys. Lett. **88**, 053120 (2006).

[5] V. Venkatesh, A. Shukla, S. Sivakumar, and S. Verma, *Purine-Stabilized Green Fluorescent Gold Nanoclusters for Cell Nuclei Imaging Applications.* ACS Appl. Mater. Interfaces **6**, 2185 (2014).

[6] A. Visikovskiy, K. Mitsuhara, and Y. Kido *Role of gold nanoclusters supported on TiO2(110) model catalyst in CO oxidation reaction.* J. Vac. Sci. Technol. A **31**, 061404 (2013).

[7] K. Mitsuhara, M. Tagami, T. Matsuda, A. Visikovskiy, M. Takizawa, and Y. Kido *The mechanism of emerging catalytic activity of gold nano-clusters on rutile TiO2(110) in CO oxidation reaction.* J. Chem. Phys. **139**, 124303 (2012).

[8] M. Penza, G. Cassano, R. Rossi, M. Alvisi, A. Rizzo, M. A. Signore, Th. Dikonimos, E. Serra and R. Giorgi *Enhancement of sensitivity in gas chemiresistors based on carbon nanotube surface functionalized with noble metal (Au, Pt) nanoclusters.* Appl. Phys. Lett. **90**, 173123 (2007).

[9] F. Baletto and R. Ferrando, *Structural properties of nanoclusters: Energetic, thermodynamic, and kinetic effects.* Rev. Mod. Phys. **77**, 371 (2005).

[10] J. Farges, M. F. de Feraudy, B. Raoult, and G. Torchet, *Noncrystalline structure of argon clusters. I. Polyicosahedral structure of Ar_N clusters, 20<N<50.* J. Chem. Phys. **112**, 5067 (1983).

[11] J. Farges, M. F. de Feraudy, B. Raoult, and G. Torchet, *Noncrystalline structure of argon clusters. II. Multilayer ichosahedral structure of Ar_N clusters, 20<N<50.* J. Chem. Phys. **84**, 3491 (1986).

[12] D. J. Wales and J. P. K. Doye, *Global optimization by basin-hopping and the lowest energy structures of Lennard-Jones clusters containing up to 110 atoms.* J. Phys. Chem. A **101**, 5111 (1997).

[13] D. J. Wales, *Energy Landscapes with Applications to Clusters, Biomolecules and Glasses* (Cambridge University Press, Cambridge, 2003).

[14] B. Raoult, J. Farges, M. F. de Feraudy, and G. Torchet, *Comparison between icosahedral, decahedral, and crystalline Lennard-Jones models containing 500 to 6000 atoms.* Philos. Mag. B **60**, 881 (1989).

[15] Y. Xiang, L. Cheng, W. Cai, and X. Shao, *Structural Distribution of Lennard-Jones Clusters Containing 562 to 1000 Atoms.* J. Chem. Phys. **108**, 9516 (2004).

[16] J. P. K. Doye, M. A. Miller, and D. J. Wales, *The double-funnel energy landscape of the 38-atom Lennard-Jones cluster.* J. Chem. Phys. **110**, 6896 (1999).

[17] V. A. Mandelshtam and P. A. Frantsuzov, *Multiple structural transformations in Lennard-Jones clusters: Generic versus size-specific behavior.* J. Chem. Phys. **124**, 204511 (2006).

[18] E. G. Noya and J. P. K. Doye *Structural transitions in the 309-atom magic number Lennard-Jones cluster.* J. Chem. Phys. **124**, 104503 (2006)

[19] P. G. Debenedetti, *Metastable Liquids: Concepts and Principles* (Princeton University Press, Princeton,1996)

[20] C. C. Asuquo, R. K. Bowles, *Molecular dynamics simulations of competitive freezing in gold nanoclusters.* J. Chem. Phys. **116**, 14619 (2012).

[21] E. Mendez-Villuendas, I. Saika-Voivod, and R. K. Bowles, *A limit of stability in supercooled liquid clusters.* J. Chem. Phys. **127**, 154703 (2007).

[22] J. W. Cahn and J. E. Hilliard, *Free Energy of a Nonuniform System. III. Nucleation in a TwoComponent Incompressible Fluid.* J. Chem. Phys. **31**, 688 (1959); W. Klein and F. Leyvraz, *Crystalline Nucleation in Deeply Quenched Liquids.* Phys. Rev. Lett. **57**, 2845 (1986); Ju-xing Yang, H. Gould, and W. Klein, *Molecular-Dynamics Investigation of Deeply Quenched Liquids.* Phys. Rev. Lett. **60**, 2665 (1988).

[23] F. Trudu, D. Donadio, and M. Parrinello, *Freezing of a Lennard-Jones Fluid: From Nucleation to Spinodal Regime.* Phys. Rev. Lett. **97**, 105701 (2006).

[24] H. Wang, H. Gould, and W. Klein, *Homogeneous and heterogeneous nucleation of Lennard-Jones liquids* Phys. Rev. E **76**, 031604 (2007).

[25] L. S. Bartell and D. T. Wu, *Do supercooled liquids freeze by spinodal decomposition?* J. Chem. Phys. **127**, 174507 (2007).

[26] J. Wedekind, R. Strey, and D. Reguera, *New method to analyze simulations of activated precesses.* J. Chem. Phys. **126**, 134103 (2007).

[27] J. Wedekind, and D. Reguera *Kinetic Reconstruction of the Free-Energy Landscape.* J. Phys. Chem. B **112**, 11060 (2008).

[28] J. Wedekind, G. Chkonia, J. Wolk, R. Strey, and D. Reguera, *Crossover from nucleation to spinodal decomposition in condensing vapor.* J. Chem. Phys. **131**, 114506 (2009).

[29] E. Mendez-Villuendas and R. K. Bowles, *Surface nucleation in the freezing of gold nanoparticles.* Phys. Rev. Lett. **98**, 185503 (2007).

[30] I. Saika-Voivod, Louis Poon and R.K. Bowles, *The role of FCC tetrahedral subunits in the phase behavior of medium sized Lennard-Jones clusters.* J. Chem. Phys. **133**, 074503 (2010).

[31] H. Reiss, *Methods of Thermodynamics* (Blaisdell Publishing Company, New York 1965)

[32] S. P. Das, *Statistical Physics of Liquids at Freezing and Beyond* (Cambridge University Press, New York, 2011).

[33] F.F. Abraham, *Homogeneous nucleation theory; the pretransition theory of vapor condensation* (Acadmic Press, New York 1974))

[34] N. Okui, *Relationship between crystallization temperature and melting temperature in crystalline materials.* J. Mater. Sci. **25** 1623 (1990).

[35] P. Hanggi, P. Talkner, and M. Borkovec *Reaction-rate theory: fifty years after Kramers.* Rev. Mod. Phy. **62**, 251 (1990).

[36] D. Frenkel and B. Smit, *Understanding Molecular Simulation: From Algorithms to Applications* (Academic, New York, 2002).

[37] M. P. Allen and D. J. Tildesley, *Computer simulation of liquids* (Oxford University Press, New York, 1989).

[38] S. Auer and D. Frenkel, *Numerical prediction of absolute crystallization rates in hard-sphere colloids.* J. Chem. Phys. **120**, 3015 (2004).

[39] M. R. Shirts and J. D. Chodera, J. Chem. Phys. **129**, 124105 (2008). We use the "pymbar-2.0beta" implementation of the MBAR method available from https://simtk.org/home/pymbar.

[40] H. J. C. Berendsen, D. van der Spoel, and R. van Druren,

GROMACS: A message-passing parallel molecular dyanmics implemmentation. Comput. Phys. Commun. **91**, 43 (1995); E. Lindahl, B. Hess, and D. van der Spoel, *GROMACS 3.0: A package for molecular simulation and trajectory analysis.* J. Mol. Model. **7**, 306 (2001); van der Spoel, E. Lindahl, B. Hess, G. Groenhof, A. E. Mark, and H. J. C. Berendsen. *GROMACS: Fast, Flexible and Free.* J. Comput. Chem. **26**, 1701 (2005); Hess, C. Kutzner, D. van der Spoel, and E. Lindahl, *GROMACS 4: Algorithms for highly efficient, load balanced, and scalable molecular simulation.* J. Chem. Theory Comput. **4**, 435 (2008).

[41] S. Lundrigan and I. Saika-Voivod, *Test of the classical nucleation theory and mean first-passage time formalism on crystallization in the Lennard-Jones liquid.* J. Chem. Phys. **131**, 104503 (2009).

[42] C. Valeriani, E. Sanz, and D. Frenkel, *Rate of homogeneous crystal nucleation in molten NaCl.* J. Chem. Phys. **122**, 194501 (2005).

[43] P. J. Steinhardt, D. R. Nelson, and M. Ronchetti, *Bond-orientational order in liquids and glasses.* Phys. Rev. B **28**, 784 (2001).

[44] P. R. ten Wolde, M. J. Ruiz-Montero, and D. Frenkel, *Numerical calculation of the rate of crystal nucleation in a Lennard-Jones system at moderate undercooling.* J. Chem. Phys. **104**, 9932 (1996).

[45] E. A. Mastny and J. J. de Pablo, *Melting line of the Lennard-Jones system, infinite size, and full potential.* J. Chem. Phys. **127**, 104504 (2007).

[46] V. G. Baidakov and A. O. Tipeev *Crystal nucleation and the solid liquid interfacial free energy.* J. Chem. Phys. **136**, 074510 (2012).

[47] I. Saika-Voivod, P. H. Poole, and R. K. Bowles *Test of classical nucleation theory on deeply supercooled high-pressure simulated silica.* J. Chem. Phys. **124**, 224709 (2006).

[48] V. G. Baidakov, A. O. Tipeev, K. S. Bobrov, and G. V. Ionov, *Crystal nucleation rate isotherms in Lennard-Jones liquids.* J. Chem. Phys. **132**, 234505 (2010).

[49] B. Scheifele, I. Saika-Voivod, R.K. Bowles, and P.H. Poole, *Heterogeneous Nucleation in the Low Barrier Regime.* Phys. Rev. E, **87**, 042407 (2013).

[50] I. Saika-Voivod, F. Romano, and F. Sciortino, *Nucleation barriers in tetrahedral liquids spanning glassy and crystallizing regimes.* J. Chem. Phys. **135**, 124506 (2011).

[51] L. Filion, M. Hermes, R. Ni, and M. Dijkstra, *Crystal nucleation of hard spheres using molecular dynamics, umbrella sampling, and forward flux sampling: A comparison of simulation techniques.* J. Chem. Phys. **133**, 244115 (2010).

[52] A.S. Clarke and H. Jonsson *Structural changes accompanying densification of random hard-sphere packings.* Phys. Rev. E **47**, 3975 (1993).

[53] S. C. Hendy and B. D. Hall *Molecular-dynamics simulations of lead clusters.* Phys. Rev. B **64**, 085425 (2001).

[54] P. Bhimalapuram, S. Chakrabarty, and B. Bagchi, *Elucidating the mechanism of nucleation near the gas-liquid spinodal.* Phys. Rev. Lett. **98**, 206104 (2007); L. Maibaum, *Comment*, *ibid* **101**, 019601 (2008); P. Bhimalapuram, S. Chakrabarty, and B. Bagchi, *Reply*, *ibid* **101**, 019601 (2008).

[55] I. Saika-Voivod, R.K. Bowles, and P.H. Poole, *Crystal Nucleation in a Supercooled Liquid with Glassy Dynamics.* Phys. Rev. Lett. **103**, 225701 (2009).

[56] S.W. Horacio. *An introduction to stochatic process and nonequilibrium statistical physics* (World Scientific Publishing, Singapore 1994).

[57] A. Einstein, *On the Motion of Small Particles Suspended in Liquids at Rest, Required by the Molecular-Kinetic Theory of Heat.* Ann. d. Phys. **17**, 132 (1905).

[58] M. V. Smoluchowski, Ann. d. Phys. **21**, 756 (1906).

[59] D. S. Lemons, A. Gythiel, *Paul Langevin's 1908 paper "On the Theory of Brownian Motion" ["Sur la théorie du mouvement brownien," C. R. Acad. Sci. (Paris) 146, 530–533 (1908)].* Am. J. Phys. **65**, 11 (1997).

[60] D. Reguera, J. M. Rubi, and J. M. G. Vilar *The mesoscopic dynamics of thermodynamics systems.* J. Chem. Phys. B **109**, 21502 (2005).

[61] A. Kolpas, J. Moehlis, and I. G. Kevrekidis, *Coarse-grained analysis of stochasticity-induced switching between collective motion states.* P. NATL. A. SCI. **104**, 5931 (2007).

Appendix A

The Fokker-Planck Equation

The Fokker-Planck equation is a partial differential equation that describes the time evolution of the probability density of the Lengevin equation, which defines the probability to find the particle at specific time at a specific place. We show in this chapter the derivation for the Fokker-Planck equation from both a physics prospective and a more mathematical approach.

A.1 Stochastic process

Stochastic process is used to describe the evolution of some random variable over time. The methods used to solve the stochastic differential equations (SDE) are important to interpret different fields in economy, population statistics, technology, physics, chemistry, biology, and other fileds [56]. An example of the stochastic process is the Brownian motion. Brownian motion had been addresed by Einstein [57], Smoluchowski [58], and Langevin [59]. They ended with the formula

$$\overline{\Delta_r^2} = \frac{RT}{N}\frac{1}{3\pi\mu a}\tau, \tag{A.1}$$

where τ is the time to predict the mean-squared displacement $\overline{\Delta_r^2}$, μ is the viscosity of the liquid, a is the radius of the particle, T is the temperature, and R is the gas constant. Langevini derived Eq. A.1 from Newton's second law

$$m\frac{\partial^2}{\partial t^2}r = F(r,t), \tag{A.2}$$

where $F(x,t)$ is the net of deterministic and random forces. Thus the position $r(t)$ of the Brownian particle at time t is stochastic process, and can be describe by the evolution of the probability density function over time.

A.2 Derive Fokker-Planck equation from thermodynamics

Fokker-Planck equation can be also derived from the thermodynamics. We follow the strategy in [60] to derive the equation from thermodynamics.

At equilibrium, the change in the entropy S is giving by the Gibbs equation,

$$TdS = dE + pdV - \mu dN, \tag{A.3}$$

where the internal energy E, the volume V, and the number of particles N are the thermodynamic extensive variables of the system, and the temperature T, the pressure p, and the chemical potential μ are the intensive variables. Consider the density function $\rho(x)$ to be spatially dependent in the spatial x-coordinate, then the number of particles on the system is equal to $N = \int v\rho(x)\,dx$, where x is the spatial coordinate and v is the volume per particle. At constant energy, temperature, and volume, and assume a slow change in the quantities in Eq. A.3, we can replace the variations d by

time derivative $\frac{d}{dt}$,

$$T\frac{dS}{dt} = \int v\mu\left(x, \rho(x)\right)\frac{\partial\rho(x)}{\partial t}\,dx, \tag{A.4}$$

where μ depends on the density and hence on x. The conservation law

$$\frac{\partial\rho}{\partial t} = -\frac{\partial J}{\partial x}, \tag{A.5}$$

where J is the flux of particles. Now combine Eq. A.5 with Eq. A.4, and assume the current J vanishes at the boundaries, we get

$$T\frac{dS}{dt} = \int v\mu\frac{\partial J}{\partial x}\,dx. \tag{A.6}$$

Integrate by parts with the assuption that the currents vanishes at the boundaries, we get

$$T\frac{dS}{dt} = -\int J\frac{\partial\mu}{\partial x}\,dx, \tag{A.7}$$

where J has a conjugated force to be the gradiant of the chemical potential. Hence, the flux is proportional to this force

$$J = -L\frac{\partial\mu}{\partial x}, \tag{A.8}$$

where $L = L\left(x, \rho(x)\right)$ is the Onsager coefficient, which depends on x. The diffusion equation can be derived from Eq. A.8 and Eq. A.5

$$\begin{aligned}\frac{\partial\rho}{\partial t} &= \frac{\partial}{\partial x}\left(L\frac{\partial\mu}{\partial x}\right)\\ &= \frac{\partial}{\partial x}\left(L\frac{\partial\mu}{\partial\rho}\frac{\partial\rho}{\partial x}\right)\\ &= \frac{\partial}{\partial x}D\frac{\partial\rho}{\partial x},\end{aligned} \tag{A.9}$$

where D is the diffusion coefficient $D = L\,(\partial\mu/\partial\rho)$.

The entropy of the system in terms of the probability of finding the system in terms of the nonequilibrated degrees of freedom γ at time t, $P(\gamma, t)$ is giving by Gibbs entropy postulate

$$S = S_{eq} - k_B \int P(\gamma, t) \ln \frac{P(\gamma, t)}{P_{eq}(\gamma)}\, d\gamma, \tag{A.10}$$

where S_{eq} is the entropy of the system when the γ are at equilibrium. At any γ that it is not at equilibrium, a contribution to the entropy arises from the deviation of the probability $P(\gamma, t)$ from it equilibrium value $P_{eq}(\gamma)$, which is giving by

$$P_{eq} \cong \exp\left(\frac{-\Delta G(\gamma)}{k_B T}\right), \tag{A.11}$$

where $\Delta G(\gamma)$ is the minimum reversible work required to drive the sytem to the state γ. This work is expressed as

$$\Delta G = \Delta E + p\Delta V - T\Delta S - \mu\Delta N + y\Delta Y + ..., \tag{A.12}$$

where $y\Delta Y$ to be any generic work performed on the system, y is the intensive variable, and Y is the conjugated extensive variable of y. By taking the time evolution of the Gibbs energy postulate, Eq. A.10

$$\frac{dS}{dt} = -k_B \int \frac{\partial P(\gamma, t)}{\partial t} \ln \frac{P(\gamma, t)}{P_{eq}(\gamma)}\, d\gamma, \tag{A.13}$$

and the evolution of the probability density in the γ-space, which governed by the continuity equation

$$\frac{\partial P}{\partial t} = -\frac{\partial J}{\partial \gamma}, \tag{A.14}$$

combine Eq. A.14 with Eq. A.13, we get

$$\frac{dS}{dt} = k_B \int \frac{\partial J(\gamma,t)}{\partial t} \ln \frac{P(\gamma,t)}{P_{eq}(\gamma)}\, d\gamma. \tag{A.15}$$

Integrate Eq. A.15 py parts

$$\frac{dS}{dt} = k_B J \ln \frac{P}{P_{eq}} - k_B \int J(\gamma,t) \frac{\partial}{\partial \gamma} \left(\ln \frac{P(\gamma,t)}{P_{eq}(\gamma)} \right) d\gamma, \tag{A.16}$$

the second part of the RHS is called the entropy production, and we denoted it by σ

$$\sigma = -k_B \int J(\gamma,t) \frac{\partial}{\partial \gamma} \left(\ln \frac{P(\gamma,t)}{P_{eq}(\gamma)} \right) d\gamma. \tag{A.17}$$

Again, the conjugated force of the flux J is the gradient of the logarithm of the ratio of the probability density to its equilibrium value. And the flux is proportional to its conjugated force

$$J(\gamma,t) = -k_B L \frac{\partial}{\partial \gamma} \left(\ln \frac{P(\gamma,t)}{P_{eq}(\gamma)} \right). \tag{A.18}$$

Substitute Eq. A.18 back in the continuity equation, Eq. A.14, and carry on the derivative on the RHS, we get the kinetic equation

$$\frac{\partial P}{\partial t} = \frac{\partial}{\partial \gamma} \left(D P_{eq} \frac{\partial}{\partial \gamma} \frac{p}{p_{eq}} \right). \tag{A.19}$$

Here, the diffusion coefficient D is defined as

$$D(\gamma) = \frac{k_B L(\gamma, P)}{P}, \tag{A.20}$$

and Eq. A.20 can be written in terms of Eq. A.11 as

$$\frac{\partial P}{\partial t} = \frac{\partial}{\partial \gamma}\left(D\frac{\partial P}{\partial \gamma} + \frac{D}{k_B T}\frac{\partial \Delta G}{\partial \gamma}P\right). \tag{A.21}$$

which is Fokker-Planck equation for the evolution of the probability density in γ-space.

A.3 Derive Fokker-Planck equation from Mathmatics

We follow the strategy in the appendix in [61] to derive Fokker-Planck equation. Markov process implies that the observation in the future depends on the most recent observations and do not depend on the previous ones. For a conditinal probability $p\left(r(t_3) = r_3 | r(t_1) = r_1, r(t_2) = r_2\right)$, we implement Markovian process definition to get

$$p\left(r(t_3) = r_3 | r(t_1) = r_1, r(t_2) = r_2\right) = p\left(r(t_3) = r_3 | r(t_2) = r_2\right), \tag{A.22}$$

with $t_1 < t_2 < t_3$.

The Chapman-Kolmogorov equation for Markovian process states

$$p\left(r(t_3) = r_3 | r(t_1) = r_1\right) = \int p\left(r(t_3) = r_3 | r(t_2) = r_2\right) p\left(r(t_2) = r_2 | r(t_1) = r_1\right)\, dx_2. \tag{A.23}$$

Now using the inegral

$$I = \int_{-\infty}^{\infty} h(Y)\frac{\partial p\left(Y, t | X\right)}{\partial t}\, dY, \tag{A.24}$$

and using the forward scheme

$$\int_{-\infty}^{\infty} h(Y)\frac{\partial p\left(Y,t|X\right)}{\partial t}\,dY = \int_{-\infty}^{\infty} h(Y)\lim_{\Delta t\to 0}\left(\frac{p\left(Y,t+\Delta t|X\right)-p\left(Y,t|X\right)}{\Delta t}\right)\,dY. \tag{A.25}$$

- Using Chapman-Kolmogorov equation, and assume Z is the observation between X and Z, we get

$$\lim_{\Delta t\to 0}\frac{1}{\Delta t}\left(\int_{-\infty}^{\infty} h(Y)\int_{-\infty}^{\infty} p\left(Y,\Delta t|Z\right)p\left(Z,t|X\right)\,dZ\,dY - \int_{-\infty}^{\infty} p\left(Y,t|X\right)\,dY\right). \tag{A.26}$$

- The integral over real time is 1, hence, using the identity in the second term $\infty\int_{-\infty}^{\infty} p\left(Y,t|X\right)\,dY = 1$

- Change the order of intergration in the first term from $dZ\,dY$ to $dY\,dZ$

- Use Chapman-Kolmogorov equation again in the second term and let $Y \to Z$ in $h(Y)$

$$\lim_{\Delta t\to 0}\frac{1}{\Delta t}\left(\int_{-\infty}^{\infty} p\left(Z,t|X\right)\int_{-\infty}^{\infty} p\left(Y,\Delta t|Z\right)\left(h(Y)-h(Z)\right)\,dZ\,dY\right). \tag{A.27}$$

- Expand $h(Y)$ about Z using Taylor series $h(Y) = \left(h(Z) + \sum_{n=1}^{\infty} h^{(n)}(Z)\frac{(Y-Z)^n}{n!}\right)$

$$\lim_{\Delta t\to 0}\frac{1}{\Delta t}\left(\int_{-\infty}^{\infty} p\left(Z,t|X\right)\int_{-\infty}^{\infty} p\left(Y,\Delta t|Z\right)\sum_{n=1}^{\infty} h^{(n)}(Z)\frac{(Y-Z)^n}{n!}\,dZ\,dY\right). \tag{A.28}$$

- Define $D^{(n)}(Z)$

$$D^{(n)}(Z) = \frac{1}{n!\,\Delta t}\int_{-\infty}^{\infty}(Y-Z)^n p(Y,\Delta t|Z)\,dY. \tag{A.29}$$

So the integral I becomes

$$\int_{-\infty}^{\infty} h(Y) \left(\frac{\partial p\left(Y,t|X\right)}{\partial t} dY - \sum_{n=1}^{\infty} D^{(n)}(Z) h^{(n)}(Z) \right) dZ = 0. \tag{A.30}$$

Since h is an arbitrary function, it follows

$$\frac{\partial p(X,t)}{\partial t} = \sum_{n=1}^{\infty} \left(-\frac{\partial}{\partial Z} \right)^{n} \left[D^{(n)}(Z) p(X,t) \right]. \tag{A.31}$$

Eq. A.31 is the Fokker-Planck equation in one variable. The general case of Eq. A.31 for $\mathbf{X}$ that defined by the set $\{X_1, X_2, X_3, ..., X_N\}$ for the first two terms $i = \{1, 2\}$ by

$$\frac{\partial p(\mathbf{X},t)}{\partial t} = \sum_{i=1}^{N} -\frac{\partial}{\partial X_i} \left[D^{(1)}(\mathbf{X}) p(\mathbf{X},t) \right] - \sum_{i=1}^{N} \sum_{j=1}^{N} \frac{\partial}{\partial X_i \partial X_j} \left[D^{(2)}(\mathbf{X}) p(\mathbf{X},t) \right]. \tag{A.32}$$

Appendix B

The Simulation Results

We list detailed results in Table B.1: Barrier heights, $\beta\Delta G^*_{MC}$ from MC, $\beta\Delta F^*_{MC}$ from MC, $\beta\Delta F^*_{MD}$ from MD, $\beta\Delta F^{*\,MC}_{\min}$ from MC; critical sizes, n^* from MC, n^*_F from MC, $n^*_{F_{MD}}$ from MD; Zeldovich factors, Z from MC, Z^{MD}_F from MD; attachment rates, $f^+_{\rm crit}$ from MC, $f^+(n^*)$ from MD; surface areas, $\mathrm{S}^*_{\mathrm{MC}}$ from MC, $\mathrm{S}^*_{\mathrm{MD}}$ from MD; and nucleation rates $\mathrm{J_b}$ from MD.

T	$\beta\Delta G^*_{MC}$	$\beta\Delta F^*_{MC}$	$\beta\Delta F^*_{MD}$	$\beta\Delta F^{*\,MC}_{\rm min}$	n^*	$n^*_{F_{MC}}$	$n^*_{F_{MD}}$	Z	Z_F^{MD}	$f^+_{\rm crit}$	$f^+(n^*)$	$\rm S^*_{MC}$	$\rm S^*_{MD}$	$\rm J_b \times 10^5$
0.485	18.80	18.80	18.89	11.08	100	100	102	0.0167	0.0491	42.81	38.97	143.08	146.48	0.2
0.480	17.69	17.69	17.98	9.93	89	89	98	0.0172	0.0483	32.45	48.33	134.40	143.21	0.5
0.475	16.69	16.69	17.5	8.89	79	77	102	0.0216	0.0435	22.43	72.81	130.42	149.94	1.7
0.470	15.76	15.76	16.55	7.92	71	73	91	0.0219	0.0464	29.18	69.18	127.70	140.99	3.9
0.465	14.88	14.88	15.87	6.99	62	62	90		0.0428		81.95		136.95	8.0
0.460	14.21	14.22	14.97	6.26	57	57	79	0.0249	0.0454	20.67	77.10	113.82	131.00	17.9
0.455	13.50	13.5	14.39	5.47	51	52	78		0.0392		60.12		130.11	30.8
0.450	12.97	12.89	13.78	4.79	46	48	72	0.0249	0.0373	16.99	61.89	103.53	127.29	52.5
0.445	12.29	12.29	13.09	4.10	41	42	59		0.0488		49.54		118.28	93.9
0.440	11.81	11.73	12.58	3.45	36	35	50	0.0256	0.0429	11.96	45.31	88.61	111.97	137.7
0.435	11.80	11.23	12.21	2.91	30	28	50		0.0548		47.50		108.07	192.4
0.430	10.84	10.73	11.89	2.31	24	25	46	0.0409	0.0567	8.46	43.98	78.84	99.20	298.0
0.425	10.62	10.07	11.49	1.65	22	18	42		0.0707		43.46		101.46	399.7
0.420	9.96	9.55	11.21	1.14	18	14	38	0.0559	0.0562	5.88	41.93	57.42	95.93	5050.1
0.415	9.18	9.09	11.06	0.74	14	11	37		0.0712		39.28		93.61	593.5
0.410	8.90	8.74	10.79	0.46	13	9	31	0.0686	0.0603	3.55	35.86	43.90	81.93	716.2
0.405	8.63	8.61	9.94	0.10	13	6	17		0.0809		14.73		50.97	738.4
0.400	8.68	8.72	9.77	0.18	13	8	10	0.0708	0.0695	3.75	11.19	48.18	31.33	829.3
0.395	8.53	8.42	9.4	0.01	12	3	16		0.1964		8.69		46.76	910.4
0.390	8.49		8.92		12		10		0.0939		4.90		32.43	998.6
0.385	8.42				12									1091.5
0.380	8.42				12							45.02		1095.1
0.375	8.36				12									1242.3
0.370	8.34				12									1257.9
0.350	8.17				12			0.0707		2.71		42.48		1616.6
0.300	8.00				11			0.0708		2.15		34.43		1829.9
0.250	8.00				10			0.0850		1.13		31.28		1528.1
0.200	7.95				13			0.0550		0.91		45.15		783.9
0.150	8.10				13			0.0558		0.77		50.51		540.9

Table B.1: Simulation results data. For $\beta\Delta F^*_{MC}$ and $\beta\Delta F^*_{MD}$, we have added $\ln N_p = \ln 600 = 6.40$ in order to better compare with ΔG^*_{MC}. For example, at $T = 0.485$, the bare value of $\beta\Delta F^*_{MC} = 12.40$ and at $T = 0.395$, the bare value of $\beta\Delta F^*_{MC} = 2.02$.